

**Modeling and Tradespace Exploration of a Space  
Suit Hip Bearing Assembly using  
Multi-Degree-of-Freedom Range of Motion Analysis**

by

Patrick Calvin McKeen

B.S., Harvey Mudd College (2017)

Submitted to the Department of Aeronautics and Astronautics  
in partial fulfillment of the requirements for the degree of

Master of Science in Aeronautics and Astronautics

at the

MASSACHUSETTS INSTITUTE OF TECHNOLOGY

September 2019

© Massachusetts Institute of Technology 2019. All rights reserved.

Author.....

Department of Aeronautics and Astronautics  
August 22, 2019

Certified by .....

Leia Stirling  
Assistant Professor

Charles Stark Draper Professor of Aeronautics and Astronautics  
Associate Faculty, Institute for Medical Engineering and Science  
Thesis Supervisor

Accepted by.....

Sertac Karaman  
Associate Professor of Aeronautics and Astronautics  
Chair, Graduate Program Committee



# Modeling and Tradespace Exploration of a Space Suit Hip Bearing Assembly using Multi-Degree-of-Freedom Range of Motion Analysis

by

Patrick Calvin McKeen

Submitted to the Department of Aeronautics and Astronautics  
on August 22, 2019, in partial fulfillment of the  
requirements for the degree of  
Master of Science in Aeronautics and Astronautics

## Abstract

Space suits are crucial to human spaceflight, but can restrict motion, require additional energy, and increase injury risk. Previous planetary suits were largely based on flexible components, which generate additional forces on the occupant as they resist volumetric changes from flexing components. The NASA Mark III suit addresses this problem using a Hip Brief Assembly (HBA), composed of rigid, constant-volume sections connected by bearings. However, due to the rigid components and fixed degrees of freedom (DoFs), the HBA and other hard-component joint assemblies (HCJAs) have stricter bounds on motion. For example, previous analysis shows that the hip multi-DoF range of motion (ROM) for an HBA occupant is not well-aligned with the nominal hip ROM during gait (gait NHRM).

In this thesis, a set of methods for describing HCJA geometry and the effect on occupant ROM is presented. A generalized model builds on Denavit-Hartenberg parameterization to describe HCJA structure, rotation, and surface shape. Also included is a computational approach, compatible with standard 3D model files, to estimate the multi-DoF ROM for joints of an HCJA occupant, and compare and score the suit-restricted ROMs against nominal, unencumbered ROMs.

These models are utilized to analyze HBA geometry and improve alignment between in-suit occupant ROM and gait NHRM. A set of design constraints based on feasible geometries and parameter bounds were devised and used to limit a tradespace analysis of alternate geometries in the HBA model. The geometries were evaluated

and given an ROM score based on occupant access to gait NHROM. Over 1.3 billion alternate geometries were tested, and 10,912 met or bested the nominal geometry. The top-scoring geometry showed a more than sixfold improvement on access to gait NHROM, as well as a more natural neutral leg position, a significant increase in adduction range, and improved kneeling ability. The tradespace data set is also used to analyze trends in HBA geometry, suggesting two-bearing HBAs would have very poor hip ROM and the most dominant factors behind a high ROM score is the extent of the cant in the HBA Proximal and Distal sections.

Thesis Supervisor: Leia Stirling

Title: Assistant Professor

Charles Stark Draper Professor of Aeronautics and Astronautics

Associate Faculty, Institute for Medical Engineering and Science



## Acknowledgments

I don't know where I would be without my advisor, Prof. Leia Stirling. She made sure that I could work on research topics that matched my interests and abilities and encouraged me every step of the way. She gave me the confidence that MIT (and the strange, foreign world of academia in general) was within my ability. She has given me invaluable advice, academically, professionally, and otherwise. Thank you.

As I have completed my Master's Degree and written this thesis, I have been lucky to get to know many different people. People all around MIT have made me feel welcome. The Human Systems Lab and MakerWorks communities, in particular, are groups I have been fortunate to be a part of. Specific thanks to Alexa, Brad, Cadence, Chris, Colin, Elliott, Hilary, Jess, Liam, and Michael for making MIT feel like home.

Stephen, you have supported me throughout a difficult and stressful process. Thank you for making sure I survived thesis-writing.

To the Mudd trivia-week squad: thank you for trying to make sure I didn't.

There are many more people to thank for helping me get this far. I would not be the person and engineer I am today without my childhood friends, who continue to influence me after all these years: Sam, you've been a great friend all my life, one that I'm lucky to have; Jake, I don't think I'd have gotten here without some of our crazy ideas; Alex, you are missed.

To Evan, Melissa, and Morgan: You three are major influences on me (in very different ways) and I am very fortunate indeed to have friends like you. I wouldn't be who I am without you and I am grateful to have you as my friends.

To Cherry: Everyday, I use lessons you taught me. I would not be able to do all that I do without all the things I learned from you. Thank you.

Finally, thank you to my family, who have always been a source of strength, usually a source of comfort, and sometimes a source of wisdom. Mom and Dad, you have been inspirations throughout my life. Your advice and support have helped me every step of the way. Anna, you continue to amaze me and I am grateful to have you as my sister. My aunts and uncles: Nate, Amy, Scott, and Jane, I am glad how frequently I get to see you all now that I am in New England. You have been supportive and welcoming, even during a somewhat-concerning thesis-writing craze. Aunt Susie, you have been a pillar of support my entire life. And to my grandparents: Grandpas George, Ed, and Woody, you are missed. Grammy, you have always shown me such love and encouragement. Nana, you have always brightened my days, and made sure that I know I am cherished. Poppa, Mom says it's your fault that I am the engineer and person I am. Thank you.

# Contents

<b>1</b>	<b>Introduction</b>	<b>17</b>
1.1	Background . . . . .	18
1.2	Thesis Aims and Outline . . . . .	22
<b>2</b>	<b>Hard-Component Joint Assembly Model</b>	<b>25</b>
2.1	Model Simplifications . . . . .	26
2.2	Parameterization . . . . .	29
2.3	Physical Structure . . . . .	36
2.4	Surface Generation . . . . .	43
2.4.1	Standard Components . . . . .	45
2.4.2	Non-standard Components . . . . .	46
2.5	Bearings . . . . .	58
<b>3</b>	<b>Multi-Degree-of-Freedom Range of Motion Testing</b>	<b>63</b>
3.1	Unsuited Range of Motion . . . . .	64
3.2	Suited Range of Motion . . . . .	67
3.2.1	Simulated Limb . . . . .	69
3.2.2	Suited Range of Motion Estimation . . . . .	76
3.3	Comparison of Unsuited and Suited Ranges of Motion . . . . .	77

<b>4</b>	<b>Hip Bearing Assembly Design Constraints</b>	<b>89</b>
4.1	Geometric Constraints . . . . .	90
4.1.1	Geometric Constraints for Briefs . . . . .	91
4.1.2	Geometric Constraints for Proximal and Distal Sections . . . . .	97
4.2	Parameter Bounds . . . . .	105
<b>5</b>	<b>Hip Bearing Assembly Tradespace Analysis</b>	<b>111</b>
5.1	Tradespace Exploration Method . . . . .	112
5.2	Preliminary Tradespace Exploration . . . . .	115
5.3	Refined Tradespace Exploration . . . . .	118
5.4	Suggested Geometries . . . . .	121
5.5	Discussion . . . . .	125
5.5.1	Number of Joints . . . . .	125
5.5.2	Geometric Trends . . . . .	127
5.5.3	Effect on Kneeling . . . . .	129
<b>6</b>	<b>Conclusion</b>	<b>131</b>
6.1	Thesis Summary . . . . .	131
6.2	Contributions . . . . .	132
6.3	Limitations . . . . .	133
6.4	Future Work . . . . .	136
<b>A</b>	<b>Definition of Anatomical Terms</b>	<b>139</b>
<b>B</b>	<b>Sinusoidal Projection Proof</b>	<b>143</b>
<b>C</b>	<b>Homogeneous Transformations</b>	<b>149</b>

**D Briefs Bottom Edge Orientation Proof** **153**

**E Constraint Simplification** **157**

E.1 Briefs Constraints . . . . . 157

E.2 Proximal and Distal Sections Constraints . . . . . 166



# List of Figures

1-1	Mark III space suit [22]. . . . .	21
1-2	Mark III Hip Bearing Assembly. . . . .	22
2-1	Sample oblique frustum. . . . .	28
2-2	Example of DH parameters describing a robotic arm. . . . .	32
2-3	Illustration of HCJA model parameters using HBA. . . . .	35
2-4	HCJA example with components and edges highlighted. . . . .	41
2-5	HBA Briefs surface regions. . . . .	48
2-6	HBA Briefs edges and reference points used in Briefs surface generation. . . . .	49
2-7	HBA Briefs top edge zones for surface generation. . . . .	52
2-8	Arrangement of points used to form HBA Briefs surface. . . . .	53
2-9	Point groupings by zone HBA Briefs top edge . . . . .	55
3-1	Convention to transform ab/adduction and flexion/extension angles to a vector in $\mathbb{R}^3$ . . . . .	66
3-2	Unsuited gait hip ROM as region on unit sphere surface. . . . .	67
3-3	HCJA simulated limb example: thigh inside HBA model. . . . .	72
3-4	Difficulties with spherical geometry without axis rotation and sinu- soidal projection. . . . .	79

3-5	Rotation range for vectors in ROM comparison. . . . .	83
3-6	Steps to calculate ROM score. . . . .	88
4-1	Leg Direction geometric constraint. . . . .	92
4-2	Briefs Height geometric constraint. . . . .	94
4-3	Leg Gap geometric constraint. . . . .	95
4-4	Leg Holes inside Briefs geometric constraint. . . . .	96
4-5	Examples of Briefs failing geometric constraints. . . . .	98
4-6	Examples of oblique frusta failing geometric constraints. . . . .	103
5-1	Histograms of parameter value usages in preliminary tradespace exploration. . . . .	117
5-2	ROM scores distribution per parameter in preliminary tradespace exploration . . . . .	117
5-3	Histograms of parameter value usages from refined tradespace exploration. . . . .	120
5-4	ROM score distribution per parameter from refined tradespace exploration. . . . .	121
5-5	Top-scoring HBA geometries from tradespace explorations . . . . .	123
5-6	Suited ROM for top-scoring HBA geometries from tradespace exploration. . . . .	124
5-7	HBA geometry featuring adjacent aligned bearings. . . . .	126
5-8	Suited ROM for example HBA with adjacent aligned bearings and nominal HBA. . . . .	128
5-9	Ab/adduction required for kneeling/squatting for various HBA geometries. . . . .	130



A-1	Sagittal plane. . . . .	139
A-2	Flexion and extension of the hip. . . . .	140
A-3	Abduction and adduction of the hip. . . . .	141



# List of Tables

2.1	Conditions defining HBA Briefs top edge zones. . . . .	51
3.1	Angular bounds of hip position in nominal human gait [17]. . . . .	65
3.2	Dimensions of simulated thigh used in HBA ROM analysis. . . . .	75
4.1	Geometric constraints on HBA components, in terms of model parameters. . . . .	104
4.2	HBA parameter bounds. . . . .	110
5.1	Parameter values explored from preliminary tradespace exploration. . .	115
5.2	Parameter values for Mark III HBA and top-scoring HBA geometries from tradespace exploration. . . . .	116
5.3	Parameter values explored in the refined tradespace exploration. . . .	119
5.4	ROM scores for top-performing HBA geometries in tradespace explorations. . . . .	122
5.5	ROM score statistics for HBA geometries featuring adjacent aligned bearings. . . . .	126
5.6	VIP scores from PLS on refined tradespace HBA parameters and ROM scores. . . . .	129



# Chapter 1

## Introduction

Fifty years before I wrote these words, Commander Neil Armstrong became the first person to stand somewhere other than Earth. As he descended the ladder and took his “small step,” the space suit protecting him from the harsh lunar environment was on display on millions of screens around the world. Since the first human spaceflight, space suits have played a critical role protecting astronauts and facilitating further exploration. However, since the end of the Apollo program 47 years ago, no space suit has been used in a planetary environment. NASA hopes to return humans to the Moon (and onwards to Mars) in the coming decade, and a number of private companies and organizations are planning trips of their own. New versions of space suits are being designed for these missions. This thesis introduces techniques to understand the effect of space suits on occupant mobility and provides information to be considered in the design process, with a specific focus on facilitating human gait for planetary missions. These ideas could be used in the development of the next-generation space suits that will make it easier for the next Neil Armstrong to take her “small step.”

## 1.1 Background

First, a note on terminology is required. The term “space suit” can refer to two different types of garments and a distinction is necessary. The first is a “flight suit,” which is worn by astronauts during the ascent and descent of their vehicle. The baggy, bright orange Advanced Crew Escape Suit (ACES) worn by crew members on the space shuttle may be the most recognized example of these suits [2]. Flight suits are pressure suits, designed to keep the astronauts safe in the event of vehicle depressurization during their ascent or landing and are only worn on Earth or inside the main vehicle [37]. An Extravehicular Activity (EVA) suit, on the other hand, is the type of space suit worn by Armstrong on the Moon and can be used in space. EVA suits are effectively miniaturized vehicles, providing life support and protection, but mobile and shaped around the crew member [27]. EVA suits are the type of suit worn on a “spacewalk” and are the focus of this thesis. When not otherwise specified, “space suit,” “suit,” and similar terms all refer to an EVA suit.

EVA suits were first designed in the 1960s for the Gemini and Vokshod missions, and further developed during the Apollo and Soyuz programs. Suits with similar designs are still in use today: the American Extravehicular Mobility Unit (EMU) and Russian Orlan space suits on the International Space Station [13]. These suits are examples of brilliant engineering, but do have weaknesses. Space suits can cause discomfort, increase the difficulty of motor tasks, increase injury risk, and require additional time and energy to complete tasks [3][33]. These issues stem from a variety of causes, such as the added inertia of the suit components, but one problem, that of “springback” forces, has a particular source [7][23][25].

The Apollo, EMU, and Orlan suits share this problem because they all feature limbs made entirely of flexible materials [13]. These flexible limbs allow for many

types of motion, but are susceptible to a specific problem: when the limbs are moved, the suit bends and changes shape, resulting in a change in the suit’s volume. As the suit is sealed, changing the volume will change the pressure, so moving from the suit’s neutral, fully-inflated position produces springback forces that resist any deformation or movement [3][23][29]. These springback forces can cause a variety of issues, including reduced mobility and increased energy usage for the suit occupant [3].

With missions to the Moon and other bodies under consideration for the near future, springback forces are particularly relevant. The upcoming surface missions will require astronauts to do something they have not done in 50 years: walk. The EMU suit, for example, was designed for spacewalks, which do not require the same lower limb involvement as surface EVAs [15]. It severely restricts the occupant’s hip, allowing only 37 degrees of hip flexion,<sup>1</sup> compared to 68 degrees in the Apollo suit and 107 degrees for an unsuited individual [12]. Even without that limitation, lower limb movements can present serious problems stemming from springback forces and the suit’s resistance to motion; Apollo astronauts reported not only great difficulty with locomotion, but exertion in their thighs to the point of fatigue [4][28]. Such extensive use of the thigh was likely connected to motions of the hip used for walking, indicating the suit hip joint and the gait motion may be particularly susceptible to springback forces [12][38].

The problems caused by springback forces, particularly on gait, have been addressed in various ways. One approach is to lower the suit’s operating pressure, but doing so can increase the risk of decompression sickness when transitioning to the primary vehicle and necessitate that astronauts pre-breathe pure oxygen before donning the suit [3][10][28]. An alternative approach uses suits built from bearings and rigid components instead of flexible materials [10][16]. As the suit moves,

---

<sup>1</sup>Flexion is defined, along with other anatomical terms used in this thesis, in Appendix A.

the rigid components pivot on their bearings, but the volume of the suit does not change; springback forces are mitigated or eliminated and a higher operating pressure is possible. This approach has been used to create space suits consisting entirely of hard components, but hybrid suits with a mix of hard and soft parts are more common [10][13]. For example, the EMU and Orlan suits both use rigid components around the upper torso, but soft materials elsewhere [13]. This thesis will focus on suits with at least one “hard-component joint assembly” (HCJA), where the degrees of freedom (DoFs) of the occupant’s corresponding joint are matched entirely through hard components. This includes both suits that are entirely rigid or those which feature a mix of materials. The umbrella term “hard-joint suits” will be used.<sup>2</sup>

One of the most prominent examples of a hard-joint suit is the NASA Mark III demonstrator space suit, shown in Figure 1-1. First designed in the late 1980s to test a higher-pressure suit design, it has since become a test platform for space suit concepts and technologies [16][36]. Due to its higher operating pressure, the Mark III was created with springback forces specifically in mind [16]. To counter springback forces, particularly those that would fatigue the thigh during gait, the suit uses an HCJA at the hips [16]. The assembly for this joint is called the Hip Bearing Assembly (HBA) is composed of several rigid components: the Briefs, a Proximal Section for each leg, and a Distal Section for each leg. The HBA can be seen as part of the Mark III in Figure 1-1 and in isolation, with labeled components and bearings, in Figure 1-2.

HCJAs, like the Mark III HBA, reduce problems associated with springback forces, but do not alleviate all space suit difficulties. In fact, hard-joint suits can exacerbate some of these issues by restricting the occupant’s mobility [7][25]. Soft

---

<sup>2</sup>Though the EMU and Orlan suits are previously mentioned as hybrid suits, they are not hard-joint suits. They have hard components, but the limbs are made entirely of soft goods.





Figure 1-1: Picture of the Mark III suit. Above the waist is the Hard Upper Torso (HUT), below the waist is the Hip Bearing Assembly (HBA). Source: NASA [22].

suits can flex to many positions (though the pressurization and springback forces can make this difficult), but hard-joint suits are bounded by the geometry and placement of their bearings [16]. If these bounds are misaligned with the occupant’s natural motions, they are forced to use “programmed” motions [1][6][31]. Programmed motions, which can be new and unnatural to the occupant, can increase injury risk, discomfort, and energy expenditure [6][31]. While the Mark III has much greater mobility than the EMU or Apollo suit, it still suffers from this problem [15]. In particular, previous research has shown that the motion envelope of the Mark III

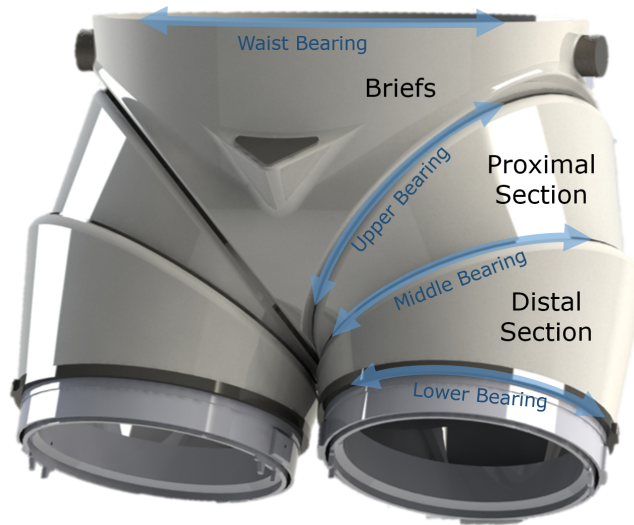


Figure 1-2: Model of the Mark III suit Hip Bearing Assembly (HBA), with the components and bearings labeled. Bearings are highlighted and labeled in blue, while primary components are in black. Image Source: Cullinane [8]. Labels added.

occupant's hips is severely misaligned with the hip positions usually used for gait [5]. As a result, occupants of the Mark III are forced to use programmed motions for ambulation [1][15].

## 1.2 Thesis Aims and Outline

This thesis explores the geometry of hard-joint suits and their impact on occupant mobility. The approaches for these techniques are then applied to the Mark III HBA to understand its design constraints and to explore possible alternate geometries.

Specifically, the aims of this thesis are as follows:

1. Develop a generalized model of HCJA geometry, including kinematic and physical structure, rotation and DoFs, and overall shape. This model is presented

in Chapter 2.

2. Demonstrate a new method of estimating and quantifying the impact of an HCJA on the mobility of the suit's occupant. This method is described in Chapter 3.
3. Explore potential HCJA design constraints, and the connections with the parameters of the geometric model. This is discussed in Chapter 4, with a focus on the HBA.
4. Suggest novel alternate geometries of the HBA that could facilitate a more natural gait. The tradespace of the HBA was analyzed for impact on gait-related mobility and a new alternate geometry is proposed in Chapter 5.



# Chapter 2

## Hard-Component Joint Assembly

### Model

A general model of the geometry of hard-component joint assemblies (HCJAs) was created to define and describe design possibilities. An HCJA is a portion of a hard-joint space suit consisting of a number of independently-mobile rigid components connected by bearings. Other assumptions and definitions used in this model are listed in Section 2.1.

The kinematic structure such as reference frames and degrees of freedom (DoFs) of the components and bearings are defined with an extension of Denavit-Hartenberg parameters (described in Section 2.2). The Mark III Hip Bearing Assembly (HBA), for example, was described with twenty-two parameters. To define the physical structure of HCJAs, the edges of each component is defined from the parameters. These edges describe the locations of the bearings and physical joints as well as the interfaces between components. The derivation of the geometry of these edges (and thus the overall physical structure of the HCJA) from the parameter set is presented

in Section 2.3. Finally, to describe the overall shape of the components, surfaces are generated for each (Section 2.4).

## 2.1 Model Simplifications

To model HCJA geometry, some simplifications were made:

1. The HCJA is treated as a simple rigid body tree (RBT). Each component has exactly one component immediately proximal to it, and there is only one kinematic path from every component to the base.
2. The HCJA is assumed to exclude the final segment of a space suit on every limb, such that there is one or more suit segment between all HCJA components and the end of a suit limb. This segment could be soft goods covering the remainder of the occupant's limb, a boot, a glove, or some combination. As they do not include the ends of suit limbs, all components of the HCJA have at least two edges.
3. The HCJA being modeled is reduced to a minimal number of relevant components responsible for structure and shape, along with the bearings. Adjacent soft-good components, in particular, are excluded. For example, the Mark III HBA was reduced to the bearings and the following components: the Briefs, a Proximal Section for each leg, and one Distal Section per leg, labeled in Figure 1-2. The soft goods and their bracket were not included in the parameterization.
4. Motion between HCJA components is assumed to be ideal. The components do not flex or bend, and the rotation at HCJA joints is entirely around the

defined axes, with no translation or rattling.

5. The geometries of HCJA components are simplified. Every edge of a component was treated as a single circle in  $\mathbb{R}^3$ .
6. Overlap between HCJA components is assumed to be zero. In physical suits, the components extend past one another, overlapping with the bearing between them. While the bearings are included in this model, the overlap is not parameterized separately and represented.
7. The shapes of HCJA components (but not the bearings) are modeled as two-dimensional infinitely thin surfaces in  $\mathbb{R}^3$ .
8. All HCJA components are designated as either standard or non-standard components. Standard components have only one component connected to them distally. Non-standard components have more than one component directly distal to them. In other words, standard components have exactly one bearing at either end, while non-standard components have more than one at their distal end. Non-standard components correspond to points in the RBT where it branches, as they have more than one distal neighbor. These components are treated identically,<sup>1</sup> except for describing the overall shape of the component: standard components use a standard method to define surfaces, while non-standard components do not (see Section 2.4.)
9. The shape of a standard HCJA component is defined by a surface between the circles that make up the edges of the component. The shape formed is similar to

---

<sup>1</sup>While the mathematics is identical, the implementation of HCJAs with non-standard components may be somewhat more complex, as indexing is less intuitive and the non-standard components have more than one distal neighbor, and those transformations and their associated parameters must be distinguished from one another.

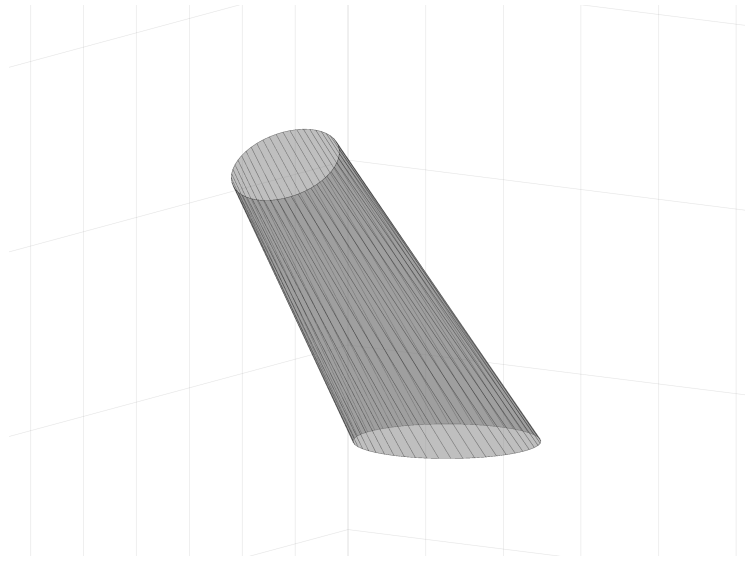


Figure 2-1: Example of an oblique frustum, used to model the shapes of standard HCJA components.

a truncated oblique cone, where the cone's axis is not necessarily perpendicular to the base and the truncation plane is not required to be perpendicular to the axis or parallel to the base. We call this shape, an example of which is shown in Figure 2-1, an oblique frustum.

10. Non-standard HCJA components do not have a standard method to generate the surfaces representing their shape. The surface generation method required may vary heavily based on the application of the model. Due to this variability, no general method to describe the surfaces of non-standard components is presented here, though an example is provided.
11. Bearings are treated as three-dimensional flat rings, with a constant height. They were not parameterized separately. Instead, the internal and external radii were treated as equal to the radii of the edges of the two components the bearing is between (see Section 2.5).



## 2.2 Parameterization

With the simplifications in Section 2.1 applied, the HCJA can be treated like any rigid body system of motion, and its kinematic structure can be described using Denavit-Hartenberg (DH) parameterization [24]. DH parameterization is a standard way of describing coordinate transformations in an RBT, using four parameters for each transformation. A brief introduction is given here. For more information, see *Introduction to Robotics: Analysis, Control, Applications* [24].

The HCJA is divided by degrees-of-freedom (DoFs). The one or more DoFs of every joint in the HCJA is assigned a coordinate frame, which moves with the DoF.<sup>2</sup> These frames are indexed from 1 to  $N_{DoF}$ , where  $N_{DoF}$  is the number of DoFs in the system. The indices are arranged such that every frame has a unique index and the kinematic chain from any frame  $n$  to the base contains no frames with a lower index than  $n$ . The origin and axes of each frame is based on the geometry of the associated DoF and joint in some neutral position defined for the system. For every frame  $n$ , its  $z$ -axis,  $z_n$ , is collinear with the axis of the affiliated DoF and passes through the center of the corresponding joint.<sup>3</sup> The  $x$ -axis for frame  $n$ ,  $x_n$ , is the common normal of  $z_n$  and  $z_{n-1}$ , the  $z$ -axis of the preceding joint.<sup>4</sup> The origin of frame  $n$  is the intersection of  $z_n$  and  $x_n$ , and the  $y$ -axis,  $y_n$ , is defined to create a

---

<sup>2</sup>If a physical joint has more than one DoF, it will have more than one frame to capture its motion.

<sup>3</sup>For the purposes of this work, only rotational joints are considered. DH parameters also work with translational joints, but that is unnecessary for this research.

<sup>4</sup>If the  $z$ -axes are parallel or intersect, there are infinite or zero common normals. In all other cases, where the  $z$ -axes are skew, there is only one. If the  $z$ -axes are parallel (with an infinite number of common normals), the  $x$ -axis of the previous joint is used, for simplicity. When the  $z$ -axes intersect (with zero common normals or a common normal of length zero), then the cross product (in either direction) of the two  $z$ -axes is used as the  $x$ -axis.

right-hand reference frame.<sup>5</sup>

As all DoFs and joints are paired with exactly one frame, there can be no movement within a frame or at locations other than the defined joints. Therefore, the components of the system between joints<sup>6</sup>  $n$  and  $n + 1$  are fixed in the frame  $n$ . The component (one or more rigidly-connected parts of the HCJA) between joints  $n$  and  $n + 1$ , fixed in frame  $n$ , will be called component  $n$ .<sup>7</sup>

With this procedure, the origin and coordinate frame for every joint are defined, and the position and orientation of every component in the HCJA can be described using the frames. An example of a robotic arm with origins and coordinate axes (as well as the DH parameters) labeled can be seen in Figure 2-2. With the “nodes” of the kinematic structure of the system defined, the transformations between each pair of adjacent frames are described by four parameters (each corresponding to a portion of the transformation) in the following order:

1.  $\theta$ : The most proximal coordinate frame of the pair, denoted by frame index  $n$ , has  $x$ -axis  $x_n$ ,  $y$ -axis  $y_n$ , and  $z$ -axis  $z_n$ . This frame is rotated by  $\theta_n$  around  $z_n$  until  $x_n$  is parallel to  $x_{n+1}$ , the  $x$ -axis of the second, more distal coordinate frame of the pair (frame  $n + 1$ ). (Given the rules defining the axes, there will always exist some rotation  $\theta_n$  which will make  $x_n$  and  $x_{n+1}$  parallel.)

---

<sup>5</sup>Note that  $x_n$ ,  $y_n$ , and  $z_n$  do not have a vector hat or arrow above them. This notation means that the axes are not simply directions, but represent the actual axes of the frame, which intersect at the frame origin.

<sup>6</sup>The notation here, and throughout this section, of  $n$  and  $n + 1$  generally assumes that adjacent frames have adjacent indices. This is not the case when the RBT has branches. This notation is used, however, because the convenient similarities between the indices of the frames, parameters, origins, and components can be very helpful for those new to the topic and the  $n \rightarrow n + 1$  relationship can help intuitively. The only difference in the expressions in this section for the case where the RBT has branches are the indices. All equations and definitions are equivalent. In cases where a frame has more than one distal neighbor, the parameters affiliated with the various neighbors have no influence or impact on one another, and are all treated as if they were the only distal neighbor.

<sup>7</sup>By extension, in our assigned rigid body chain, the base of the system is component 0, associated with frame 0, which is the global frame. This is a useful and logical connection.

2.  $d$ : The rotated coordinate frame is shifted by distance  $d_n$  along  $z_n$ ,<sup>8</sup> until the now-shifted  $x_n$  is collinear with  $x_{n+1}$ .
3.  $a$ : The already-shifted coordinate frame  $n$  is shifted again, along its current  $x$ -axis (which is collinear with  $x_{n+1}$ ) by distance  $a_n$ , until the origins of coordinate frames  $n$  and  $n + 1$  overlap.
4.  $\alpha$ : With the origins of coordinate frames  $n$  and  $n + 1$  overlapping, the frames differ only by a rotation. The parameter  $\alpha_n$  provides this rotation, and coordinate frame  $n$  is rotated about its shifted  $x$ -axis (identical to  $x_{n+1}$ ) until the frames are identical.

The subscripts of each parameter  $\theta$ ,  $d$ ,  $a$  and  $\alpha$  identify the transformation to which it belongs: parameters with subscript  $n$  are used to transform between frames  $n$  and  $n + 1$ . The transformations are simple to adjust when the system has moved from its neutral position, into a new “pose.” If joint  $n$  rotates by angle  $\phi_n$ ,  $\theta_n$  is replaced in the transformation by  $\theta_n + \phi_n$ .<sup>9</sup>

These DH parameters encode the location of frame origins and the HCJA’s axes of motion, but, as can be seen in Figure 2-2, they do not specify the actual location of each physical joint or the physical structure of each component at those joints. To fully describe the HCJA, these must be modeled. Thus, a parameter  $h$  is added for

---

<sup>8</sup>The rotation in step 1 was about  $z_n$ , and thus  $z_n$  did not change. The axis along which the frame is now translated can be considered either the original  $z$ -axis or the  $z$ -axis after the  $\theta$  rotation, as these axes are identical.

<sup>9</sup>It is possible to treat this rotation by  $\phi_n$  as a change in the value of  $\theta_n$ , so that  $\theta_n$  simply changes as the system moves. For this research, however, we are explicitly concerned with the geometry of the HCJA, which is described with  $\theta$ . Thus, we treat  $\theta$  as constant, so the geometry is constant, and use the  $\phi$  variables to represent changes in kinematics or poses of the HCJA.

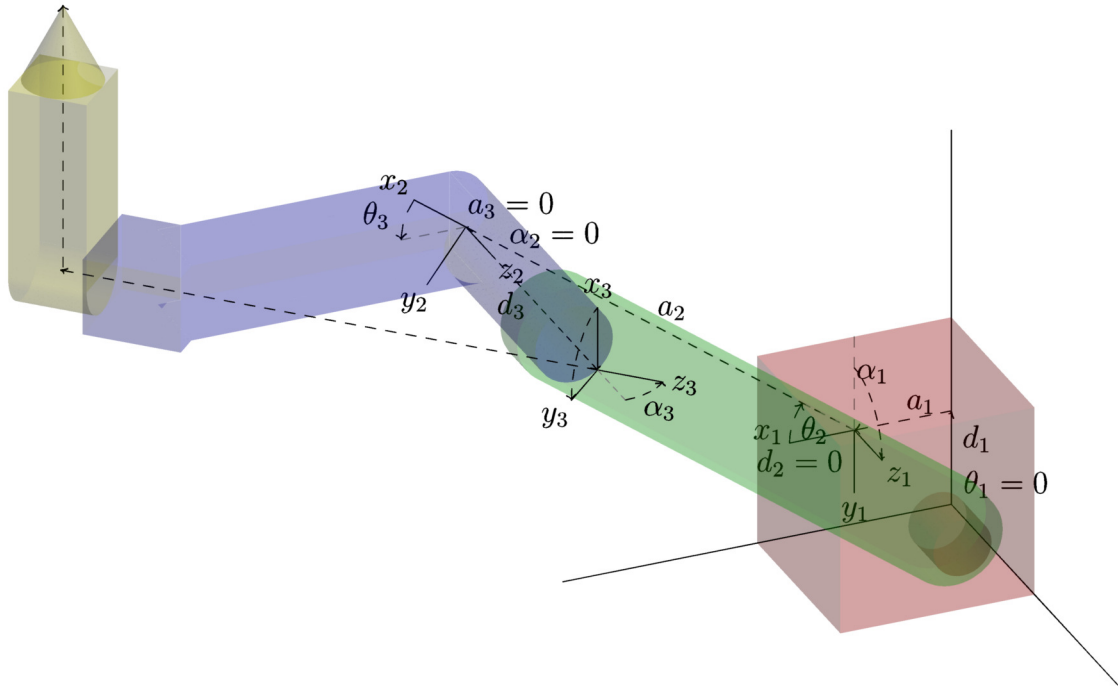


Figure 2-2: Example of DH parameters describing a robotic arm, as well as the origins and axes of each coordinate frame. The red box is the the robot base, the green bar is component 1, the blue bar component 2, and the yellow structure component 3. Dotted lines indicate transformations associated with one of the DH parameters, while solid lines are the axes of each coordinate frames. The origin of each frame lies at the junction of the three frame axes. Note that the reference frames are aligned with the joints, but do not always sit on them. Several additional details to note: (1) the first coordinate frame (frame 0) is not defined by a joint, but by the robot base, affiliated with the global frame; (2) To better demonstrate DH parameterization and how it applies, this robot has been moved from its neutral position (The DH parameters were defined with the green bar entirely horizontal, and then moved with the robot. In the neutral position,  $x_1$  and  $x_2$  would be parallel, as  $z_1$  and  $z_2$  are parallel.); and (3) there is an additional pair of dotted lines that do not correspond to DH parameters, showing the path from the origin of frame 3 to the tip of component.

each joint, and a pair of parameters  $r_t$  and  $r_b$  are added for each component.<sup>10</sup> An example of these parameters in the Mark III HBA is shown in Figure 2-3.

The definition of the  $h$  parameter for joint  $n$  (between frames  $n$  and  $n + 1$ ) takes advantage of the fact that the physical actualization of the joint corresponding to the DoF represented by joint  $n$  lies along  $z_n$ . This means the location of the physical joint can be identified by a displacement along  $z_n$ . For each joint in the HCJA, we add an  $h$  parameter to indicate the distance between the frame's origin and the location of the physical joint, measured along  $z_n$ . The DH parameters apply to transitions between joints, and govern the geometry of the single component between those joints. The  $h$  parameters, in contrast, affect the geometry of the components on both sides of the joint. Due to this shared significance, a different index style is used. The distance from the origin of frame  $n$  to the center of the physical joint associated with joint  $n + 1$ , measured along  $z_n$ , is defined as  $h_{n/n+1}$ .

We must describe not just the locations of the physical joints, but the physical structure of the components. As mentioned in the simplifications list earlier in Section 2.1, this model assumes HCJA components are infinitely thin surfaces, beginning and ending in circles in  $\mathbb{R}^3$ . Thus, we can describe the physical structure of each HCJA component, and its interactions with the joints on either side, with a pair of circles. With surfaces generated (see Section 2.4), the component's shape will be an oblique frustum, like the one seen in Figure 2-1. We know the location of the circle

---

<sup>10</sup>As previously mentioned, the notation assumes all components are standard such that adjacent frames and components have adjacent indices. Non-standard components have more than one distal neighbor. If a non-standard component has  $N$  distal neighbors, there will be  $N$  values for  $r_b$  ( $r_{bI}, r_{bII}, \dots$ ), not just one, corresponding to  $N + 1$  circles (not just 2) used to define their edges. Similarly, there will be  $N$  different  $h$  parameters to indicate the offset to the physical locations of those distally-located joints. All formulae are the same, except for indexing like this. Each of these values is applied and defined as if it were the only distal edge. The only difference in the math occurs for surface generation, where non-standard components do not have a standard approach to generate their surface and may not be oblique frusta.

centers and the planes in which they lie (they must be normal to and centered on the  $z$ -axis of the joints at each end of the component, as the bearings rotate around those axes), so all that is necessary to describe the edges of a component is the radii of the two circles.

The radii can be thought of in pairs, corresponding to the “top” (proximal) and “bottom” (distal) ends of a component. The top radii for a component is indicated by  $r_{nt}$  and the bottom radii by  $r_{nb}$ , where  $n$  is the index of the component or frame. These radii are used to create the top and bottom edges of each component, a process which is discussed further in Section 2.3.

A visual example of this parameterization applied to the Mark III HBA (all parameters labeled) can be see in in Figure 2-3. The specific values of these parameters for the HBA can be found in Table 4.2.

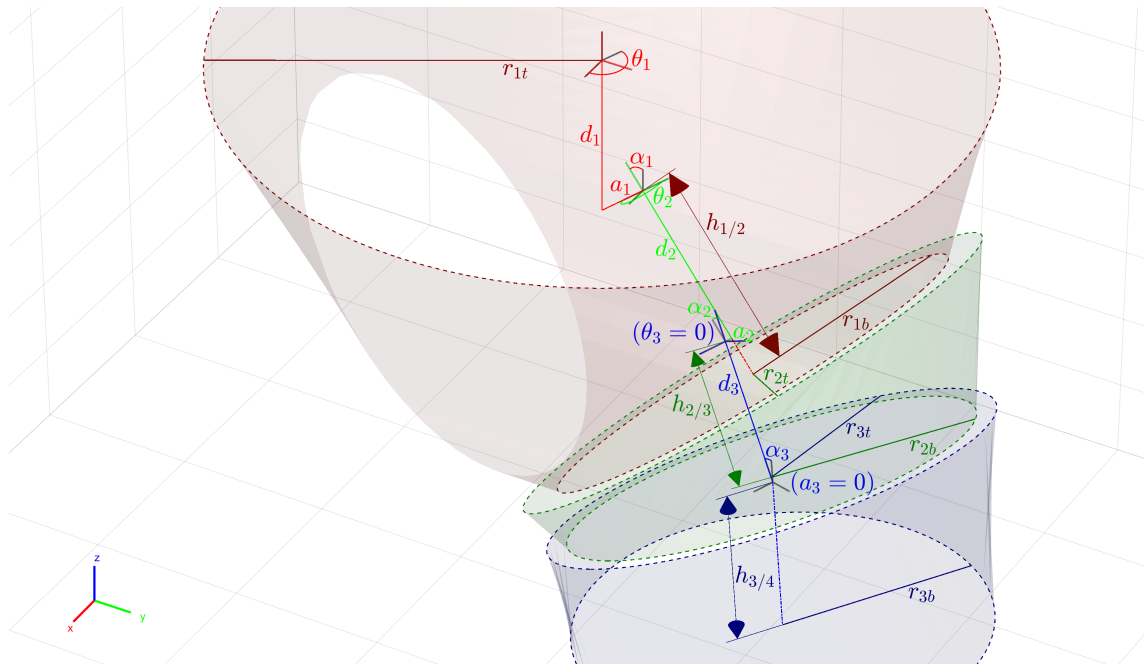


Figure 2-3: An overview of the parameters used to describe the geometry of a HCJA, applied to the Mark III HBA. The parameters are color-coded by component. Red values/lines correspond to the Briefs (frame 1), green corresponds to the Proximal Section (frame 2), and blue corresponds to the Distal Section (frame 3). The origin of each component reference frame is indicated by a 3-axis coordinate marker, in its own color. The Denavit-Hartenberg parameters used to describe each component are included in the same color, as well as the additional parameters (top and bottom radii  $r_t$  and  $r_b$ , and physical joint offset  $h$ ) in a darkened hue of the same color. The dotted lines are the component edges and the dotted-dashed lines are lines along the axes used by the offset parameters. The global frame (frame 0) axes are also included in the bottom left corner.

## 2.3 Physical Structure

To fully describe HCJA geometries using the parameterization described in Section 2.2, there must be a clear method to derive the HCJA's physical structure from the parameter set. After the physical structure of the HCJA is defined, the location and orientation of each component in the global frame can be found.

The approach to defining the suit structure described in this section relies heavily on homogeneous transformations. The notation of, and a simple primer in, these transformations can be found in Appendix C. The homogeneous transformation to frame  $n$  from its distally adjacent neighbor  $n + 1$  (without joint rotation, so  $\phi_n = 0$ ), is represented by  ${}^nT_{n+1}$  and can be defined using the DH parameters of the frame.<sup>11</sup> The formula is

$${}^nT_{n+1} = \begin{bmatrix} \cos \theta_n & -\sin \theta_n \cos \alpha_n & \sin \theta_n \sin \alpha_n & a_n \cos \theta_n \\ \sin \theta_n & \cos \theta_n \cos \alpha_n & -\cos \theta_n \sin \alpha_n & a_n \sin \theta_n \\ 0 & \sin \alpha_n & \cos \alpha_n & d_n \\ 0 & 0 & 0 & 1 \end{bmatrix}. \quad (2.1)$$

---

<sup>11</sup>The notation here, and throughout this section, assumes adjacent frames have adjacent indices. This is not the case when the RBT has branches. This notation is used, however, for clarity and simplicity. The only difference in the expressions for an RBT with branches is the indices. All equations and definitions are equivalent. In cases where a frame has more than one distal neighbor, the parameters affiliated with the various neighbors have no influence or impact on one another, and are all treated as if they were the only distal neighbor. All of the distal or bottom edges for the different frames are created as if they were the only distal neighbor.



The transformation for the rotation  $\phi_n$  about joint  $n$  is

$$J(\phi_n) = T(\phi_n, 0, 0, 0) = \begin{bmatrix} \cos \phi_n & -\sin \phi_n & 0 & 0 \\ \sin \phi_n & \cos \phi_n & 0 & 0 \\ 0 & 0 & 1 & 0 \\ 0 & 0 & 0 & 1 \end{bmatrix}. \quad (2.2)$$

Transformations between frames are applied by simply pre-multiplying a vector in frame  $n + 1$  by these matrices. For detailed information, see Appendix C.

Locations in each component or its affiliated frame, both indexed from 0 to  $N_{DoF}$ ,<sup>12</sup> can be converted to the global frame (or any other frame in the HCJA) using homogeneous transformations. The transformation matrix from frame 4 to the global frame, for example, would be

$${}^0T_4 = {}^0T_1 J(\phi_1) {}^1T_2 J(\phi_2) {}^2T_3 J(\phi_3) {}^3T_4 J(\phi_4).$$

As described in Section 2.2, every component  $n$  is fixed within corresponding reference frame  $n$  that is described relative to the other frames by the sets of four DH parameters. The position and structure of component  $n$  and its joints are described by the additional  $r$  and  $h$  parameters. It has circular edges of radii  $r_{nt}$  and  $r_{nb}$  at the top and bottom, respectively. The position of this top edge is defined by  $h_{n-1/n}$ , while  $h_{n/n+1}$  governs the bottom edge. We can use these values to describe the positions of the component edges.

Consider the component  $n$ , corresponding to frame  $n$ , with top edge at joint  $n$

---

<sup>12</sup>Due to the methods by which edges are described (detailed in this section), the frame after the final HCJA component may be utilized. As mentioned in Section 2.1, the HCJA does not contain the final portion of the suit for any limb, so there will always be at least one part of the space suit remaining, such as boot or glove. The geometry or details of that part are not used, just the frame.

and bottom edge at joint  $n + 1$ . The top edge circle can be most easily described in frame  $n$ , the component's own frame. The top edge is centered at a point we call  $\vec{c}_{nt}$ , located a distance of  $h_{n-1/n}$  along  $z_n$  from the origin of frame  $n$ . The value of  $\vec{c}_{nt}$  (or any vector  $\vec{v}$ ) in frame  $n$  is indicated by a pre-appended superscript with the frame index. In this case, we have

$${}^n\vec{c}_{nt} = \begin{bmatrix} 0 & 0 & h_{n-1/n} & 1 \end{bmatrix}^T \quad (2.3)$$

in frame  $n$ .<sup>13</sup> The circle that forms this top edge has radius  $r_{nt}$  and is normal to  $n_z$ , so it is located in a plane parallel to the  $xy$ -plane of frame  $n$ . Using this information, we will describe the top edge of component  $n$  as the set of points traced out by the vector parametric equation  $\vec{t}_n(p)$ , where  $p$  is a parametric variable on the interval  $[0, 2\pi)$ . In frame  $n$ , we have

$${}^n\vec{t}_n(p) = \begin{bmatrix} 0 \\ 0 \\ h_{n-1/n} \\ 1 \end{bmatrix} + r_{nt} \begin{bmatrix} 1 & 0 \\ 0 & 1 \\ 0 & 0 \\ 0 & 0 \end{bmatrix} \begin{bmatrix} \cos p \\ \sin p \end{bmatrix} = \begin{bmatrix} r_{nt} \cos p \\ r_{nt} \sin p \\ h_{n-1/n} \\ 1 \end{bmatrix}, \forall p \in [0, 2\pi). \quad (2.4)$$

The bottom edge circle can be most easily described in frame  $n + 1$ ,<sup>14</sup> the frame

---

<sup>13</sup>The pre-affixed subscript indicates the frame in which a vector is expressed when the components of the vector are specified. When working with multiple frames, this is an important distinction. For example,  ${}^n\vec{c}_{1t}$  and  ${}^0\vec{c}_{1t}$  would refer to the same point in space, but they refer to that point from different frames and origins, so the components composing the vector may differ. When a frame transformation like  ${}^nT_{n+1}$  is used, it is not modifying the vector, but modifying the frame in which it is expressed. This notation is used throughout.

<sup>14</sup>This approach is simpler because the bottom edge of component  $n$  is coplanar with the top edge of component  $n + 1$ . The bottom edge is described identically to the top edge, but it is described in the next frame and then undergoes a coordinate transformation. This is the reason behind the previous footnote about in some instances requiring the frame after the end of the HCJA. It is used to define the bottom edge of the most distal component in the HCJA.

of the next component, and then transformed back to frame  $n$ . The bottom edge is centered at  $\vec{c}_{nb} = \vec{c}_{(n+1)t}$ , described in frame  $n + 1$  as  ${}^{n+1}\vec{c}_{nb} = \begin{bmatrix} 0 & 0 & h_{n/n+1} & 1 \end{bmatrix}^T$ . In other words, it is a distance  $h_{n/n+1}$  along  $z_{n+1}$  from the origin of frame  $n + 1$ . The circle that forms this bottom edge is normal to this vector, so it is located in a plane parallel to the  $xy$ -plane of frame  $n + 1$ , and it has radius  $r_{nb}$ . To transform these vectors back into frame  $n$ , we can use the transformation  ${}^nT_{n+1}J(\phi_{n+1})$ . As we are transforming a circle centered on and normal to  $z_{n+1}$  and  $J(\phi_{n+1})$  represents a rotation about  $z_{n+1}$ , we can ignore the  $J$  matrix representing the kinematic rotation, as it just transforms the circle onto itself. This is a circle centered at the point  $\vec{c}_{nb} = \vec{c}_{(n+1)t}$ . Described in the frame  $n + 1$ , it is

$${}^{n+1}\vec{c}_{nb} = {}^{n+1}\vec{c}_{(n+1)t} = \begin{bmatrix} 0 \\ 0 \\ h_{n/n+1} \\ 1 \end{bmatrix}$$

and lies in the plane described by coordinate frame unit vectors<sup>15</sup>

$${}^{n+1}\hat{x}_{n+1} = \begin{bmatrix} 1 \\ 0 \\ 0 \\ 0 \end{bmatrix} \quad \text{and} \quad {}^{n+1}\hat{y}_{n+1} = \begin{bmatrix} 0 \\ 1 \\ 0 \\ 0 \end{bmatrix}.$$

---

<sup>15</sup>Unlike the previously defined axes with no hat, the hat-topped unit vectors  $\hat{x}_n$ ,  $\hat{y}_n$ , and  $\hat{z}_n$  describe directions parallel to the frame axes, not inherently the lines of the axes themselves.

Transformed into the  $n$  frame, we have the center

$${}^n\vec{c}_{nb} = {}^nT_{n+1} {}^{n+1}\vec{c}_{nb} = {}^nT_{n+1} \begin{bmatrix} 0 \\ 0 \\ h_{n/n+1} \\ 1 \end{bmatrix} \quad (2.5)$$

and the vectors for the plane

$${}^n\hat{x}_{n+1} = {}^nT_{n+1} {}^{n+1}\hat{x}_{n+1} = {}^nT_{n+1} \begin{bmatrix} 1 \\ 0 \\ 0 \\ 0 \end{bmatrix} \quad \text{and} \quad {}^n\hat{y}_{n+1} = {}^nT_{n+1} {}^{n+1}\hat{y}_{n+1} = {}^nT_{n+1} \begin{bmatrix} 0 \\ 1 \\ 0 \\ 0 \end{bmatrix} .$$

We describe this bottom edge as the set of points traced out (in frame  $n$ ) by the vector parametric equation  $\vec{b}_n(p)$ , where  $p$  is a parametric variable<sup>16</sup> on the interval  $[0, 2\pi)$ . In frame  $n$ , this is

$${}^n\vec{b}_n(p) = {}^nT_{n+1} \begin{bmatrix} 0 \\ 0 \\ h_{n/n+1} \\ 1 \end{bmatrix} + r_{nb} {}^nT_{n+1} \begin{bmatrix} 1 & 0 \\ 0 & 1 \\ 0 & 0 \\ 0 & 0 \end{bmatrix} \begin{bmatrix} \cos p \\ \sin p \end{bmatrix}, \quad \forall p \in [0, 2\pi),$$

---

<sup>16</sup>Please note that while this is the same  $p$  as used to define  $\vec{t}_n(p)$ ,  $p$  simply denotes the parametric variable in both cases. It describes how the function relates to its arguments, and should only be considered within the function for which it is being used.

which simplifies to

$${}^n\vec{b}_n(p) = {}^nT_{n+1} \begin{bmatrix} r_{nb} \cos p \\ r_{nb} \sin p \\ h_{n/n+1} \\ 1 \end{bmatrix}, \forall p \in [0, 2\pi). \quad (2.6)$$

An example of an HCJA with  $r_{nt}$ 's,  $r_{nb}$ 's, and  $h_{n/n+1}$ 's labeled can be seen in Figure 2-3. The same HCJA with the edges and their associated components highlighted can be found in Figure 2-4.

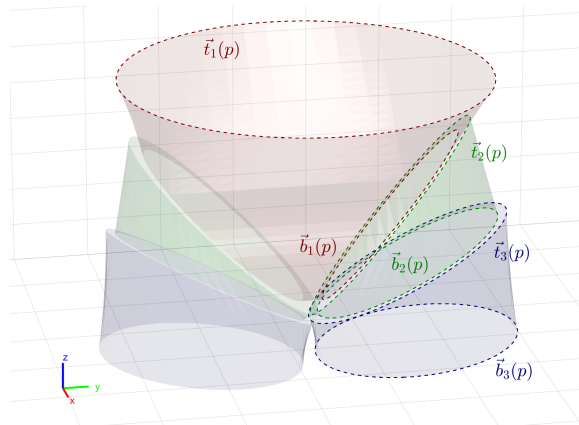


Figure 2-4: Figure showing edges for each component of an HCJA, using the HBA as an example. The top and bottom edges,  $\vec{t}_n(p)$  and  $\vec{b}_n(p)$ , respectively, are shown for each component. The color of the surface of each component, the top and bottom edges of that component, and the labels all match. The Briefs are red, the Proximal Section is green, and the Distal Section is blue. Only the edges of the components on the left side of the HBA are shown, as this model focuses on the left side. As symmetry is assumed in this model, the right side components are simple reflections of their counterparts. The global coordinate frame axes are also visible in the lower left.

When describing the circular edges of a component, the specific values of the parametric variable  $p$  in  $\vec{t}_n(p)$  and  $\vec{b}_n(p)$  do not matter, as moving  $p$  through the

interval  $[0, 2\pi)$  generates the same circular edge. A problem can arise, however, if one attempts to attribute significance to the points that  $\vec{t}_n(p)$  and  $\vec{b}_n(p)$  return for the same  $p$ . There is no inherent significance to the points on the edges for the same  $p$ . There is sometimes the need to determine corresponding points between the two edges, such as for generating the surfaces of HCJA components, as discussed in Section 2.4. In that case, there is a need for points on the top edge to correspond with points on the bottom edge, so they can be connected for the surface. Simply using the same values for  $p$  can result in absurd geometries.<sup>17</sup> A number of approaches could be used here, but this model relies on a rather simple one, dependent on the frame's  $\theta_n$  parameter. Determining the corresponding points between the two edges and thus rotationally aligning the two edges of a component can be done with the formulae<sup>18</sup>

$$\tau_n(p) = \begin{cases} ((p + \theta_n - \pi \lceil \frac{\theta_n}{\pi} \rceil) \bmod 2\pi) & \theta_n < \pi \\ ((p + \theta_n - \pi \lfloor \frac{\theta_n}{\pi} \rfloor) \bmod 2\pi) & \theta_n \geq \pi \end{cases}, \quad (2.7)$$

where  $\lceil * \rceil$  is the ceiling function and  $\lfloor * \rfloor$  is the floor function, and

$$\beta_n(p) = \begin{cases} ((p + \pi) \bmod 2\pi) & \cos \theta_n < 0 \\ (p \bmod 2\pi) & \cos \theta_n \geq 0 \end{cases}, \quad (2.8)$$

where  $p \in [0, 2\pi)$  is a parametric variable to find  $\tau$  and  $\beta$ , which can be used themselves as the parametric variables for  $\vec{t}_n(p)$  and  $\vec{b}_n(p)$ . In other words, to find the

---

<sup>17</sup>Connecting points between two parallel circles with a rotational offset is one way a hyperboloid of one sheet can be defined.

<sup>18</sup>The function for  $\tau_n(p)$  looks oddly complex, but it is much simpler to code. In MATLAB, if the parametric variable  $p$  is a vector of values  $\mathbf{p}$  and the parameter  $\theta_n$  is  $\text{thn}$ , then the code equivalent would be simply  $\mathbf{p} + \text{rem}(\text{thn} - \text{pi}, \text{pi})$ , where  $\text{rem}$  is MATLAB's remainder after division function and  $\text{pi}$  is  $\pi$ .

corresponding points on the two edges of a standard HCJA component,<sup>19</sup> compute

$$\vec{t}_n(\tau_n(p)) \quad \text{and} \quad \vec{b}_n(\beta_n(p))$$

for the same  $p \in [0, 2\pi)$ . To reduce confusion, it is simplest to always compute the top and bottom edge like this from the same  $p$ .

## 2.4 Surface Generation

To fully model the geometry of the HCJA, the overall shapes of the components must be described. This extension can be critical. In Chapter 3, for example, the shapes of the components are used to determine the range of motion for the suit's occupant. These shapes are also invaluable when visualizing the HCJA geometry.

The shape of each component is described as a two-dimensional surface in  $\mathbb{R}^3$ , defined by a set of points identified in a manner similar to the .STL file format. The .STL file, a common standard for describing three-dimensional structures, relies on a numbered set of points in  $\mathbb{R}^3$  and a list of triangular faces, each defined by the numbers of the three points that are its vertices [34]. While there are many ways to describe a surface, the .STL format was selected due to its ubiquity. The surfaces output from this model in this format can be imported into many different three-dimensional modeling programs. Similarly, analyses using this model, such as the one in Chapter 3, can be applied to .STL file data with no modification. There

---

<sup>19</sup>This approach is for standard HCJA components. In non-standard components, the rotational alignment of the top and bottom edges may be more complex, as more than one edge must be aligned. (The exception is a symmetric non-standard component with only two distal neighbors. See Section 2.4.2). The alignment described here is primarily used for generating the surfaces of the components. There is no standard method to generate the surfaces for non-standard components, and the method of aligning points along the various edges is a non-trivial part of each special method.

are also tools available to convert many other three-dimensional formats to .STL (SolidWorks and most other 3D design programs can save as .STL, for example), so analyses based off this model are compatible with many file types.

To create the .STL files, MATLAB three-dimensional surfaces were converted using a modified<sup>20</sup> version of the `surf2stl` function [19]. These MATLAB surfaces had to be generated, which required creating input acceptable to MATLAB's `surf` function. The MATLAB surface for each component requires three matrices,  $\mathbf{X}$ ,  $\mathbf{Y}$ , and  $\mathbf{Z}$  as input. These correspond to a  $x$ ,  $y$ , and  $z$  coordinates of the rectangular grid of points that make up the surface. The point in row  $i$  and column  $j$  (the  $(i, j)$ -th point) of the grid for component  $n$  is denoted by the vector<sup>21</sup>  $\vec{q}_{n:i,j}$ . The input matrices can thus be found as

$$\mathbf{X}_{i,j} = \begin{bmatrix} 1 \\ 0 \\ 0 \\ 0 \end{bmatrix} \cdot \vec{q}_{n:i,j}, \quad \mathbf{Y}_{i,j} = \begin{bmatrix} 0 \\ 1 \\ 0 \\ 0 \end{bmatrix} \cdot \vec{q}_{n:i,j}, \quad \text{and} \quad \mathbf{Z}_{i,j} = \begin{bmatrix} 0 \\ 0 \\ 1 \\ 0 \end{bmatrix} \cdot \vec{q}_{n:i,j}, \quad (2.9)$$

where  $\mathbf{A}_{i,j}$  denotes the element in the  $i$ -th row and  $j$ -th column of the matrix  $\mathbf{A}$ .

Points that are vertically or horizontally (but not diagonally) adjacent in this grid (and thus the input matrices) are connected with an edge. For example,  $\vec{q}_{n:3,5}$  would be adjacent to (and share an edge with)  $\vec{q}_{4,5}$  and  $\vec{q}_{3,6}$ , but not  $\vec{q}_{4,6}$ . Each

---

<sup>20</sup>The modifications were made for speed and efficiency. Some portions of this research (such as the tradespace explorations in Chapter 5) required performing these calculations on hundreds of thousands of geometries. To make that process more efficient, unused generalizations and input checking were removed from the code. To further reduce computation time, the code was modified in some cases to output the data as a pair of arrays containing .STL-formatted data, rather than saving every geometry as a file.

<sup>21</sup>The vectors  $\vec{q}_{n:i,j}$  are used to define component  $n$  and are expressed in coordinate frame  $n$  (though parts of their derivation may use other frames. Therefore, the frame-related notation of  ${}^n\vec{v}$  is normally extraneous and clutters the equations. Unless otherwise specified,  $\vec{q}_{n:i,j} = {}^n\vec{q}_{n:i,j}$ .



“square” of four entries in the grid, and the edges between them, are connected in the MATLAB surface to form a face. To create the surfaces, the grid of points  $\vec{q}_{n:i,j}$  for each component must be determined. The grids for standard and non-standard HCJA components are discussed further in Sections 2.4.1 and 2.4.2, respectively.

### 2.4.1 Standard Components

Standard components of the HCJA (those connected to exactly one component on each end, as described in Section 2.1), the creation of the surface grid of points  $\vec{q}_{n:i,j}$  is relatively simple. These components are oblique frusta (see Figure 2-1) and can be thought of similarly to deformed cylinders. Only points on the top and bottom edges must be defined, with surface edges in between. The only additional information required is the number of points on each component edge, denoted  $N_1$ ,<sup>22</sup> and the alignment of the top and bottom component edges. The value of  $N_1$  will be based on the accuracy required for the implementation of the model. The rotational alignment of the edges was determined using the functions  $\tau_n(p)$  and  $\beta_n(p)$ , described in Equations 2.7 and 2.8.

With only two rows of points (one each for the top and bottom component edges),  $\vec{q}_{n:i,j}$  is simple to describe. The index  $j$  values 1 and 2 (indicating top or bottom component edge), while  $i$  takes integer values between 0 and  $N_1$ , inclusive (indicates which point along component edges). Thus, the points can be defined by the formula

$$\vec{q}_{n:i,j} = \begin{cases} \vec{t}_n \left( \tau_n \left( \frac{2\pi j}{N_1} \right) \right) & j = 1 \\ \vec{b}_n \left( \beta_n \left( \frac{2\pi j}{N_1} \right) \right) & j = 2 \end{cases}, \forall i \in \{0, 1, \dots, N_1\}, \forall j \in \{1, 2\}.$$

---

<sup>22</sup>There were actually  $N_1 + 1$  points between 0 and  $2\pi$ , but when considering a circle, 0 and  $2\pi$  are equivalent, so there are only  $N_1$  distinct points.

Note that  $\vec{q}_{n:i,0} = \vec{q}_{n:i,N_1}$ . This makes the surface wrap around and close against itself. The surfaces for each standard component can then be found using MATLAB's `surf` function with input matrices defined according to Equation 2.9.

## 2.4.2 Non-standard Components

As stated in Section 2.1, the structural portions (both kinematic and physical) of this model defined in Sections 2.2 and 2.3 are applicable to both standard and non-standard components (with slight modifications to indexing and number of bottom edges) with little complexity. However, the difference is more significant when considering the surfaces of the components. The surfaces describing the overall shapes of standard components can be found with a consistent formula for its points, described in Section 2.4.1. The shapes of non-standard components, in contrast, can vary wildly based on the HCJA being modeled,<sup>23</sup> and a method of defining the surface points must be created for each specific usage. This section presents an example of such a method, generating the grid of points  $\vec{q}_{1:i,j}$  for the non-standard Briefs component of the Mark III HBA. The two-dimensional grid of points for the Briefs surface,  $\vec{q}_{n:i,j}$ , must be generated, but, due to the complexity of its shape, it cannot simply be two rows corresponding to the top and bottom edges.

Instead, working in the Briefs own coordinate frame, frame 1, the Briefs surface was divided into five regions:

- the under side, which connects portions of the left and right bottom edges of the Briefs to one another,
- the left side, which connects a portion of the left bottom edge to points on the

---

<sup>23</sup>For example, the shapes and surfaces of an HCJA for the shoulder, hips, knee, or hands would all look very different.

top edge,

- the right side, which connects a portion of the right bottom edge to points on the top edge,
- the back side, which connects a portion of the top edge to points on the under side, and
- the front side, which also connects a portion of the top edge to points on the under side.

The regions of the Briefs surface can be seen in Figure 2-5. These regions each form a sub-surface, which are combined to form the surface for the Briefs.

Some simplifications are applied. The Briefs are treated as symmetric across the sagittal plane,<sup>24</sup> so any point in the Briefs frame on the right half  ${}^1\vec{v}_R$  can be converted from the equivalent left-half vector,  ${}^1\vec{v}_L$  by changing the sign on the  $y_1$ -coordinate,<sup>25</sup> or:

$${}^1\vec{v}_R = \mathbf{R} {}^1\vec{v}_L, \text{ where } \mathbf{R} = \begin{bmatrix} 1 & 0 & 0 & 0 \\ 0 & -1 & 0 & 0 \\ 0 & 0 & 1 & 0 \\ 0 & 0 & 0 & 1 \end{bmatrix}. \quad (2.10)$$

This simplifies the physical structure of the Briefs. Only one bottom edge radius,  $r_{1b}$  is required, and the bottom edge on the left side is simply reflected across the sagittal plane to find the right side. The  $\tau_n(p)$  and  $\beta_n(p)$  index adjustments for the component edges, described in Equations 2.7 and 2.8, are used as well.

---

<sup>24</sup>The definition of the sagittal plane and other anatomical terms can be found in Appendix A.

<sup>25</sup>This term “ $y_1$ -coordinate” of a specific vector means the  $y$ -component of that vector, when that vector is expressed in frame in 1. The subscript means that it is measured along the  $y_1$  axis, no matter in what frame the vector is expressed. In other words, the  $y_n$  component for  $\vec{v}$  is equal to  ${}^n\vec{v} \cdot [0 \ 1 \ 0 \ 0]^T$ . This also can be applied to  $x$  and  $z$  axes.

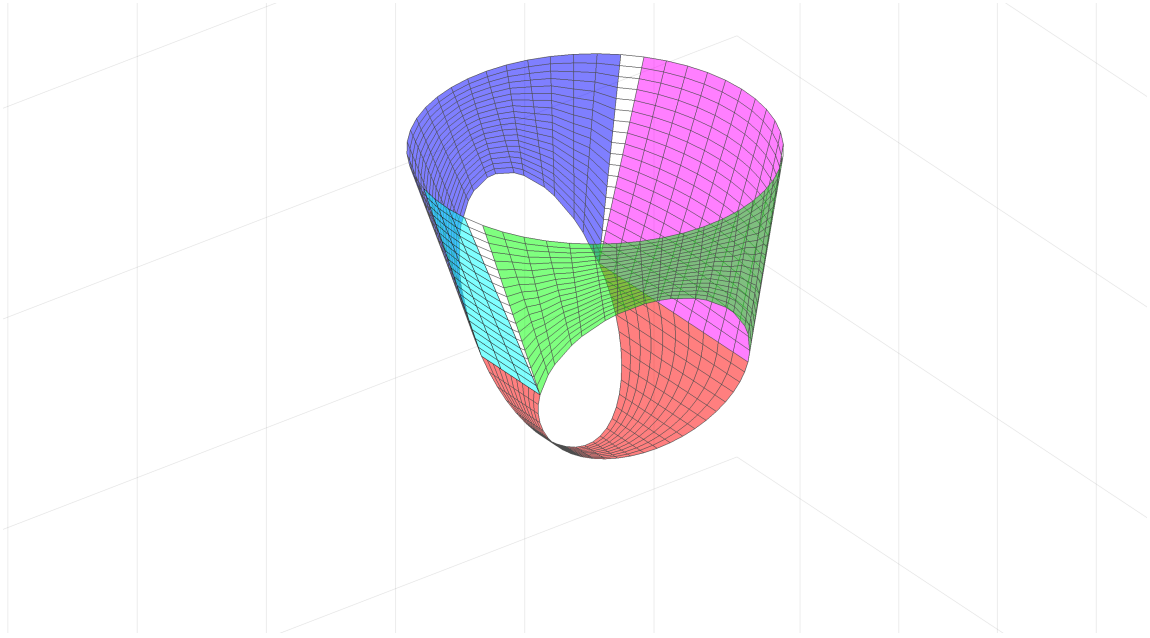


Figure 2-5: The surface generated for the Briefs of the Mark III HBA, with the different regions of the surface specified. The under side region is shown in red, the left side in green, the right side in blue, the back side in magenta, and the front side in cyan. Uncolored areas are the seams between the regions. The colors used match those in Figure 2-7, which shows the zones which determine the Briefs region for each top edge point.

The top edge of the Briefs component is divided according to the region each point joins. The bottom edges are divided between points that connect to the top edge, and those that connect with each other to form the under side. They form the bounds of the sub-surfaces, which are formed by interpolating between them.

As shown in Figure 2-5, portions of the top edge form parts of four different regions (left, right, front, and back). The region to which a top edge point belongs depends on the location of the point relative to several landmark points on the Briefs:

- the center of the top edge of the Briefs, which we call  $\vec{c}_{1t}$ ;
- the two points (denoted as  $\vec{f}_L$  and  $\vec{r}_L$ , for the fore- and rearmost of the pair,

respectively, using the  $x_1$ -coordinates) of the left<sup>26</sup> bottom edge which have  $z_1$ -coordinates equal to those of the centers of the bottom edges; and

- the two points (denoted as  $\vec{f}_R$  and  $\vec{r}_R$ , for the fore- and rearmost of the pair, respectively, using the  $x_1$ -coordinates) of the right<sup>27</sup> bottom edge which have  $z_1$ -coordinate equal to those of the centers of the bottom edges.

These landmark points are labeled in Figure 2-6.

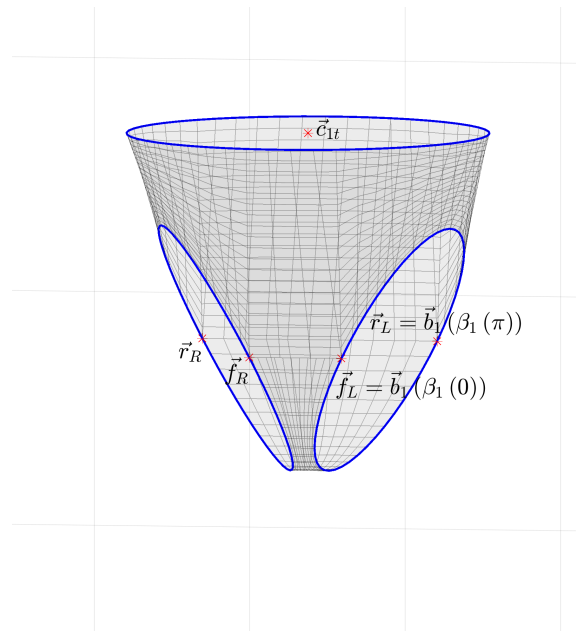


Figure 2-6: The edges for the Briefs of the Mark III HBA, with the generated surface visible and landmark points for Briefs surface generation labeled. The zones created from these points can be seen in Figure 2-7.

The landmark points are used to form a set of zones around the top edge, shown in Figure 2-7. The top edge points that fall into each zone are used to form a

<sup>26</sup>As stated in this section, this model assumes symmetry and is based on the left side. Thus, using the coordinate transformation formulae and given DH parameters finds the left bottom edge.

<sup>27</sup>Due to the symmetry assumption, the points in frame 1 on the right bottom edge for the Briefs can be found by taking the points for the left bottom edge and changing the sign on the  $y_1$ -coordinate. See previous footnote or Equation 2.10.

specific region of the Briefs. The conditions<sup>28</sup> defining these zones are summarized in Table 2.1. They can be defined as follows:

- Front side: Parallel to the  $y$ -axis of the Briefs frame,  $y_1$ , points must fall on or between  $\vec{f}_R$  and  $\vec{f}_L$ . Points must also be in the front half of the waist edge, with a greater  $x_1$ -coordinate than  $\vec{c}_{1t}$ .
- Left side: Points must either be in the front half of the waist edge ( $x_1$ -coordinate greater than or equal to  ${}^1\vec{c}_{1t}$ ) and fall on or outside  $\vec{f}_L$  (compared using  $y_1$ -coordinates), or be in the rear half of the waist edge ( $x_1$ -coordinate less than or equal to  $\vec{c}_{1t}$ ) and fall on or outside  $\vec{r}_L$  along the  $y_1$ -axis.
- Right side: Points must either be in the front half of the waist edge ( $x_1$ -coordinate greater than or equal to  $\vec{c}_{1t}$ ) and fall on or outside  $\vec{f}_R$  (compared using  $y_1$ -coordinates), or be in the rear half of the waist edge ( $x_1$ -coordinate less than or equal to that of  $\vec{c}_{1t}$ ) and fall on or outside  $\vec{r}_R$  along the  $y_1$ -axis.
- Back side: Points must either fall on or between  $\vec{r}_L$  and  $\vec{r}_R$  (compared using  $y_1$ -coordinates) and be in the back half of the waist edge, with an  $x_1$ -coordinate less than or equal to that of  $\vec{c}_{1t}$ .

As defined in Equation 2.4, the location of the points on the top edge themselves are defined by  $\vec{t}_1(\tau_n(p))$ . In frame 1, the center of the top edge is the origin, so  ${}^1\vec{c}_{1t} = \vec{0}$ . It can be shown (see Appendix D) that  ${}^1\vec{f}_L = {}^1\vec{b}_1(\beta_1(0))$  and  ${}^1\vec{r}_L = {}^1\vec{b}_1(\beta_1(\pi))$ . Given the symmetry assumption, right-side points  ${}^1\vec{f}_R$  and  ${}^1\vec{r}_R$

---

<sup>28</sup>We assume that  $\vec{r}_L$  (and thus  $\vec{r}_R$  as well) is in the rear half of the Briefs, with an  $x_1$ -coordinate less than or equal to that of  $\vec{c}_{1t}$ . An alternative method to describe the Briefs surfaces for cases where  $\vec{r}_L$  is in the front half of the Briefs, was created, but not finalized. With the bounds and constraints in Chapter 4, as well as the values of the radii, no such cases arose during this research.

<b>Region</b>	<b>Conditions for Point <math>\vec{t}_1(\tau_1(p))</math></b>
Front side	$-y_f \leq y_p \leq y_f$ and $x_p > 0$
Left side	$(y_p \geq y_f$ and $x_p \geq 0)$
	or $(y_p \geq y_r$ and $x_p \leq 0)$
Right side	$(y_p \leq -y_f$ and $x_p \geq 0)$
	or $(y_p \leq -y_r$ and $x_p \leq 0)$
Back side	$-y_r \leq y_p \leq y_r$ and $x_p \leq 0$

Note: The following shorthand is used:

$$\begin{aligned}
{}^1\vec{t}_1(\tau_1(p)) &= [x_p \quad y_p \quad z_p \quad 1]^T \\
{}^1\vec{f}_L &= {}^1\vec{b}_1(\beta_1(0)) = [x_f \quad y_f \quad z_f \quad 1]^T \\
{}^1\vec{r}_L &= {}^1\vec{b}_1(\beta_1(\pi)) = [h_r \quad y_r \quad z_r \quad 1]^T \\
{}^1\vec{f}_R &= [x_f \quad -y_f \quad z_f \quad 1]^T \\
{}^1\vec{r}_R &= [x_r \quad -y_r \quad z_r \quad 1]^T
\end{aligned}$$

Table 2.1: Conditions defining HBA Briefs top edge zones.

equal the equivalent left-side points with the sign changed on the  $y_1$ -coordinate, or

$${}^1\vec{f}_R = \mathbf{R} {}^1\vec{f}_L \quad \text{and} \quad {}^1\vec{r}_R = \mathbf{R} {}^1\vec{r}_L,$$

with  $\mathbf{R}$  defined according to Equation 2.10. These definitions simplify the assignment of top edge points to each region, resulting in the conditions given in Table 2.1.

Using the top edge points in each zone, we can generate the sub-surface for each region and combine them to form the Briefs surface. One aspect of the MATLAB `surf` function simplifies this: the function ignores values that are Not a Number (NaN), a data type in MATLAB that can be treated as a number for all calculations (though any operation between a NaN and a number or between two NaNs results in a NaN) and is therefore useful as a placeholder. This feature is utilized to avoid forcing the

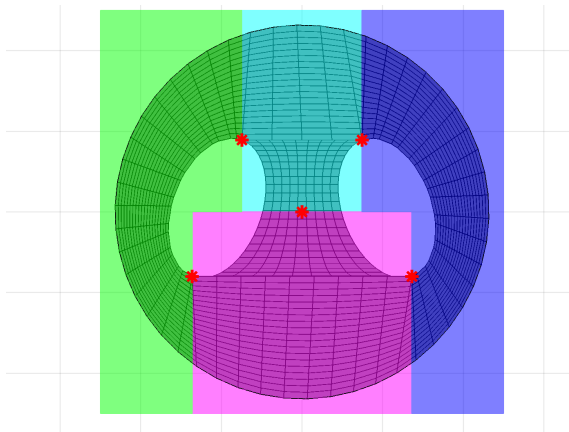


Figure 2-7: An illustration of the zones used to divide the Briefs top edge, with the corresponding regions indicated. The left side zone is in green, the right side in blue, the back side in magenta, and the front side in cyan. These colors match those in Figure 2-5, to show the surface regions of the top edge points in these zones. Also note the red stars, matching the points in Figure 2-6, that serve as the divisions between the zones.

grid of points,  $\vec{q}_{1:i,j}$ , to match the rectangular shape of the grid. Instead, a sort of “T” shape of relevant points fills part of the grid, with the unused areas filled with NaNs. The grid of surface points forms something like the bottom half of an infant’s onesie, where the tongue of the “T” (or flap of the onesie) is the under side of the Briefs, and the other four regions in the top bar across the “T” wrap around the waist. Rectangular blocks of NaNs under the top bar of the “T,” and on either side of the tongue of the “T,” correspond to the leg holes of the Briefs. The points on the grid around these NaN-blocks are the bottom edges of the Briefs, and the top line of the grid is the top edge of the Briefs. The leftmost and rightmost columns are identical, to force the surface to self-intersect and seal. The form of this grid can be seen in Figure 2-8.

Similar to Section 2.4.1, the circles forming both the top and bottom edges are



	$M_t + 1$			$M_b + 1$			$M_r + 1$			1
	$\bar{q}_{1t:0,0}$	$\bar{q}_{1t:1,0}$	$\dots$	$\bar{q}_{1t:M_t,0}$	$\bar{q}_{1b:0,0}$	$\bar{q}_{1b:1,0}$	$\dots$	$\bar{q}_{1r:0,0}$	$\bar{q}_{1f:0,0}$	$\bar{q}_{1t:0,0}$
	$\bar{q}_{1t:0,1}$	$\bar{q}_{1t:1,1}$	$\dots$	$\bar{q}_{1t:M_t,1}$	$\bar{q}_{1b:0,1}$	$\bar{q}_{1b:1,1}$	$\dots$	$\bar{q}_{1r:0,1}$	$\bar{q}_{1f:0,1}$	$\bar{q}_{1t:0,1}$
	$\vdots$	$\vdots$	$\ddots$	$\vdots$	$\vdots$	$\vdots$	$\ddots$	$\vdots$	$\vdots$	$\vdots$
	$\bar{q}_{1t:0,N_2}$	$\bar{q}_{1t:1,N_2}$	$\dots$	$\bar{q}_{1t:M_t,N_2}$	$\bar{q}_{1b:0,N_2}$	$\bar{q}_{1b:1,N_2}$	$\dots$	$\bar{q}_{1r:0,N_2}$	$\bar{q}_{1f:0,N_2}$	$\bar{q}_{1t:0,N_2}$
	NaN	NaN	$\dots$	NaN	$\bar{q}_{1u:0,0}$	$\bar{q}_{1u:1,0}$	$\dots$	NaN	NaN	NaN
	NaN	NaN	$\dots$	NaN	$\bar{q}_{1u:0,1}$	$\bar{q}_{1u:1,1}$	$\dots$	NaN	NaN	NaN
	$\vdots$	$\vdots$	$\ddots$	$\vdots$	$\vdots$	$\vdots$	$\ddots$	$\vdots$	$\vdots$	$\vdots$
	NaN	NaN	$\dots$	NaN	$\bar{q}_{1u:0,\frac{N_1}{2}}$	$\bar{q}_{1u:1,\frac{N_1}{2}}$	$\dots$	NaN	NaN	NaN

Figure 2-8: The arrangement of the grid of points used to make the Briefs surface. The colored boxes indicate the associated region of the surface, corresponding to the colors used in Figures 2-5 and 2-7. The under side region is shown in red, the left side in green, the right side in blue, the back side in magenta, and the front side in cyan. Grey areas correspond to areas that are left as NaN (a non-numeric placeholder value) so there is no surface at the leg holes.

divided into  $N_1$  equally-spaced points.<sup>29</sup> The value of  $N_1$  can change based on the implementation of the model. The bottom edge points<sup>30</sup> are at

$$\vec{b}_1 \left( \beta_1 \left( \frac{2\pi k}{N_1} \right) \right)$$

and the top edge points lie at

$$\vec{t}_1 \left( \tau_1 \left( \frac{2\pi k}{N_1} \right) \right),$$

where  $k$  is an integer between 0 and  $N_1$ , inclusive.

The top edge is divided into zones based on the regions each point will join, based on the conditions in Table 2.1 and Figure 2-7. The top edge points within each zone are then ordered such that they form a consistent circle as the top line of the grid of points defining the Briefs surface, as shown in Figure 2-8. We sort the top edge points that are in the left side zone, ordered with decreasing  $x_1$ -coordinates, to form the ordered set of points  $\vec{w}_{l,i}$ , where  $i$  is an integer between 0 and  $M_l$  (inclusive). There are a total of  $M_l + 1$  points of top edge points in the left side zone, all included in this set. We arrange the points in the other three top edge zones like this, so the  $M_b + 1$  points in the back side zone are ordered with decreasing  $y_1$ -coordinates to form  $\vec{w}_{b,i}$ , the  $M_r + 1$  points in the right side zone ordered with increasing  $x_1$ -coordinates as  $\vec{w}_{r,i}$ , and the  $M_f + 1$  points on the front side zone ordered by increasing  $y_1$ -coordinates as  $\vec{w}_{f,i}$ . The ordering of each region results in a continuous progression of points around the top edge that is anticlockwise if viewed from above. An example of these points (with  $N_1 = 50$ ,  $M_f = 4$ ,  $M_r = 17$ ,  $M_b = 9$ , and  $M_l = 16$ ) can be seen in Figure 2-9.

---

<sup>29</sup>Also similar to Section 2.4.1, there are actually  $N_1 + 1$  points between 0 and  $2\pi$ , but the first and last overlap.

<sup>30</sup>For the left side. The right side bottom edge points are the same, but with the sign of the  $y_1$ -coordinate's sign changed. See Equation 2.10.

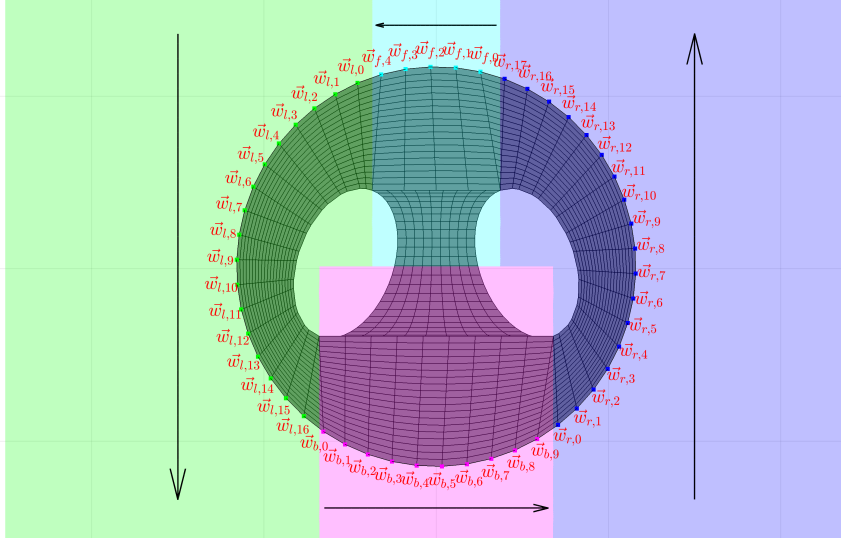


Figure 2-9: Point groupings by zone of Briefs top edge points for  $N_1 = 50$ ,  $M_f = 4$ ,  $M_r = 17$ ,  $M_b = 9$ , and  $M_l = 16$ . The colors of the top edge points (the squares) and the color-coded regions match the colors in Figures 2-5, 2-7, and 2-8. The black arrows indicate the direction in which points are sorted for each zone.

Like the top edge, the bottom edges must be divided, but in a much simpler manner. They are divided based which points will join the under side and which will join one of the other regions. This division splits the set of points in half.<sup>31</sup> The lower half of the bottom edges (those with  $z_1$ -coordinates less than or equal to the  $z_1$ -coordinate of the bottom edge center) are connected to their equivalent points on the opposite leg hole to form the under side region of the Briefs. The upper halves of these edges (points with  $z_1$ -coordinates greater than or equal to the  $z_1$ -coordinate of the bottom edge center) are connected to the left and right side regions of the Briefs. As shown in Appendix D,  ${}^1\vec{b}_n(\beta_n(0))$  and  ${}^1\vec{b}_1(\beta_1(\pi))$  are the points with the same  $z_1$ -coordinate as the bottom edge's center. The upper half are the points with integer indices  $i \in \{0, 1, \dots, \frac{N_1}{2}\}$ . The points in the lower half of the Briefs bottom

<sup>31</sup>The two points which define the dividing line,  $\vec{f}_L$  and  $\vec{r}_L$  for the left bottom edge and  $\vec{f}_R$  and  $\vec{r}_R$  for the right bottom edge, are both used in both halves.

edge correspond to integer indices  $i \in \{\frac{N_1}{2}, \frac{N_1}{2} + 1, \dots, N_1\}$ . For this reason, we only use even values for  $N_1$ .

With the top and bottom edges divided by region, the edges are connected to form the sub-surfaces. A second dimension of this surface is required (beyond the points-per-edge  $N_1$ ): the number of points, denoted  $N_2$ , between the top edge of the Briefs and the bottom edges. With this value, we can define the points of each sub-surface as a rectangular sub-grid of points (Figure 2-8) by interpolating between the edges of the region.

The front side is the simplest. The top line of this sub-grid of points runs along the Briefs top edge as  $\vec{w}_{f,i}$ , with  $i$  varying from 0 to  $M_f$  (inclusive). The bottom of this sub-grid as the same number of points ( $M_f + 1$ ) and runs between  $\vec{f}_R$  and  $\vec{f}_L$ . The bottom line is found by interpolating:

$$\vec{f}_R \frac{i}{M_f} + \vec{f}_L \frac{(1-i)}{M_f}.$$

By interpolating between the top and bottom lines of the grid, we can find the points on the front side sub-surface, denoted  $\vec{q}_{1f:i,j}$ . The formula is

$$\vec{q}_{1f:i,j} = \vec{w}_{f,i} \frac{(1-j)}{N_2} + \left( \vec{f}_R \frac{i}{M_f} + \vec{f}_L \frac{(1-i)}{M_f} \right) \frac{j}{N_2},$$

where  $j$  is an integer between 0 and  $N_2$ , inclusive, and  $i$  is an integer between 0 and  $N_1$ , also inclusive.

The back side is similar to the front, connecting the  $M_b + 1$  points on the top edge in  $\vec{w}_{b,i}$  to the interpolated line between  $\vec{r}_R$  and  $\vec{r}_L$ . The interpolated bottom line is:

$$\vec{r}_L \frac{i}{M_b} + \vec{r}_R \frac{(1-i)}{M_b}.$$

By interpolating between the top and bottom line, we can find the points on the back side sub-surface, denoted  $\vec{q}_{1b:i,j}$ . The formula is

$$\vec{q}_{1b:i,j} = \vec{w}_{b,i} \frac{(1-j)}{N_2} + \left( \vec{r}_L \frac{i}{M_b} + \vec{r}_r \frac{(1-i)}{M_b} \right) \frac{j}{N_2},$$

where  $i$  is an integer between 0 and  $N_1$ , inclusive, and  $j$  is an integer between 0 and  $N_2$ , also inclusive.

The left side connects the  $M_l + 1$  left side top edge points in the left side zone,  $\vec{w}_{l,i}$ , to the upper half of the left bottom edge. Unlike the front and back sides, these sets do not inherently contain the same number of points. There are more points in the top half of the leg hole, so they cannot connect one-to-one. Therefore, we need to adjust the indices of the connections. The top edge has  $M_l + 1$  points and the upper half of the bottom edge has  $\frac{N_1}{2} + 1$  points. We adjust the index of the connections by the ratio of the number of points,  $\frac{\frac{N_1}{2} + 1}{M_l + 1}$ . This gives us the formula

$$\vec{q}_{1l:i,j} = {}^1\vec{w}_{l,i} \frac{(1-j)}{N_2} + {}^1\vec{b}_1 \left( \beta_1 \left( \frac{2\pi i}{N_1} \left[ \frac{\frac{N_1}{2} + 1}{M_l + 1} \right] \right) \right) \frac{j}{N_2},$$

where  $i$  is an integer between 0 and  $M_l$ , inclusive,  $j$  is an integer between 0 and  $N_2$ , also inclusive, and  $[*]$  indicates rounding to the nearest integer.

The right side is found similarly, though the indices are reversed. This gives<sup>32</sup>

$$\vec{q}_{1r:i,j} = {}^1\vec{w}_{r,i} \frac{(1-j)}{N_2} + \mathbf{R} {}^1\vec{b}_1 \left( \beta_1 \left( \frac{2\pi}{N_1} \left( \frac{1}{2} - i \left[ \frac{\frac{N_1}{2} + 1}{M_r + 1} \right] \right) \right) \right) \frac{j}{N_2}$$

where  $i$  is an integer between 0 and  $M_r$ , and  $j$  is an integer between 0 and  $N_2$ .

---

<sup>32</sup>Note that this is using the right side  $\vec{b}_1$ , while the Briefs are parameterized based on the left side. This is the same as all other uses, but the sign on the  $y_1$ -coordinate is changed. To achieve this, the matrix  $\mathbf{R}$  as defined in Equation 2.10 is included.

inclusive.

Finally, the under side can be described. It interpolates between the bottom halves of the bottom edges. Horizontally, it has  $M_b + 1$  points, so it can match the points in the middle part of the back side region and fit into the grid of points. The formula is

$$\vec{q}_{1u:i,j} = {}^1\vec{b}_1 \left( \frac{2\pi(\frac{N_1}{2} + j)}{N_1} \right) \frac{i}{M_P} + \mathbf{R} {}^1\vec{b}_1 \left( \frac{2\pi(\frac{N_1}{2} + j)}{N_1} \right) \frac{(1-i)}{M_b},$$

where  $i$  is an integer between 0 and  $M_{2b}$ , and  $j$  is an integer between 0 and  $\frac{N_1}{2}$ , both inclusive. These sub-grids of points,  $\vec{q}_{1f}$ ,  $\vec{q}_{1l}$ ,  $\vec{q}_{1r}$ ,  $\vec{q}_{1b}$ , and  $\vec{q}_{1u}$ , are then arranged as shown in Figure 2-8. With the grid of points defined, the surface for the Briefs can be found using MATLAB's `surf` function with input matrices defined according to Equation 2.9. Similar approaches can be derived for other non-standard HCJA components.

## 2.5 Bearings

In this model, the bearings are considered differently than the rigid components which they connect. While physically critical, they have little impact on the overall geometry of the HCJA. They are placed between components, are aligned with the axes of rotation, and do not add new reference frames or alter the structure of the model. However, the geometry of the bearings themselves can be important in answering certain questions. For example, when studying the mobility of the occupant of a suit (see Section 3.2.2), bearings are considered because their presence inside the HCJA would restrict the occupant. Answering this, and other questions, motivates describing the bearing geometry inside the HCJA model.

Each bearing, which we will identify using the index  $n/n + 1$ ,<sup>33</sup> exists between the components  $n$  and  $n + 1$  in the RBT described in Section 2.2. As the bearings are treated as circles (and thus rotating with one frame or the other does not affect their geometry), there is no significance to the component frame in which the bearing is placed.<sup>34</sup> Like the bottom edge circle of component  $n$  and the top edge circle of component  $n + 1$ , which should be very close to it, the  $n/n + 1$  bearing is located centered around and normal to the axis of the relevant joint,  $z_{n+1}$ .

The bearing is modeled as a ring or annular cylinder. For bearing  $n/n + 1$ , the two radii are  $r_{nb}$  and  $r_{(n+1)t}$ , so that the bearing has the same radii as the components to which it connects. Either component can provide the internal and external radii. To preserve generality, we will not assign one to be internal or external and instead call these  $r_{n/n+1;I}$  and  $r_{n/n+1;E}$ , respectively. The bearing also requires a height, represented by variable  $l_{n/n+1}$ . As the bearing is defined with respect to frame  $n + 1$ , and is centered around and normal to  $z_{n+1}$ , the only other parameter necessary to define the bearing is the distance along the  $z$ -axis from the origin (this is exactly like the  $h_{n/n+1}$  parameter for the top edges of each component in Section 2.3). This parameter, which we can call  $g_{n/n+1}$ , should be equal to  $h_{n/n+1}$ .

The bearing, unlike the other components, is not treated as a infinitely-thin surface. Therefore, while other components have two edges, the bearings each have four. We will call the functions describing the points on these edges  $\vec{b}_{n/n+1;I}(p)$  and  $\vec{b}_{n/n+1;E}(p)$  for the bottom inner and outer edges, respectively, and  $\vec{t}_{n/n+1;I}(p)$  and  $\vec{t}_{n/n+1;E}(p)$  for the top inner and outer edges, respectively. Note that  $p$  is, once again,

---

<sup>33</sup>This uses the same naming convention as the  $h_{n/n+1}$  parameters in Section 2.2, because the bearings and that parameter interact with both components  $n$  and  $n + 1$ .

<sup>34</sup>For non-dynamics applications. If dynamics and mass or inertia properties are being considered, the component frame in which the bearing is placed is important, but that is beyond the scope of this thesis.

the parametric variable to define each function, and should vary between 0 and  $2\pi$ .

The edges are

$$\vec{b}_{n/n+1;I}(p) = \begin{bmatrix} r_{n/n+1;I} \cos p \\ r_{n/n+1;I} \sin p \\ g_{n/n+1} + l_{n/n+1} \\ 1 \end{bmatrix}, \quad \vec{b}_{n/n+1;E}(p) = \begin{bmatrix} r_{n/n+1;E} \cos p \\ r_{n/n+1;E} \sin p \\ g_{n/n+1} + l_{n/n+1} \\ 1 \end{bmatrix},$$

$$\vec{t}_{n/n+1;I}(p) = \begin{bmatrix} r_{n/n+1;I} \cos p \\ r_{n/n+1;I} \sin p \\ g_{n/n+1} \\ 1 \end{bmatrix}, \quad \text{and} \quad \vec{t}_{n/n+1;E}(p) = \begin{bmatrix} r_{n/n+1;E} \cos p \\ r_{n/n+1;E} \sin p \\ g_{n/n+1} \\ 1 \end{bmatrix}.$$

Like in Section 2.4, the parameter  $N_1$ , the number of points used to define the circles that are the edges, is required to generate the bearing surfaces.<sup>35</sup>

The bearing surface is constructed using the MATLAB `surf` function in the same manner described in Section 2.4. The points which form the input matrices are called  $\vec{q}_{n/n+1:i,j}$ , where  $n/n+1$  is the bearing identifier and  $i$  and  $j$  are the matrix indices. The points are ordered:

1. along the outside face from the bottom outer edge to the top outer edge,
2. along the top face from the top outer edge to the top inner edge,
3. along the inside face from the top inner edge to the bottom inner edge, and
4. along the bottom face from the bottom inner edge back to the bottom outer edge.

---

<sup>35</sup>As discussed in Section 2.4, there are  $N_1 + 1$  points used, but 0 and  $2\pi$  are equivalent.



For this surface definition, there is no advantage to using extra points on each face between the edges, so only the edge points are needed. The formula for the points of the surface matrices is thus

$$\vec{q}_{n/n+1:i,j} = \begin{cases} \vec{b}_{n/n+1;E} \left( \frac{2\pi i}{N_1} \right) & j = 1 \\ \vec{t}_{n/n+1;E} \left( \frac{2\pi i}{N_1} \right) & j = 2 \\ \vec{t}_{n/n+1;I} \left( \frac{2\pi i}{N_1} \right) & j = 3 \\ \vec{b}_{n/n+1;I} \left( \frac{2\pi i}{N_1} \right) & j = 4 \\ \vec{b}_{n/n+1;E} \left( \frac{2\pi i}{N_1} \right) & j = 5 \end{cases}$$

where  $j$  is an integer between 1 and 5, inclusive, and  $i$  is an integer between 0 and  $N_1$ , also inclusive.

The surface for each bearing in the HCJA can then be found using MATLAB's `surf` function with input matrices defined according to Equation 2.9.



## Chapter 3

# Multi-Degree-of-Freedom Range of Motion Testing

As discussed in Chapter 1, the hard-component joint assemblies (HJCA) of hard-joint suits can affect the occupant's range of motion (ROM) and negatively impact mobility. An approach was developed to quantify and measure that impact, based on comparing the unsuited and suited multi-degree-of-freedom (MDoF) ROMs for the occupant's joint corresponding to the HJCA under consideration.<sup>1</sup> The comparison is performed by treating the center of rotation of the occupant's joint as the origin of a unit sphere, with the limb segment immediately distal to the joint treated as a unit vector. When considered in this manner, every position of the joint can be imagined as both a unit vector and point on the surface of the unit sphere. The ROMs thus can be defined as a region or shape on the surface of the unit sphere.

To use this comparison method, the ROMs must first be described as unit vectors

---

<sup>1</sup>This research focuses on ranges of motion with two degrees of freedom. A single-DoF ROM is simply the comparison of one-dimensional angular ranges. It might be possible to extend the approach presented here to systems with three DoFs (perhaps using quaternions instead of spherical coordinates), but that is not examined here.

or points on the unit sphere surface. Sections 3.1 and 3.2, respectively, detail the specifics of Unsuiting and Suited ROM calculation in this form. The comparison method itself is described in Section 3.3.

### 3.1 Unsuiting Range of Motion

The Unsuiting ROM is the control for the comparison method described in this chapter. It is the nominal ROM for the occupant's joint corresponding to the HCJA, when unsuited and unencumbered. The Unsuiting ROM of the joint can be calculated either for specific tasks (such as the ROM of the hip used during gait, the ROM of the knee used in kneeling, the ROM of the wrist used in sample collection, or similar definitions) or for the joint's entire possible motion envelope (the full range angles of the shoulder, hip, wrist, or other joint usable when unsuited). In either case, the ROM bounds must be described as unit vectors to be compatible with the comparison method described in Section 3.3. The exact method of conversion depends on the manner in which the ROM is initially described. The remainder of this section is an example of Unsuiting ROM calculation, showing the conversion of the hip position angular ranges (one common method of describing ROM in literature) for nominal gait to an Unsuiting ROM.

We begin with the angular bounds of hip position used during gait. These values were sourced from the Clinical Gait Analysis Normative Gait Database [17]. The bounds are defined by the maximum flexion, extension, abduction, and adduction used in a nominal human gait, presented in Table 3.1.<sup>2</sup>

These angles are converted to unit vectors by using them to rotate a unit vector

---

<sup>2</sup>The definition of these terms can be found in Appendix A.

	Maximum Value (°)	Converted Value (°)
<b>Flexion</b>	40	-40
<b>Extension</b>	10	10
<b>Abduction</b>	5	5
<b>Adduction</b>	10	-10

Table 3.1: The extreme values for human gait, used to define the necessary ROM [17]. Flexion and adduction values have negative signs that were not present in the source, which were added to indicate the direction.

initially pointing in the  $-\tilde{z}$  direction.<sup>3</sup> This unit vector is first rotated around the positive  $\tilde{x}$ -axis by the converted ab/adduction angle, then rotated around the original  $\tilde{y}$ -axis by the converted flexion/extension angle. This conversion is demonstrated in Figure 3-1. It should be noted that this approach differs from the standard established by the International Society of Biomechanics (ISB), where rotation is intrinsic instead of extrinsic<sup>4</sup> and flexion/extension is applied before ab/adduction [39].<sup>5</sup>

To define the Unsuit ROM, these rotations are applied to all four combinations of flexion/extension and ab/adduction. Rotation matrices corresponding to rotations about the  $\tilde{y}$ -axis are created for extension and flexion:

$$R_{\text{flex}} = \begin{bmatrix} \cos \psi_{\text{flex}} & 0 & \sin \psi_{\text{flex}} \\ 0 & 1 & 0 \\ -\sin \psi_{\text{flex}} & 0 & \cos \psi_{\text{flex}} \end{bmatrix} \quad \text{and} \quad R_{\text{ext}} = \begin{bmatrix} \cos \psi_{\text{ext}} & 0 & \sin \psi_{\text{ext}} \\ 0 & 1 & 0 \\ -\sin \psi_{\text{ext}} & 0 & \cos \psi_{\text{ext}} \end{bmatrix}.$$

---

<sup>3</sup>In Chapters 2 and 4, various specific definitions for the axes and unit vectors parallel to axes are used. To specify the axes that are not part of a physical model, we use the  $\tilde{x}$  mark. These are used mainly when calculating and rotating ROM unit vectors.

<sup>4</sup>For intrinsic rotations, each rotation is about the axes of the current frame. These axes themselves may have been rotated by the previous rotations. In extrinsic rotation, every rotation is applied about the original coordinate frame axes.

<sup>5</sup>The approach used here also discounts internal and external rotation of the hip, as well as any translation of the hip joint.

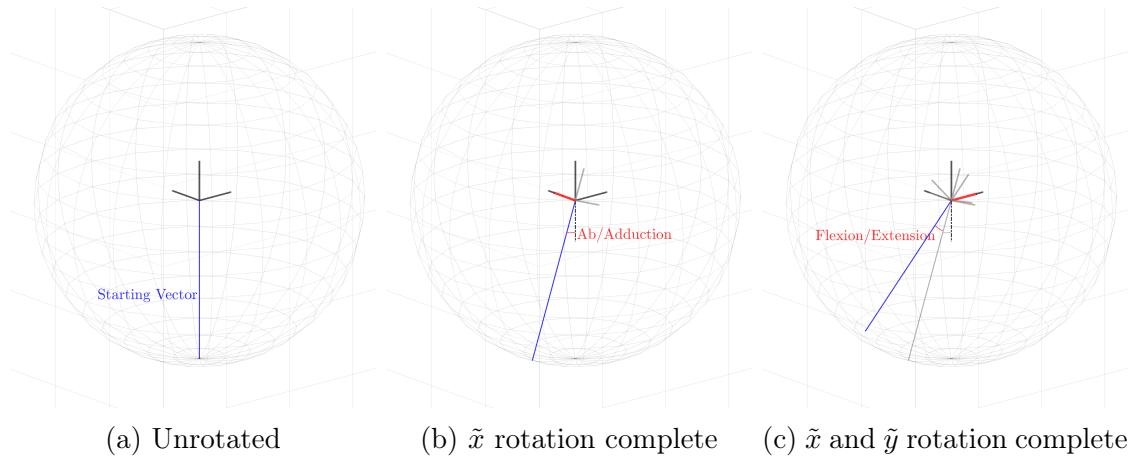


Figure 3-1: Visual representation of the convention used to transform converted flexion/extension and ab/adduction angles to a vector in  $\mathbb{R}^3$ . The blue line is the vector representing the “leg” as each rotation is applied. The rotation is indicated by a red arc, and the rotation’s axis is also highlighted in red.

Similarly, rotation matrices corresponding to rotations about the  $\tilde{x}$ -axis are created for abduction and adduction:

$$R_{ab} = \begin{bmatrix} 1 & 0 & 0 \\ 0 & \cos \psi_{ab} & -\sin \psi_{ab} \\ 0 & \sin \psi_{ab} & \cos \psi_{ab} \end{bmatrix} \quad \text{and} \quad R_{ad} = \begin{bmatrix} 1 & 0 & 0 \\ 0 & \cos \psi_{ad} & -\sin \psi_{ad} \\ 0 & \sin \psi_{ad} & \cos \psi_{ad} \end{bmatrix}.$$

Applying the rotation convention shown in Figure 3-1 yields the four vectors

$$R_{ext}R_{ad} \begin{bmatrix} 0 \\ 0 \\ -1 \end{bmatrix} = \begin{bmatrix} -\sin \psi_{ext} \cos \psi_{ad} \\ \sin \psi_{ad} \\ -\cos \psi_{ext} \cos \psi_{ad} \end{bmatrix}, \quad R_{flex}R_{ad} \begin{bmatrix} 0 \\ 0 \\ -1 \end{bmatrix} = \begin{bmatrix} -\sin \psi_{flex} \cos \psi_{ad} \\ \sin \psi_{ad} \\ -\cos \psi_{flex} \cos \psi_{ad} \end{bmatrix},$$

$$R_{\text{flex}}R_{\text{ab}} \begin{bmatrix} 0 \\ 0 \\ -1 \end{bmatrix} = \begin{bmatrix} -\sin \psi_{\text{flex}} \cos \psi_{\text{ab}} \\ \sin \psi_{\text{ab}} \\ -\cos \psi_{\text{flex}} \cos \psi_{\text{ab}} \end{bmatrix}, \quad \text{and} \quad R_{\text{ext}}R_{\text{ab}} \begin{bmatrix} 0 \\ 0 \\ -1 \end{bmatrix} = \begin{bmatrix} -\sin \psi_{\text{ext}} \cos \psi_{\text{ab}} \\ \sin \psi_{\text{ab}} \\ -\cos \psi_{\text{ext}} \cos \psi_{\text{ab}} \end{bmatrix}.$$

These four unit vectors, shown in Figure 3-2, define the bounds of the Unsuitied gait hip ROM.

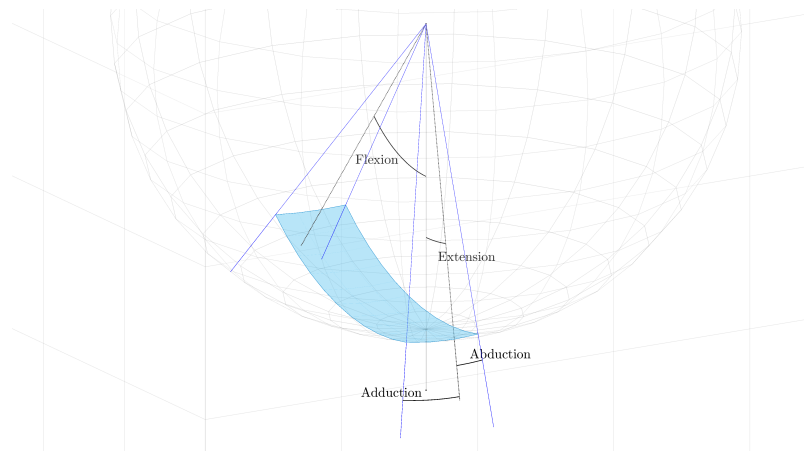


Figure 3-2: The Unsuitied hip ROM for gait, represented as a region on the surface of the sphere. The light blue box is the Unsuitied ROM, with the darker blue lines at each of the corners indicating the vectors of the four extrema used to create that box. Labeled black arcs indicate the angles of flexion/extension and ab/adduction defining the ROM.

## 3.2 Suited Range of Motion

The Suited ROM is the envelope of the motions available to the occupant when limited by the HCJA. Unlike its Unsuitied counterpart, the Suited ROM always

describes the total motion envelope available to the occupant’s joint.<sup>6</sup> This measurement includes all HCJA poses, so that all possible motions of the occupant’s joint are considered. The term “poses” here refers to a kinematic configuration of the different HCJA components. A pose can be specified by indicating an angular displacement for every bearing in the HCJA. If using the model from Chapter 2, a pose can be described by specifying  $\phi_1, \phi_2, \dots, \phi_{N_{DoF}}$ , where  $N_{DoF}$  is the number of DoFs in the HCJA.

The ROM could be measured experimentally or gathered from literature. In those cases, the Suited ROM should be approached in the same manner as the Unsited ROM in Section 3.1 and converted directly to unit vectors. However, space suits are expensive and testing can be difficult or time-consuming. Experimental verification is also difficult to use during the design process, as it may not be feasible to prototype every various design under consideration. A more general approach was developed, described in this section, which estimates the Suited ROM for an HCJA with arbitrary geometry. The estimation is approached by considering the space of possible poses of the HCJA, estimating the position of the occupant’s limb, and testing for intersection between the limb and suit. To test for intersection, the limb must be simulated for every pose. This topic is further discussed in Section 3.2.1. The detailed explanation of the Suited ROM calculation can be found in Section 3.2.2.

---

<sup>6</sup>Even if the Unsited ROM is task-based, the total ROM is used for the Suited ROM. The methodology described in this chapter is designed to evaluate how a suit impacts the motion of the occupant. Always using the total ROM avoids making assumptions about the occupant’s strategy or experience. For example, the way the occupant performs a task might change in the suit due to problems with visibility instead of motion restrictions.



### 3.2.1 Simulated Limb

When analyzing the Suited ROM, HCJA poses where the occupant's body would be forced to pass through the HCJA surfaces must be detected so body positions for those poses are not counted as part of the ROM.<sup>7</sup> To detect these cases when estimating the Suited ROM (see Section 3.2.2), the relevant body parts must be simulated for every HCJA pose considered.

Several simplifications were applied:

- Only one body part is considered for the HCJA: the limb (or limb segment) immediately distal to the occupant's joint, from the joint to the end of the limb (or next major joint). For example, if the HCJA is around the hips, the limb is the thigh; an HCJA about the knee has a limb corresponding to the shank and foot; and the limb for an HCJA around the wrist is the hand.<sup>8</sup>
- The limb is assumed to have a single specific position for every HCJA pose.
- The simulated limb is composed of two pieces used to estimate Suited ROM: a set of line segments indicating the limb's shape and a pair of points indicating the limb's orientation.
- The limb is assumed to be a constant shape, independent of motion and orientation. This shape is represented by a set of line segments. The positions of the line segments in the global frame must be entirely specified by HCJA position.

---

<sup>7</sup>In a physical suit, the body would not actually pass through the HCJA. Instead, the occupant-suit system would simply not be able to assume the pose.

<sup>8</sup>The definition of where the limb ends, is dependent on the implementation of the model. For example, the ankle may or not be a major joint for different questions.

- The limb's orientation can be described by two points: the base point, corresponding to the base of the limb at occupant's relevant joint and the tip point at the opposite end of the limb. As the limb position is determined entirely by the HCJA pose, these points (in the global frame) must be functions of the HCJA pose.

The base and tip points, which we will call  $\vec{v}_{\text{base}}$  and  $\vec{v}_{\text{tip}}$ , are critical to defining the Suited ROM. As functions of the HCJA pose (which can be represented by an angle for each of the  $N_{DoF}$  bearings in the HCJA), they can be described as

$${}^m\vec{v}_{\text{base}} = {}^m\vec{F}_{\text{base}}(\phi_1, \phi_2, \dots, \phi_{N_{DoF}})$$

and

$${}^n\vec{v}_{\text{tip}} = {}^n\vec{F}_{\text{tip}}(\phi_1, \phi_2, \dots, \phi_{N_{DoF}}),$$

where  $m$  and  $n$  are frames in the HCJA and the  $\vec{F}(\ast)$  functions, indicating the point locations in the respective frames, depend on the limb and HCJA under consideration. The frames of vectors  $\vec{v}_{\text{base}}$  and  $\vec{v}_{\text{tip}}$ ,  $m$  and  $n$  respectively, are important to consider. The points may be simple to describe in some frames, but complex in others.<sup>9</sup> The values of  $m$  and  $n$  are also bounded. It is required that  $m \geq 0$  and  $n \geq 0$ , as frames are not defined for values less than 0 and  $n \geq m$ , because  $n$  defines tip of the limb,  $m$  indicates the base of the limb, and the tip must be distal to the base. We also know  $m \leq N_{DoF}$  and  $n \leq N_{DoF}$ , because the positions of the tip and base must be expressed in the global frame based solely on the HCJA pose. If the points were expressed in a frame with an index greater than  $N_{DoF}$ , they would be in a frame that is not part of the HCJA and their position would depend on other

---

<sup>9</sup>For example, one simple method is to define a point in frame 0 as the base point and a point in frame  $N_{DoF}$  as the tip point. The functions are constants in those frames, but complex in others.

factors (such as the rotation of other frames in the suit).<sup>10</sup>

To be used in Section 3.2.2, these vectors should be converted to the global frame, which is performed using the transformations

$${}^0\vec{v}_{\text{base}} = {}^0T_1 J(\phi_1) {}^1T_2 J(\phi_2) \dots {}^{m-1}T_m J(\phi_m) {}^m\vec{F}_{\text{base}}(\phi_1, \phi_2, \dots, \phi_{N_{DoF}})$$

and

$${}^0\vec{v}_{\text{tip}} = {}^0T_1 J(\phi_1) {}^1T_2 J(\phi_2) \dots {}^{n-1}T_n J(\phi_n) {}^n\vec{F}_{\text{tip}}(\phi_1, \phi_2, \dots, \phi_{N_{DoF}}).$$

The vector between these points is used to describe the orientation of the limb (and thus the position of the human's joint). That vector,

$${}^0\vec{v}_{\text{tip}} - {}^0\vec{v}_{\text{base}},$$

is used in Section 3.2.2 in the estimation of the Suited ROM.

The other details of the simulated limb, including the line segments used to represent the limb's surface, cannot be universally defined, but will depend on the purpose of the experiment as well as the HCJA and limb under consideration. The remainder of this section contains an example of a simulated limb: the thigh used with the Mark III Hip Bearing Assembly (HBA).

For the HBA Suited ROM estimation, the limb under consideration was the thigh. The thigh reaches from the base point at the hip to the tip point at the knee. The base point is the centroid of the upper bearing and the tip point is located a constant distance from the origin of frame 4, as can be seen in Figure 3-3.

For this analysis, the distance was the value in the nominal Mark III geometry.

---

<sup>10</sup>There is one exception to this bound: if the tip point falls on the  $z$ -axis of the frame immediately distal to the HCJA ( $z_{N_{DoF}+1}$ ), the point can be expressed in the  $N_{DoF} + 1$  frame, because the rotation of that frame is about  $z_{N_{DoF}+1}$ , so the point would not be affected by the rotation.

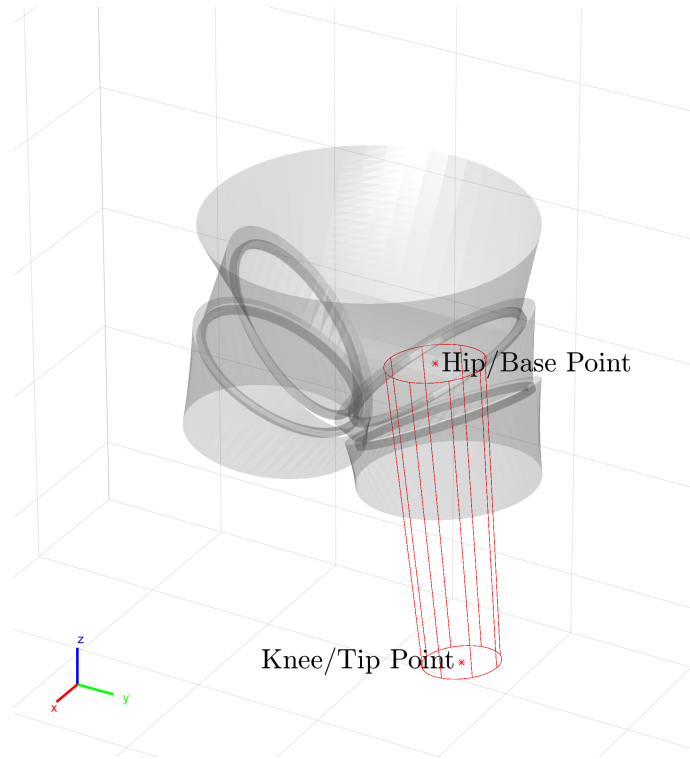


Figure 3-3: The simulated thigh inside the HBA model. The dots at either end represent the base and tip points, and the long lines running between them are the line segments use to simulate the shape.

Using that value, the tip point is positioned in frame 4 (thigh frame) at

$${}^4\vec{v}_{\text{tip}} = \begin{bmatrix} 0 \\ 0 \\ -0.3759 \text{ m} \end{bmatrix}.$$

Note that while  $N_{DoF} = 3$  for the Mark III HBA, the point can be defined in the frame distal to the HCJA under consideration, as it falls on the  $z$ -axis of that frame

and is unaffected by that frame's rotation. In the global frame, this vector is

$${}^0\vec{v}_{\text{tip}} = {}^0T_1 J(\phi_1) {}^1T_2 J(\phi_2) {}^2T_3 J(\phi_3) {}^3T_4 J(\phi_4) \begin{bmatrix} 0 \\ 0 \\ -0.3759 \text{ m} \\ 1 \end{bmatrix},$$

with the appropriate transformation matrices based on the HBA geometry according to Equation 2.1.

We ignore HBA torso rotation in the HBA in our approach because we are only concerned with components below the waist. Thus, we can treat  $\phi_1$  as  $\phi_1=0$ . Similarly, we have not found  ${}^0T_1$ , but we can treat it as an identity matrix.<sup>11</sup> As already mentioned, the point falls on the  $z_4$ -axis, so the last rotation  $J(\phi_4)$  (about  $z_4$ ) can also be discounted. With these simplifications, the expression for the tip point can be simplified to

$${}^0\vec{v}_{\text{tip}} = {}^1T_2 J(\phi_2) {}^2T_3 J(\phi_3) {}^3T_4 \begin{bmatrix} 0 \\ 0 \\ -0.3759 \text{ m} \\ 1 \end{bmatrix}.$$

The base point (which, for this application, we will treat as independent of the HCJA pose) is defined as a constant position in the Proximal Section frame (frame 2) and located at  ${}^2\vec{v}_{\text{base}} = \begin{bmatrix} 0 & 0 & h_{1/2} & 1 \end{bmatrix}^T$ , where  $h_{1/2}$  is one of the parameters from

---

<sup>11</sup>We are focused on the hip joint and the limb distal to it, so the components proximal to it can be simplified. In the code for this approach, and the later ROM tests, this transformation was not an identity matrix, but was described as having  $\theta_0 = a_0 = \alpha_0 = 0$  and  $d_0 = -6$  inches. This additional translation of 6 inches was purely for visualization purposes, so a stand-in for the HUT could be clear in the visual representations.

Chapter 2 used to describe the HBA. This point is the centroid of the top edge of the Proximal Section, the bottom edge of the Briefs, and the bearing between them. The base point was tied to the HCJA geometry for convenience, but it means this approach will evaluate the best-case possibility for ROM [5]. In the global frame, the base point is at

$${}^0\vec{v}_{\text{base}} = {}^0T_1 J(\phi_1) {}^1T_2 J(\phi_2) \begin{bmatrix} 0 \\ 0 \\ h_{1/2} \\ 1 \end{bmatrix},$$

with the appropriate transformation matrices based on the HBA geometry,<sup>12</sup> according to Equation 2.1. We can again treat  $\phi_1$  as equal to 0 and  ${}^0T_1$  as an identity matrix, so the expression simplifies to

$${}^0\vec{v}_{\text{base}} = {}^1T_2 \begin{bmatrix} 0 \\ 0 \\ h_{1/2} \\ 1 \end{bmatrix}.$$

It is clear from this result that the hip point does not change with kinematic rotation (no  $\phi$  values in the equation), as desired.

The other component of the simulated thigh that we must create is the set of line segments used to describe the shape of the thigh. For simplicity, it is approximated

---

<sup>12</sup>The base and tip points used in this example (and in the tradespace analysis in Chapter 5) create a simple and logical approximation of the thigh, but suffer from a particular problem. By setting the base and tip points as constants within the separate frames, the distance between the points will change between different HCJA positions, so the simulated thigh grows and shrinks as the HCJA moves. For simplicity and computational efficiency, this was allowed.

using eight line segments forming a truncated cone. The 2012 Anthropometric Survey of U.S. Army Personnel (ANSUR II) was used to specify the circumference at each end of this shape: the hip and knee circumferences (see Table 3.2) [11]. For this analysis, the fiftieth percentile male values were selected. As noted in Table 3.2, certain leg dimensions did not come directly from ANSUR II, but instead were calculated from raw ANSUR II values. The hip and knee radii were estimated using the equivalent circumferences from ANSUR II, divided by  $2\pi$ . Additionally, to account for tissue compression and motion within the suit, these values were scaled by 0.7 and 0.85, respectively, in the simulated leg.<sup>13</sup>

<b>Dimension</b>	<b>Value (cm)</b>	<b>ANSUR #/Title or Equation</b>
Hip Circumference	62.40	#78/Thigh Circumference
Knee Circumference	40.80	#60/Lower Thigh Circumference
Thigh Radius	6.95	$\left(\frac{0.7}{2\pi}\right) * (\text{Hip Circumference})$
Knee Radius	5.52	$\left(\frac{0.85}{2\pi}\right) * (\text{Knee Circumference})$

Table 3.2: Table showing dimensions of simulated thigh used in HBA range of motion analysis. The Circumference dimensions are from ANSUR II [11]. The Radius dimensions are calculated based off their respective circumferences, using the equations in the table.

The radii in Table 3.2 are used to form circles centered on the hip and knee points, respectively, with the cone’s axis running between. The circles lie on planes normal to this axis. The line segments intersect the planes at points equally spaced around the circles. The line segments of the simulated thigh can be seen in Figure 3-3.

---

<sup>13</sup>The knee end was reduced by less than the hip end for several reasons. There is more bone and less muscle around the knee, so tissue compression should be less. Additionally, the knee may be more constrained and less free to move within the suit, due to the smaller suit diameter there.

### 3.2.2 Suited Range of Motion Estimation

The Suited ROM is estimated by considering the space of possible HCJA poses, simulating the limb inside the HCJA, and noting the positions where the limb and HCJA do not intersect. The set of possible poses (with the possibility of repetition) is the set of  $N_{DoF}$  real numbers on the range  $[0, 2\pi)$ , where  $N_{DoF}$  is the number of DoFs or bearings in the HCJA. Each number indicates the angular displacement of a DoF. Thus, the space of possible poses forms an  $N_{DoF}$ -dimensional hypercube. The space of HCJA poses can be reduced when estimating the Suited ROM by limiting the angles considered for each DoF, based on the feasibility of possible motions of the suit's occupant and the relevance to the topic at hand.<sup>14</sup> This changes the space of possible poses from a hypercube to a set of  $N_{DoF}$  angular ranges.<sup>15</sup> For each joint  $n$  (see Section 2.2 for an explanation of the indexing), there will be an upper and lower bound on the angles considered, denoted  $\phi_{n,\min}$  and  $\phi_{n,\max}$ .<sup>16</sup> To estimate the Suited ROM, the set of possible poses is sampled over its entire (finite) volume. The sampled angles for joint  $n$ , are found by sampling its bearing ranges with an increment specified by  $\Delta\phi_n$ , between bounds  $\phi_{n,\min}$  and  $\phi_{n,\max}$ . This sampling generates  $N_{DoF}$  sets of angles. The poses created from these sets, used to estimate the Suited ROM, correspond to the possible ways to choose one angle from each of these sets, so the total number of poses is the product of the cardinality of these sets.

For a given pose, the relevant limb is simulated (see Section 3.2.1) within the

---

<sup>14</sup>If the Suited ROM is being calculated to define the ROM score as described in Section 3.3, then bearing positions which would prohibit the relevant limb (estimated in Section 3.2.1) from being inside or near the Unsited ROM can be discounted for efficiency. The ROM score is based on the overlap between the Suited and Unsited ROM, so points which will not contribute to the overlap can be ignored. If the shape of the ROM (and not just the score) is a desired value, this should not be done.

<sup>15</sup>This new set of pose possibilities is a subset of the hypercube.

<sup>16</sup>These are measured from the joint's neutral position,  $\eta_n$ . See Chapter 2.



HCJA. The simulated limb and the surfaces of the HCJA (sourced from a .STL file or the model in Chapter 2) are tested for intersection. If the limb is simulated with a set of lines, as recommended in Section 3.2.1, and the HCJA surfaces are composed of triangles (like a .STL file or the surfaces in Section 2.4), this can be achieved with a triangle/ray intersection algorithm.<sup>17</sup> If there is no intersection, the orientation of the simulated limb is considered to be within the Suited ROM and the vector corresponding to the limb’s orientation (expressed in the global frame),  ${}^0\vec{v}_{\text{tip}} - {}^0\vec{v}_{\text{base}}$  (see Section 3.2.1), is recorded. This process is repeated for each HCJA pose sampled from the space of possible poses.<sup>18</sup>

The non-intersecting limb position vectors recorded across the space of possible poses are normalized to unity, then used to generate the Suited ROM. The ROM comparison method described in Section 3.3 uses the vectors in this form, with no further modification required, as input. To find the Suited ROM for other purposes, the points on the unit sphere surface corresponding to the vectors can be used to generate a shape,<sup>19</sup> or the vectors themselves can be used to estimate the solid angle of the ROM.

### 3.3 Comparison of Unsuiting and Suited Ranges of Motion

To accurately assess the impact of an HCJA on the occupant’s MDoF ROM, the Unsuiting ROM (described in Section 3.1) and the Suited ROM (found in Section 3.2)

---

<sup>17</sup>For this research, a version from MATLAB Central File Exchange was downloaded and modified for speed and efficiency [35].

<sup>18</sup>One possible implementation is  $N_{\text{DoF}}$  nested loops, iterating over each sampled bearing angle, one dimension at a time.

<sup>19</sup>One method is to follow steps one through four in Section 3.3, ignoring the Unsuiting ROM.

can be compared. The Unsuitied ROM should be in the form of a set of unit vectors that define a shape on the surface of the unit sphere, where the shape is the limits of the relevant ROM when unencumbered. The Suited ROM is also a collection of unit vectors, which correspond to positions of wearing the HCJA.<sup>20</sup> These ROMs can be compared by converting the scattered points of the Suited ROM into a bounded shape, and comparing this shape to the Unsuitied ROM. A quantifiable metric termed the “ROM score” is defined. The ROM score is proportional to the amount of the Unsuitied ROM shape that overlaps with the Suited ROM shape (at maximum, identical to the Unsuitied ROM if the Suited ROM entirely contains the Unsuitied ROM), and describes what portion of the Unsuitied ROM remains accessible when suited, and indicates to what extent the HCJA restricts the joint or task. This section will describe the process for calculating ROM score.

The ROM vectors cannot simply be converted to spherical coordinates and the area overlap found, due to problems stemming from spherical geometry. The most significant problem was the Unsuitied ROM (and, in many cases, the Suited ROM as well) containing the “south pole” ( $-\tilde{z}$ -axis) of the unit sphere, which is a singularity in spherical coordinates. Simply converting to spherical coordinates and plotting results resulted in shapes wrapping around the borders of the plot, making it impossible to calculate an accurate area representation, as shown in Figure 3-4. The simple shape on the surface of the sphere in Figure 3-4a becomes divided and complex in Figure 3-4b. For proper measurement, a different axis for the unit sphere must be chosen, such that the singularity does not fall within the overlap of the ROMs. As a sphere

---

<sup>20</sup>Technically, this is not an ROM but a sampling of points within it. As described in Section 3.2, the region that contains these points can be converted to an estimate of the Suited ROM by following steps one through four in this section. The points are converted to the ROM as this process proceeds. For simplicity, these set of points are still referred to as the Suited ROM in this section.

is uniform in all directions, changing the axis can also be thought of as rotating our points of interest on the surface of the sphere. The magnitude of this rotation depends on the data itself. Figure 3-4 also highlights another problem that requires correction: the distortion of area in spherical coordinates, based on proximity to the poles. The red circles in Figure 3-4a are the same size, but appear quite different when plotted in Figure 3-4b. Rotation cannot solve this issue, which applies over the entire sphere. Instead, a specific area-preserving projection is used when mapping the coordinates. The following procedure to calculate the ROM score avoids these issues. The steps of this process are illustrated in 3-6. We begin with the unit vectors of the Suited and Unsited ROMs, illustrated in Figure 3-6a.

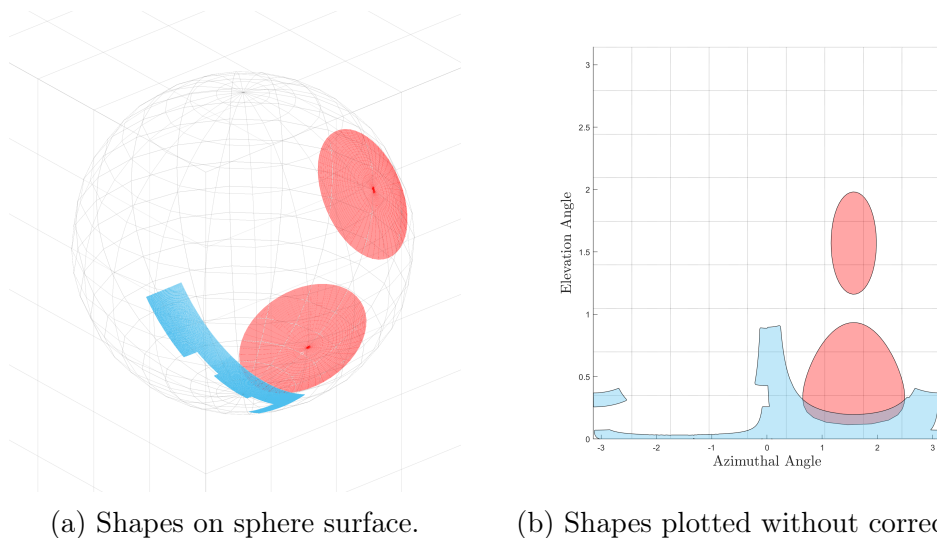


Figure 3-4: Example of problems with spherical geometry when axis rotation and the sinusoidal projection are not used. Note how the blue shape is warped and divided across the plot and how the red circles, which are the same size ( $1/3$  steradian) on the surface of the sphere, are wildly different in size in the projection.

1. **Rotate Suited and Unsited ROM Vectors:** To avoid geometric distortion shown in Figure 3-4, the Suited and Unsited ROM vectors must be rotated

away from spherical coordinate singularities (the “poles” or  $\pm\tilde{z}$ -axes). This rotation, by angle  $\rho$ , occurs around the  $\tilde{y}$ -axis in the negative direction.<sup>21</sup>

The amount of rotation to move the ROMs away from the singularities is bounded. The vectors must be rotated enough to move away from the  $-\tilde{z}$  singularity, but not rotated so much as to intersect the  $+\tilde{z}$  singularity. The following example uses the simple rectangular Unsuiting gait hip ROM from Section 3.1, but similar approaches can be used to find the rotation bounds for any Unsuiting ROM.

The Unsuiting hip gait ROM example from Section 3.1 spans angles from  $-\psi_{\text{flex}}$  to  $\psi_{\text{ext}}$  around the positive  $\tilde{y}$ -axis, so the rotation must be more than  $-\psi_{\text{ext}}$  and less than  $\pi + \psi_{\text{flex}}$ . Thus,

$$-\psi_{\text{ext}} < \rho < \pi + \psi_{\text{flex}}.$$

The calculation is more complex for the Suited ROM vectors, which do not have a simple shape. The rotation is around the  $\tilde{y}$ -axis, meaning the vectors that have any significant  $\tilde{y}$ -coordinate will not be distorted by the singularity for any rotation (no value of  $\rho$  will bring those points close to the poles). We focus on Suited ROM vectors with small  $\tilde{y}$ -coordinates, which we can, in this approach, conveniently define as vectors with a  $\tilde{y}$  component that satisfies<sup>22</sup>  $\sin \psi_{\text{ab}} \geq y \geq \sin \psi_{\text{ad}}$ . This subset of vectors covers a range defined by their  $\tilde{x}$ -coordinates,<sup>23</sup> which we can say have a minimum of  $x_{\text{min}}$  and a maximum of

---

<sup>21</sup>A vector pointing down from the hip would move like a thigh in flexion.

<sup>22</sup>If there are no such vectors, no rotation is needed. We do not need to do area-comparison, because we already know that there is no overlap between the ROMs, as there are no Suited ROM vectors with the appropriate  $\tilde{y}$ -coordinates, and thus no ROM overlap. The ROM score is 0.

<sup>23</sup>This assumes that none of them are in the upper hemisphere.

$x_{\max}$ . Given they are all of length unity, their angular range can be expressed as going from  $\arcsin x_{\min}$  to  $-\arcsin x_{\max}$ , so we know the rotation must be more than  $-\arcsin x_{\min}$ , but less than  $\pi - \arcsin x_{\max}$ , indicating that

$$-\arcsin x_{\min} < \rho < \pi - \arcsin x_{\max}.$$

The magnitude of the rotation  $\rho$  must fall within the rotational bounds established for both the Suited and Unsited vectors. To rotate both ROMs away from the  $-\tilde{z}$  singularity, we need to rotate by an angle that is greater than both  $-\psi_{\text{ext}}$  and  $-\arcsin x_{\min}$ , so our minimum rotation is the maximum of these values, or

$$\rho_{\min} = \max(-\arcsin(x_{\min}), -\psi_{\text{ext}}).$$

Similarly, to ensure that neither ROM interacts with the  $+\tilde{z}$  singularity, we cannot rotate by an angle that will bring either set of vectors to the “north pole”. Therefore, our angle of rotation must be less than both  $\pi + \psi_{\text{flex}}$  and  $\pi - \arcsin x_{\max}$ , so we can describe our maximum rotation as

$$\rho_{\max} = \min(\pi - \arcsin(x_{\max}), \pi + \psi_{\text{flex}}).$$

With the range of possible rotations established,<sup>24</sup> between  $\rho_{\max}$  and  $\rho_{\min}$ , a value between them must be selected to rotate the vectors. To provide a

---

<sup>24</sup>There is theoretically a possibility that  $\rho_{\min} \geq \rho_{\max}$ , meaning there is no possible rotation. This would also mean that the area of possible overlap (or actual overlap) being studied spans 180°, which is somewhat unlikely in a space suit (it may be possible, for example, in the shoulder joint). If it did occur, and defining the area of possible overlap more strictly did not resolve the problem, an additional rotation can be added. A single rotation around  $\tilde{y}$ -axis was chosen for simplicity. Really, any set of rotations that are consistently applied and move the  $\pm\tilde{z}$  singularities outside of overlap areas (or either ROM, preferably) will work.

consistent approach that is near the minimum rotation but sufficiently far from the borders, the rotation value is selected to be 20% of this range away from  $\rho_{\min}$ . In other words

$$\rho = \rho_{\min} + 0.2(\rho_{\max} - \rho_{\min}).$$

Every vector in the Suited or Unsited ROM, is rotated by  $\rho$  around the negative  $\tilde{y}$ -axis (or  $-\rho$  about the positive  $\tilde{y}$ -axis), using a standard rotation matrix. Every vector in either ROM is treated as  $\vec{v}_0$  and converted to  $\vec{v}$  by:

$$\vec{v} = \begin{bmatrix} \cos(-\rho) & 0 & \sin(-\rho) \\ 0 & 1 & 0 \\ -\sin(-\rho) & 0 & \cos(-\rho) \end{bmatrix} \vec{v}_0 = \begin{bmatrix} \cos \rho & 0 & -\sin \rho \\ 0 & 1 & 0 \\ \sin \rho & 0 & \cos \rho \end{bmatrix} \vec{v}_0.$$

The definition of this rotation range can be seen in Figure 3-5 and the rotated vectors can be seen in Figure 3-6b.

2. **Convert to Spherical Coordinates:** The now-rotated vectors of the Suited and Unsited ROM are converted to spherical coordinates. There are at least two conventions for spherical coordinates, where  $r$  or  $\rho$  is the vector length and  $\phi$  and  $\theta$  are either the inclination or azimuth angles. As  $\theta$  and  $\phi$  are already used in this text, we will use a convention where  $\lambda$  is inclination (measured from the  $xy$ -plane),  $\xi$  is azimuth, and  $r$  is length. (All vectors under consideration are normalized, so length  $r$  is ignored.) For a given unit vector  $\hat{v} = \begin{bmatrix} x & y & z \end{bmatrix}^T$ , conversion follows according to:

$$r = \sqrt{x^2 + y^2 + z^2} \quad \lambda = \arccos \frac{z}{r} = \arccos z \quad \xi = \text{atan2}(y, x).$$

To ensure there is no issue with the discontinuity from  $\text{atan2}$ , the range of  $\xi$

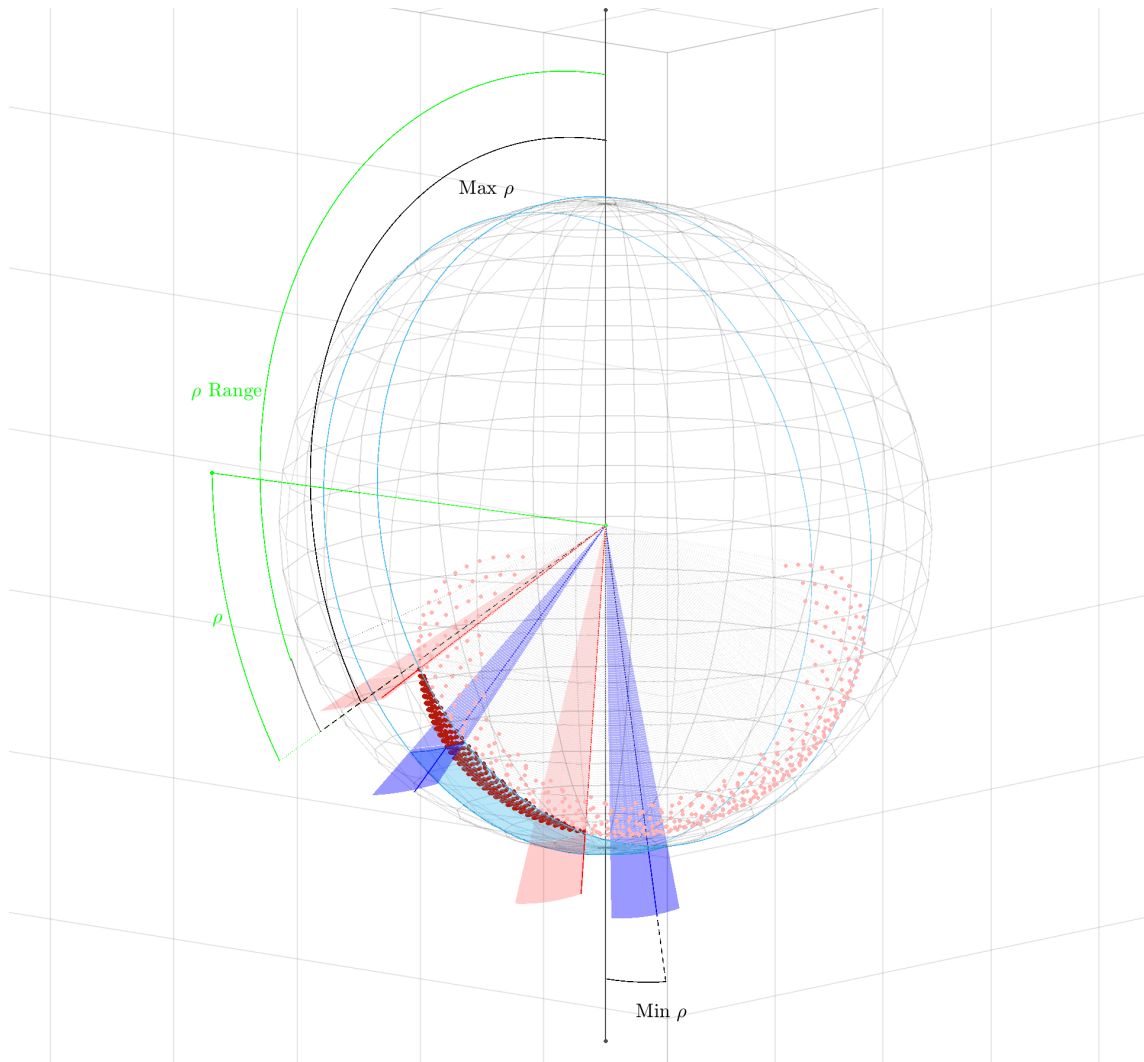


Figure 3-5: Illustration of the minimum and maximum rotations possible to move the vectors away from the singularities. Also shown is the rotation range and selected rotation,  $\rho$ . The pink dots represent the points identified to be within the Suited ROM, and the blue box is the Unsuited ROM. The red dots indicate the points in the Suited ROM that are considered relevant to rotation, and the red lines indicate the maximum/minimum points in that group (those that limit the overall rotation the most). The blue lines represent the maximum/minimum points for the Unsuited ROM, and the black dotted lines represent the overall maximum/minimum points from both ROMs. The maximum and minimum values of  $\rho$  are found from there.

can be adjusted based on the positions of the ROMs. For example, it could be adjusted to go from  $-\frac{\pi}{2}$  to  $\frac{3\pi}{2}$  by incrementing all values of  $\xi \leq -\frac{\pi}{2}$  by  $2\pi$ .

With the length constant, the vectors are now expressed as points in two dimensions, as shown in Figure 3-6c.

3. **Sinusoidal Projection:** With the conversion to spherical coordinates, the regions on the sphere are projected to a two-dimensional map to estimate the overlapping area. There are several projections that can be used (exactly like there are many map projections), with some variants causing distortions that we want to eliminate, like those seen in Figure 3-4 [30][32]. The approach used here to avoid distortion is similar to the sinusoidal projection [30]. We scale the  $\xi$  component (offset from an arbitrary middle point) by the sine of the  $\lambda$  component. The middle point selected is the mean of all  $\xi$  values<sup>25</sup> for all vectors in the Suited ROM,  $\mu_{\xi,\text{suited}}$ . All vectors retain the same relative position to each other, but move towards  $\mu_{\xi,\text{suited}}$  near the “poles” of the spherical coordinate system. In other words, for every vector  $u = (\xi, \lambda)$ , there is a transformation to  $u' = (\xi', \lambda)$  by the rule

$$\xi' = (\xi - \mu_{\xi,\text{suited}}) \sin \lambda + \mu_{\xi,\text{suited}}.$$

A shape formed by parts which have undergone this transformation will have a Cartesian area proportional to the area of the original shape on the unit

---

<sup>25</sup>Note that while the mean is of just the vectors in the Suited ROM, this transformation is applied to all vectors, including the boundary vectors of the Unsited ROM. This value was chosen as it produced good visualizations.



sphere surface.<sup>26</sup> With this transformation, the Cartesian area of any shape formed by the point of the form  $(\xi', \lambda)$  will now be proportional to the area of a shape on the surface of a sphere, traced out in the same manner. See proof in Appendix B. The effect of this projection can be seen in Figure 3-6d.

4. **Define Polyshapes for ROMs:** With ROM vectors rotated, transformed, and projected, the actual comparison can proceed. If there are 10 or fewer<sup>27</sup> valid points in the Suited ROM, the code returns to an area overlap of zero. Otherwise, it continues as described here.

Shapes were created using MATLAB's `polyshape` functionality. However, certain HCJA geometries produce unconnected areas of points within the ROM. These areas are in the Suited ROM, but areas between them may not be. To prevent the creation of inaccurate "bridge" areas between these areas, a cluster analysis was performed on the set of  $(\xi', \lambda)$ -encoded Suited ROM points, using MATLAB's `evalclusters` function. A  $k$ -means clustering algorithm is used, using the silhouette clustering evaluation criterion. Clustering is attempted for a cluster number from 1 to 5, and the optimal number is found by the function, using the criteria established by MATLAB [18]. The use of clustering also seems to improve matching the concave surfaces of shapes.<sup>28</sup>

For each of the clusters identified (shown in Figure 3-6e, the points in the

---

<sup>26</sup>For shapes with few vertices, this depends somewhat on the manner in which the lines between the points are transferred to the sphere. When there are few vertices and each side is comparatively long there is a difference between transforming the sphere surface points corresponding to each vertex with simple connecting lines and transforming each point along the great-circle edges of the sphere. However, for complex shapes or shapes with many vertices (as we have here), where each line between vertices is short, this question quickly diminishes.

<sup>27</sup>The use of 10 points as the boundary was selected by trial-and-error.

<sup>28</sup>This seems to stem from the clustering algorithm dividing a strongly concave shape into two or more sub-shapes that are less concave.

cluster are considered and an attempt is made to form a sub-shape. First, the boundary points of the cluster are found using the `boundary` function in MATLAB. The “shrink factor” of this function, which governs how tightly the boundary hugs the data, is set to 0.8 in all cases, for consistency. This value was found by trial-and-error to produce a tight-fitting edge that still represented the general shape of the region, not affected by gaps between points. If the `boundary` command returns a list of three<sup>29</sup> or more points, a shape is created from these points using MATLAB’s `polyshape` function, which returns a `polyshape` object. To ensure good meshing with other sub-shapes (as the clustering algorithm does sometimes divide one large, cohesive group into smaller groups), the shape is then grown or “buffered,” creating a rim around the shape. This is achieved with the `polybuffer` function, and the distance of buffering is set to the square root<sup>30</sup> of the area of the shape (calculated using the `area` function of the `polyshape` object), scaled by 0.02. This ratio was determined by trial-and-error. The shape is then simplified using the `simplify` function for `polyshape` objects, which removes duplicate vertices or edges which cross one another.

The process is applied to each cluster. Using the `union` function, the resulting shapes from each cluster are combined. If all clusters are tested, and no clusters have produced valid boundaries and shapes, all sub-shapes are non-valid and the ROM score is 0.

A `polyshape` object is also calculated from the transformed vectors of the Unsuited ROM. The generated polyshapes can be seen in Figure 3-6e.

---

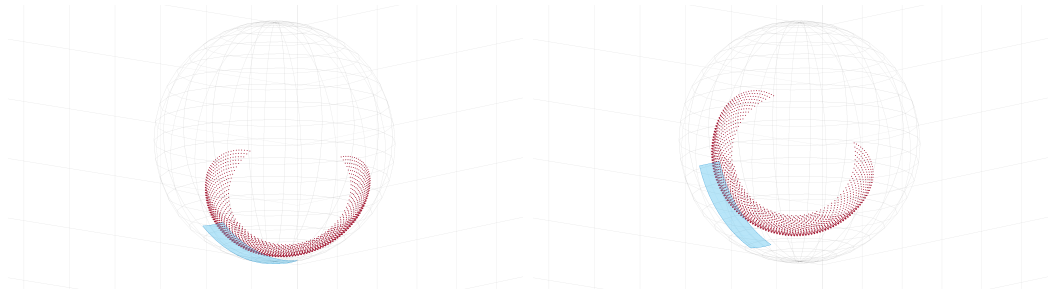
<sup>29</sup>If a sub-shape has only 2 or fewer boundary points, it is either a line or not a valid shape and so it is discarded.

<sup>30</sup>On occasion, for reasons unknown, MATLAB returns a negative or imaginary area for a shape that is clearly valid. Due to issues calculating this area, this buffering is only applied if the area returned is real and positive.

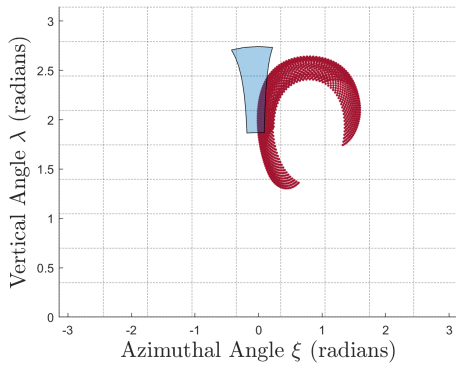
5. **Calculate Overlap Area:** The overlap between the polyshape objects representing the Suited and Unsited ROMs is found using MATLAB's `intersect` function for polyshape objects. This returns a new polyshape object that is the intersection, or overlap, of the two ROMs, as shown in Figure 3-6f. The area of this overlap polyshape is found using the `area` function. This area indicates the Suited and Unsited ROMs overlap. Thus, the overlap area, scaled<sup>31</sup> by  $\frac{1}{4\pi}$ , is the ROM score.

---

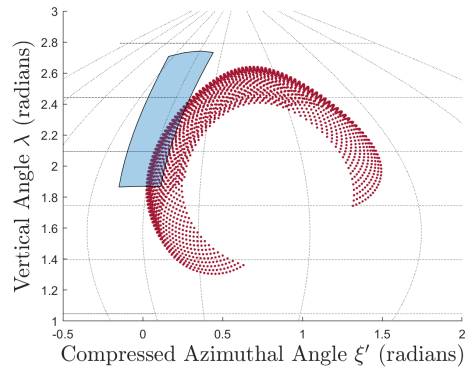
<sup>31</sup>The area is unitless, as it is on the surface of the unit sphere and composed by unitless vectors, so normalization is not needed. However, the area is scaled by  $\frac{1}{4\pi}$ , the surface area of a unit sphere, to better define the area covered.



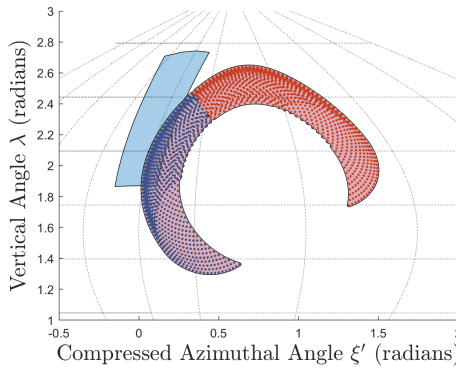
(a) Unsuited ROM points (b) Suited ROM points. Rotated on surface of unit sphere.



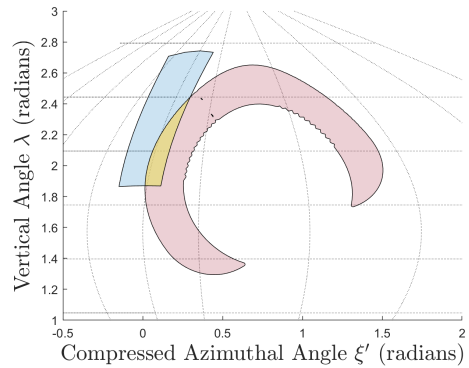
(c) Converted to spherical coordinates.



(d) Sinusoidal projection.



(e) Polyshapes generated. Suited ROM points colored by cluster.



(f) Unsuited and Suited ROM Overlap.

Figure 3-6: Steps to calculate ROM score.

## Chapter 4

# Hip Bearing Assembly Design Constraints

With the geometric model discussed in Chapter 2, the design of an HCJA can be created from an arbitrary set of the parameters defined in Section 2.2. However, when the set of parameters is arbitrary, the geometry generated can be such that the hard-component joint assembly (HCJA) would be impossible to wear or use. To understand the connection between parameters and these situations, a method of detecting impossible or useless HCJA geometries from the parameters was desired. However, the definition of useless or impossible is highly dependent on the HCJA, the corresponding occupant's joint, and its purpose. Universal constraints were deemed impractical. Instead, the question was applied to a specific example: the Mark III Hip Briefs Assembly (HBA).

The Briefs was treated as symmetric across the sagittal plane, so any point in the Briefs frame on the right half,  ${}^1\vec{v}_R$ , can be converted from the equivalent left-half

vector,  ${}^1\vec{v}_L$ , by changing the sign on the  $y_1$ -coordinate,<sup>1</sup> as seen in Equation 2.10. This simplifies the physical structure of the Briefs. Only one bottom edge radius,  $r_{1b}$  is required, and the bottom edge on the left side is simply reflected across the sagittal plane to find the right side. The  $\tau_n(p)$  and  $\beta_n(p)$  index adjustments for the component edges, described in Equations 2.7 and 2.8, are used as well.

A set of constraints was created to detect infeasible HBA geometries (Section 4.1). These are converted to parameter form in Appendix E. Additionally, to explore the possibility space of HBA geometries, parameter bounds were considered. Certain parameters were defined as constants, while others were given upper and lower bounds, as detailed in Section 4.2.

## 4.1 Geometric Constraints

The HCJA geometry model outlined in Chapter 2 permits a set of arbitrary parameters, but these parameters often fail to produce a viable geometry, instead resulting in geometries that could not be worn or even constructed. Tests were created to detect these conditions specifically in the Mark III HBA.<sup>2</sup> The tests are applied to each component of the HBA separately, with the constraints for the Briefs laid out in Section 4.1.1 and those for the Proximal and Distal Sections detailed in Section 4.1.2.

---

<sup>1</sup>This term of  $y_1$ -coordinate of a specific vector, means the  $y$ -component of that vector, when that vector is expressed in frame in 1. The subscript means that it is measured along the  $y_1$  axis, no matter in what frame the vector is expressed. In other words, the  $y_n$  component for  $\vec{v}$  is equal to  ${}^n\vec{v} \cdot [0 \ 1 \ 0 \ 0]^T$ . This also can be applied to  $x$  and  $z$  axes.

<sup>2</sup>As mentioned in the introduction to this chapter, these constraints are highly dependent on the specific HCJA under consideration. These constraints are only for the Mark III HBA, but some of them could be generalized. The constraints on the Proximal and Distal Sections in Section 4.1.2, in particular, could be extended for all or most standard HCJA components.

### 4.1.1 Geometric Constraints for Briefs

The geometric constraints for the Briefs are listed below, with examples of geometries that violate each test shown in Figure 4-5.

- **Leg Direction:** The human leg generally points downwards, forward, outward, or some combination of the three. This is also the range of the hip most used for movements. There is a greater range of motion (ROM) at the hip for flexion than for extension, and for abduction than adduction [26].<sup>3</sup>

Due to these natural limits, a constraint on the “direction” of the bottom holes in the Briefs was created. The vector normal to the upper bearing, or “leg vector” pointing out of the bottom holes of the Briefs, must not be pointing backwards, upwards, or inwards. A visualization can be seen in Figure 4-1. This constraint is met in the nominal HBA.

The leg vector can be defined as the negative  $z$ -axis of the Proximal Section coordinate frame<sup>4</sup> (frame 2),  ${}^{-2}z_2 = [0 \ 0 \ -1 \ 0]^T$ , so the mathematical constraint can be stated:

$$\left( {}^1T_2 \begin{bmatrix} 0 \\ 0 \\ -1 \\ 0 \end{bmatrix} \right) \cdot \begin{bmatrix} 1 \\ 0 \\ 0 \\ 0 \end{bmatrix} \geq 0, \quad \left( {}^1T_2 \begin{bmatrix} 0 \\ 0 \\ -1 \\ 0 \end{bmatrix} \right) \cdot \begin{bmatrix} 0 \\ 1 \\ 0 \\ 0 \end{bmatrix} \geq 0, \quad \left( {}^1T_2 \begin{bmatrix} 0 \\ 0 \\ -1 \\ 0 \end{bmatrix} \right) \cdot \begin{bmatrix} 0 \\ 0 \\ 1 \\ 0 \end{bmatrix} \leq 0,$$

where  $\cdot$  is the dot product. Examples of Briefs which fail this constraint can be seen in Figures 4-5a, 4-5b, and 4-5c.

---

<sup>3</sup>The definition of these terms can be found in Appendix A.

<sup>4</sup>The circle forming the bottom edge of the Briefs lies in a plane normal to this vector. See Section 2.3.

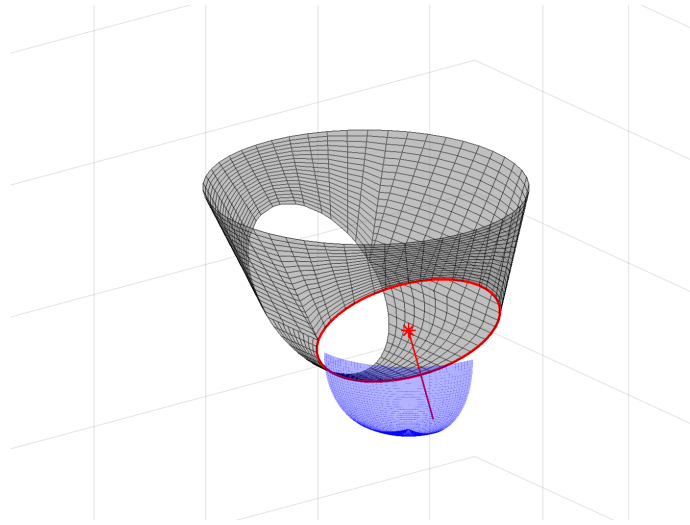


Figure 4-1: The surface for the nominal HBA Briefs, along with the limits imposed by the Leg Direction geometric constraint. The “leg vector” shown as the red line begins in the centroid (red star) of the bottom edge of the Briefs (also highlighted in red). This vector is normal to the plane containing the edge. To pass this constraint, the vector must point somewhere within the blue surface, which forms an octant of a sphere.

- Briefs Height:** The HBA should minimally constrain the occupant. With the top edge of the Briefs at a fixed position on the body, the bottom edge should not be too far from it. In other words, the Briefs should not be too “tall.” If the HBA were donned by a shorter occupant, Briefs that are too tall would place the bottom edges of the Briefs around the thighs. The lower the edges fall along the thigh, the more hip motion would be limited. Therefore, the Briefs are constrained to have a maximum height of  $z_{1,\max}$ , measured from the plane containing the top edge (the  $xy$  plane in frame 1). All points of the bottom edge of the Briefs must be a distance less than or equal to  $z_{1,\max}$  from that plane. The value of  $z_{1,\max}$  could be altered in other implementations of this model, dependent on the model’s purpose, but  $z_{1,\max} = 0.3$  m was used



here. This value was selected to avoid over-limiting the HBA geometry model. There is also a minimum distance between the top and bottom edges. While not represented in the model in Chapter 2, the physical HBA will have a non-zero thickness as well as supporting structures and mounting for the bearing hardware at the joints. There must be space in the design for those additions, so a constraint of  $z_{1,\min}$  is imposed. All points on the bottom edge must be at least  $z_{1,\min}$  away from the plane containing the top edge (the  $xy$  plane in frame 1). Similar to  $z_{1,\max}$ , this value could be altered in other implementations of this model, but  $z_{1,\min} = 0.03$  m was used here. This value was based on the Briefs of the nominal HBA, where the minimum gap between any two edges is a distance of 3.04 cm between the left and right bottom edges.

Because the top edge is in the  $xy$  plane, we can state this constraint more simply: all points of the bottom edge of the Briefs (defined by  ${}^1\vec{b}_1(p)$  in the appropriate frame<sup>5</sup>) must have a  $z$ -coordinate (in frame 1) in the range of  $[-z_{1,\max}, -z_{1,\min}] = [-0.3 \text{ m}, -0.03 \text{ m}]$  from the origin and top edge of the Briefs. In the model of the nominal HBA, the  $z_1$ -coordinate of the bottom edge runs from -0.2898 m to -0.0786 m, meeting this constraint. A visualization can be seen in Figure 4-2.

Using Equation 2.6 we can define this constraint as:

$$\forall p \in [0, 2\pi), -z_{1,\max} \leq \left( {}^1\vec{b}_1(p) \cdot \begin{bmatrix} 0 \\ 0 \\ 1 \\ 0 \end{bmatrix} \right) \leq -z_{1,\min}.$$

---

<sup>5</sup>Note that the  $\beta_1(p)$  conversion formula in Equation 2.8 is not used. This formula must apply for all points, so specifying the angular offset is unnecessary and makes the constraint more complicated.

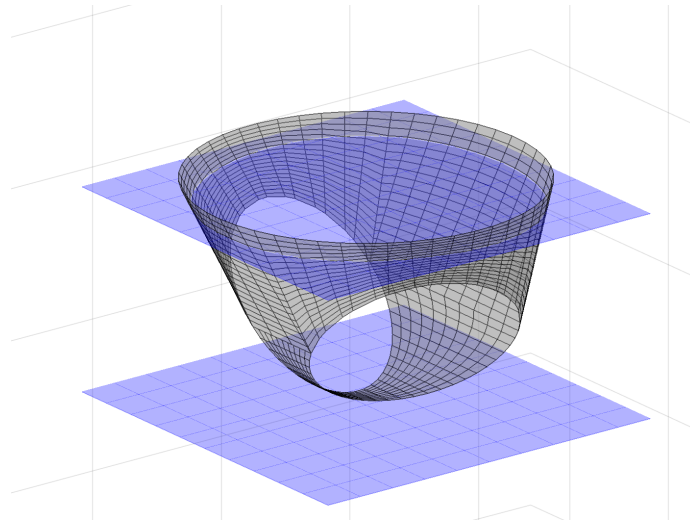


Figure 4-2: The surface for the nominal HBA Briefs, with the limits imposed by the Briefs Height geometric constraint. All points on the bottom edge must fall between the blue planes.

Examples of Briefs which fail this constraint can be seen in Figures 4-5d and 4-5e.

- Leg Gap:** The necessity of a minimum distance between locations of bearings, the motivation for the lower bound of the Briefs Height, also applies to the gap between the two bottom edges of the Briefs. The leg holes must have sufficient distance, a minimum of  $y_{1,\min}$ , between them to support the bearings. As in previous constraints, this value could be altered in other implementations of this model, but here the same value as for the Briefs Height lower bound was used:  $y_{1,\min} = 0.03$  m. As the Briefs are symmetric, this constraint can be enforced by considering the minimum distance between the bottom edge and the sagittal plane.

Thus, all points of the bottom edge of the Briefs must have a  $y$ -coordinate greater than or equal to  $\frac{y_{1,\min}}{2} = \frac{0.03 \text{ m}}{2} = 0.015$  m, to ensure that there is a gap

of 3 cm between the left and right leg holes. In the model of the nominal HBA, the bottom edge of the Briefs has a minimum  $y$ -coordinate of 0.0152 m.

A visualization can be seen in Figure 4-3.

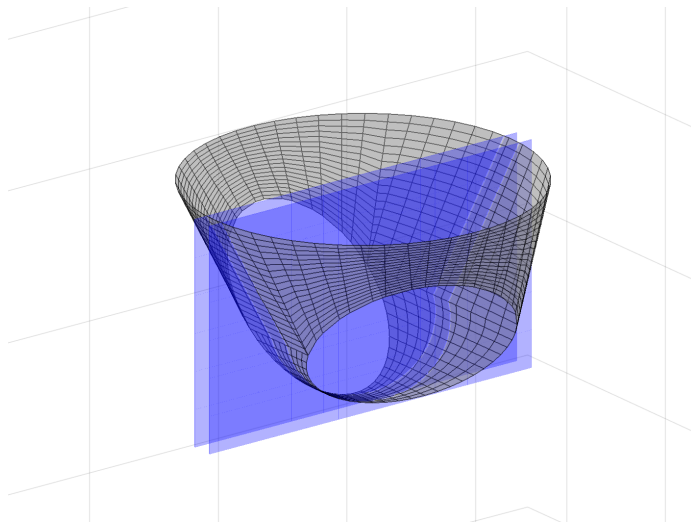


Figure 4-3: The surface for the nominal HBA Briefs, with the limits imposed by the Leg Gap geometric constraint. The bottom edges must not intersect the blue planes.

Using Equation 2.6 we can define this constraint as:

$$\forall p \in [0, 2\pi), \left( {}^1\vec{b}_1(p) \cdot \begin{bmatrix} 0 \\ 1 \\ 0 \\ 0 \end{bmatrix} \right) \geq \frac{y_{1,\min}}{2}.$$

An example of Briefs which fails this constraint can be seen in Figure 4-5f.

- **Leg Holes inside Briefs:** This constraint is related to the Briefs Height upper bound and prevents the Briefs from being too “wide,” with the leg holes falling too far from the waist hole in the  $xy$  plane. To enforce this constraint, all

points of the bottom edges must fall within the cylinder formed by the  $z$ -axis and the top edge of the brief. This requirement is met in the nominal HBA.

A visualization can be seen in Figure 4-4.

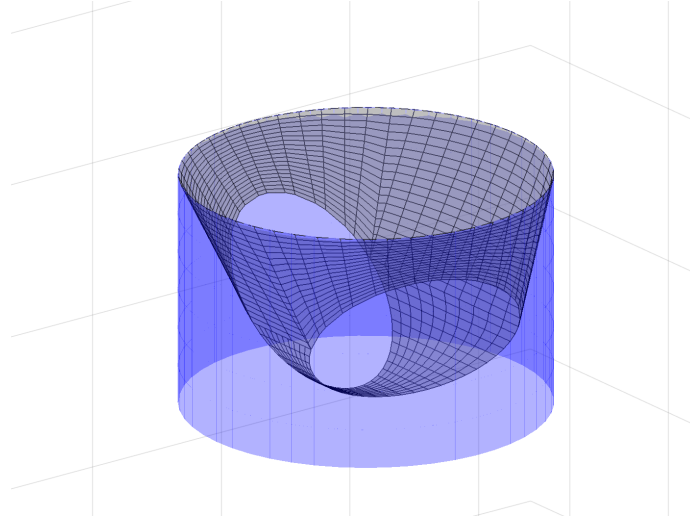


Figure 4-4: The surface for the nominal HBA Briefs, with the limits imposed by the Leg Holes inside Briefs geometric constraint. All points on the bottom edges must fall within the blue cylinder.

The expression for this constraint is based off the cross product identity

$$\vec{a} \times \vec{b} = \hat{n} \|\vec{a}\| \|\vec{b}\| \sin \phi, \quad (4.1)$$

where  $\hat{n}$  is the unit vector normal to both  $\vec{a}$  and  $\vec{b}$ ,  $\phi$  is the angle between the vectors, and  $\|\cdot\|$  is the Euclidean norm. This definition can be converted to  $\|\vec{a} \times \vec{b}\| = \|\vec{a}\| \|\vec{b}\| \sin \phi$ , which would be the length of the projection of  $\vec{b}$  onto the plane normal to  $\hat{a}$ . Using this identity, we can find the distance in the  $xy$  of a

point from the frame's origin by finding its projection into that plane as

$$\|\vec{a} \times \vec{b}\| = \|\hat{z}\| \|\vec{b}\| \sin \phi = \|\vec{b}\| \sin \phi,$$

where  $\hat{z}$  is the unit vector parallel to the  $z$ -axis for the relevant frame. We can apply this to Equation 2.6 and limit the distance to less than the top edge radius, giving the constraint

$$\forall p \in [0, 2\pi), \left\| \left( {}^1\vec{b}_1(p) \right)_{1:3} \times \begin{bmatrix} 0 \\ 0 \\ 1 \end{bmatrix} \right\| \leq r_{1t}.$$

An example of Briefs which fails this constraint can be seen in Figure 4-5g.

## 4.1.2 Geometric Constraints for Proximal and Distal Sections

The Proximal and Distal Sections are functionally and geometrically similar to one another. Therefore, the same constraints were used for both. As they are both oblique frusta, like the example in Figure 2-1, they are often limited based on features of frusta. The geometric constraints for these components are as follows, with examples of geometries that violate each test shown in Figure 4-6.

- **Frusta Length:** Similar to the Briefs Height limits in Section 4.1.1, there are limits on the length of these components, to avoid lengthy components limiting movement. This is determined by the distance between the centers of the top and bottom edges, which must be less than or equal to some bound, denoted  $l_{\max}$ . Like in previous constraints, this value could be altered in other

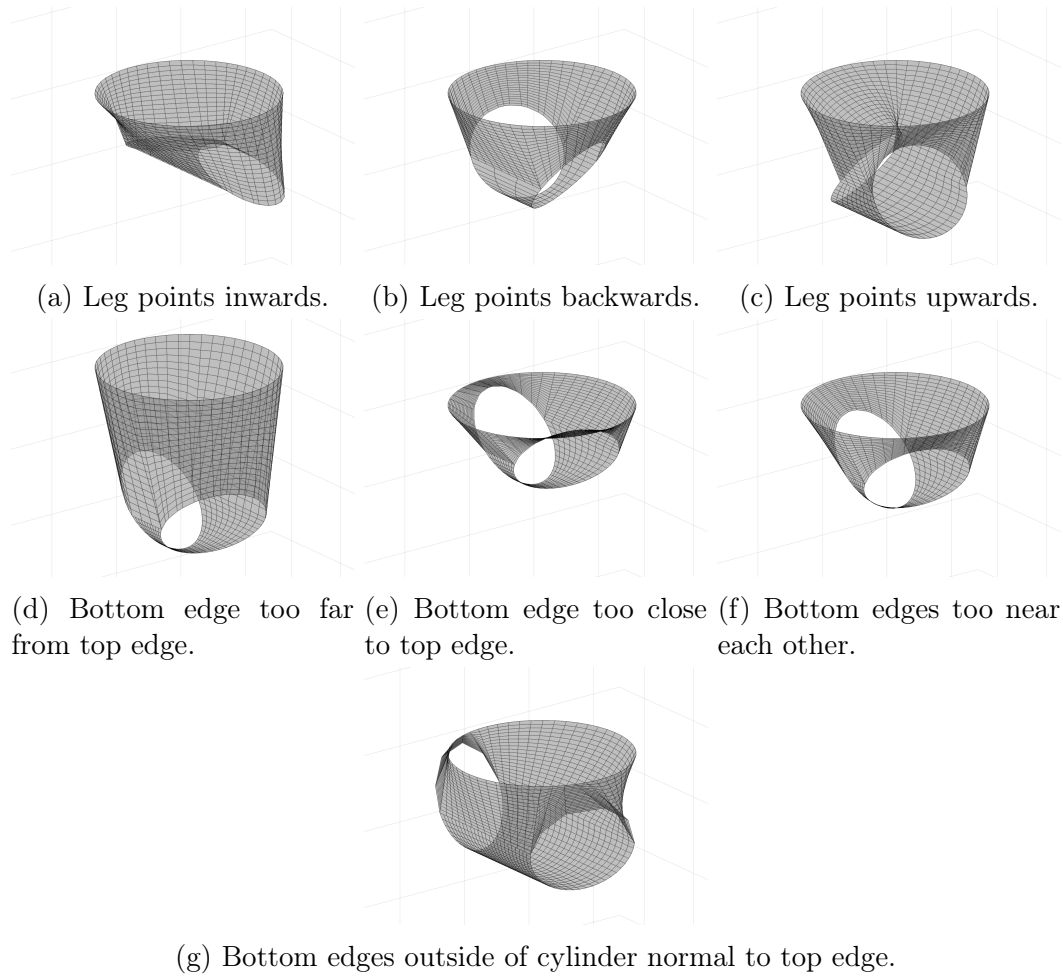


Figure 4-5: Examples of Briefs failing geometric constraints listed in Section 4.1.1.

implementations of this model, but  $l_{\max} = 0.15$  m was used here. In the model of the nominal HBA, the distance between the edge centers are 6.47 cm and 10.31 cm for the Proximal and Distal Sections, respectively, so they meet this constraint.

From Equations 2.3 and 2.5, we know the centers of the top and bottom edges and can define this constraint as

$$\forall n \in \{2, 3\}, \left\| \left\| \begin{bmatrix} 0 \\ 0 \\ h_{n-1/n} \\ 1 \end{bmatrix} - {}^nT_{n+1} \begin{bmatrix} 0 \\ 0 \\ h_{n/n+1} \\ 1 \end{bmatrix} \right\| \right\| \leq l_{\max}.$$

An example of a component which fails this constraint can be seen in Figure 4-6a.

- **Frusta Angle:** If either the Proximal or Distal Section had too sharp of an angle between the top and bottom edge planes, the occupant's thigh would not be able to pass through the component. The angle between these planes is therefore limited to be less than or equal to  $\gamma_{\max}$ . The value of this limit may change based on the model's implementation, but in this case the value was set to be  $\gamma_{\max} = 60$  degrees. For simplicity, this constraint is enforced by considering the cosine of the angle between the planes, which must be greater than or equal to  $\cos \gamma_{\max} = \cos(\frac{\pi}{3}) = \frac{1}{2}$ . In the model of the nominal HBA, the cosines of the angles between the edge planes are 0.9220 and 0.9196 for the Proximal and Distal Sections, respectively.

Mathematically, we can say find the angle between the edge planes by con-

sidering the angle between the vectors normal to each of them. From Equations 2.4 and 2.6, these are the  $z$ -axes  $z_n$  and  $z_{n+1}$ . Described in the same frame, we have,  ${}^n z_n$  and  $z_{n+1} = {}^n T_{n+1} {}^{n+1} z_{n+1}$ . We enforce this limit with the cosine definition of the dot product  $\vec{a} \cdot \vec{b} = \|\vec{a}\| \|\vec{b}\| \cos \phi$ , where  $\phi$  is the angle between the vectors. Applied to this case, we have

$$\forall n \in \{2, 3\}, \begin{bmatrix} 0 \\ 0 \\ 1 \\ 0 \end{bmatrix} \cdot \left( {}^n T_{n+1} \begin{bmatrix} 0 \\ 0 \\ 1 \\ 0 \end{bmatrix} \right) \geq \cos \gamma_{\max}$$

An example of a component which fails this constraint can be seen in Figure 4-6b.

- **Frusta Skew:** It is simple to create an oblique frustum where few straight lines can go through both ends. If either the Proximal or Distal Section took a shape like this, they would not fit around the occupant. This constraint is defined by projecting both the top and bottom edges into normal cylinders. The center of each edge must fall within the cylinder of the opposite edge. In other words, if the center of the one edge were projected onto the plane of the opposite edge, the projected point must fall within that opposite edge. This requirement is met in the nominal HBA for both the Proximal and Distal Sections.

Like the Leg Holes inside Briefs constraint in Section 4.1.1, this constraint is based off the cross product identity in Equation 4.1. Applied to Equa-



tions 2.3 and 2.5, we find

$$\forall n \in \{2, 3\}, \left\| \begin{bmatrix} 0 \\ 0 \\ 1 \end{bmatrix} \times \left( {}^n T_{n+1} \begin{bmatrix} 0 \\ 0 \\ h_{n/n+1} \\ 1 \end{bmatrix} \right) \right\|_{1:3} \leq r_{nt}$$

and

$$\forall n \in \{2, 3\}, \left\| \begin{bmatrix} 0 \\ 0 \\ 1 \end{bmatrix} \times \left( {}^{n+1} T_n \begin{bmatrix} 0 \\ 0 \\ h_{n-1/n} \\ 1 \end{bmatrix} \right) \right\|_{1:3} \leq r_{nb}.$$

An example of a component which fails this constraint can be seen in Figure 4-6c.

- **Frusta Height:** Like the previous two, this constraint helps to ensure that the occupant's leg will fit through the component. We require the bottom edge to not cross the plane in which the top edge lies, which is parallel to the  $xy$  plane of a given component's frame, offset by the joint's proximal  $h$ , all of the bottom edge must have a  $z_n$ -coordinate less than the top edge,  $h_{n-1/n}$ . This constraint is met for both Proximal and Distal Sections in the nominal HBA.

Considering Equations 2.6 and 2.4, we find

$$\forall n \in \{2, 3\}, \forall p \in [0, 2\pi), \left( \begin{bmatrix} 0 \\ 0 \\ 1 \\ 0 \end{bmatrix} \cdot {}^n \vec{b}_n(p) \right) \leq h_{n-1/n}.$$

An example of a component which fails this constraint can be seen in Figure 4-6d.

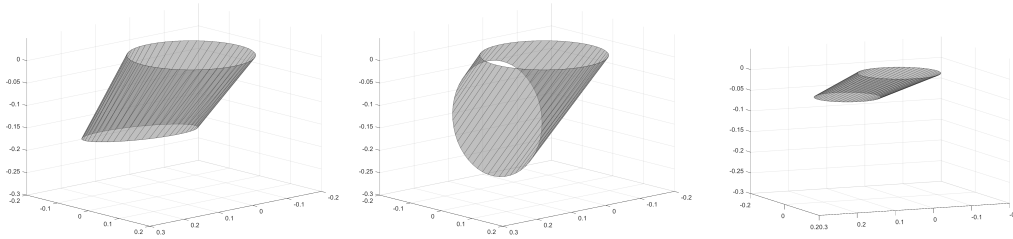
- **Frusta Edge Gaps:** Similar to the Briefs Height lower bound and the Leg Gap constraint in Section 4.1.1, this constraint ensures an acceptable distance between the edges of the component, to provide space for structure and the hardware of the bearings themselves. The top and bottom edges must be at least  $l_{\min}$  distance apart at their closest points. The value of this limit could be altered when the model is implemented elsewhere, but  $l_{\min} = 0.005$  m was used here. This value was chosen to serve as a small value that would not over-limit the design space while requiring some space for the bearing hardware. In the model of the nominal HBA, the closest the opposite edges come to each other are 0.88 cm and 4.84 cm for the Proximal and Distal Sections, respectively.

Based on Equations 2.4 and 2.6, we can describe the constraint as

$$\forall n \in \{2, 3\}, \forall p_t \in [0, 2\pi), \forall p_b \in [0, 2\pi), \left\| {}^n\vec{t}_n(p_t) - {}^n\vec{b}_n(p_b) \right\| \geq l_{\min}.$$

An example of a component which fails this constraint can be seen in Figure 4-6e.

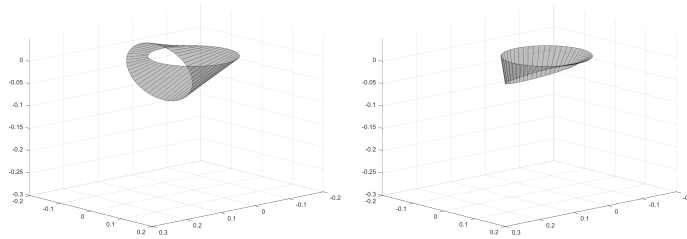
Using the previously-written formulae for transformations and edges, the constraints discussed in Sections 4.1.1 and 4.1.2 can be re-written in terms of our parameters. The simplifications of these equations can be found in Appendix E, and the results are given in Table 4.1.



(a) Frusta too long.

(b) Frusta too angled.

(c) Frusta too skewed.



(d) Bottom edge crosses the plane of the top edge.

(e) Edges too close.

Figure 4-6: Examples of oblique frusta failing geometric constraints for Proximal and Distal Sections listed in Section 4.1.2.

<b>Leg Direction</b>	$\left(\left(\frac{3\pi}{2} \leq \theta_1 \leq 2\pi\right) \wedge \left(0 \leq \alpha_1 \leq \frac{\pi}{2}\right)\right)$ <p style="text-align: center;">or</p> $\left(\left(\frac{\pi}{2} \leq \theta_1 \leq \pi\right) \wedge \left(\frac{3\pi}{2} \leq \alpha_1 \leq 2\pi\right)\right)$
<b>Briefs Height</b>	$r_{1b} \sin \alpha_1 + h_{1/2} \cos \alpha_1 + d_1 \leq -z_{1,\min}$ <p style="text-align: center;">and</p> $-r_{1b} \sin \alpha_1 + h_{1/2} \cos \alpha_1 + d_1 \geq -z_{1,\max}$
<b>Leg Gap</b>	$\left(a_1 - r_{1b} \sqrt{1 + (\cot \theta_1 \cos \alpha_1)^2}\right) \sin \theta_1 - h_{1/2} \cos \theta_1 \sin \alpha_1 \geq \frac{y_{1,\min}}{2}$
<b>Leg Holes inside Briefs</b>	$(a_1 + r_{1b} \cos p)^2 + (h_{1/2} \sin \alpha_1 - r_{1b} \cos \alpha_1 \sin p)^2 \leq r_{1t}^2$ <p style="text-align: center;">for all <math>p</math> such that</p> $0 = a_1 \sin p + r_{1b} \cos p \sin p \sin^2 \alpha_1 + h_{1/2} \sin \alpha_1 \cos \alpha_1 \cos p$

(a) Briefs geometric constraints

<b>Frusta Length</b>	$a_n^2 + h_{n/n+1}^2 + (d_n - h_{n-1/n})^2$ $+ 2h_{n/n+1}(d_n - h_{n-1/n}) \cos \alpha_n \leq l_{\max}^2$
<b>Frusta Angle</b>	$\gamma_{\max} \text{ is in 1st quadrant,}$ $-\gamma_{\max} \leq \alpha_n \leq \gamma_{\max}$
<b>Frusta Skew</b>	$h_{n/n+1}^2 \sin^2 \alpha_n + a_n^2 \leq r_{nt}^2$ <p style="text-align: center;">and</p> $(h_{n-1/n} - d_n)^2 \sin^2 \alpha_n + a_n^2 \leq r_{nb}^2.$
<b>Frusta Height</b>	$d_n + h_{n/n+1} \cos \alpha_n + r_{nb}  \sin \alpha_n  \leq h_{n-1/n}.$
<b>Frusta Edge Gaps</b>	$\forall p_t \in [0, 2\pi), \forall p_b \in [0, 2\pi), (r_{nt} \cos p_t \pm r_{nb} \cos p_b \pm a_n)^2$ $+ (r_{nt} \sin p_t \pm r_{nb} \sin p_b \cos \alpha_n \mp h_{n/n+1} \sin \alpha_n)^2$ $+ ((h_{n-1/n} - d_n) - r_{nb} \sin p_b \sin \alpha_n - h_{n/n+1} \cos \alpha_n)^2 \geq l_{\min}^2,$ <p style="text-align: center;">where the sign of <math>\pm</math> is the sign on <math>\cos \theta_n</math></p>

(b) Proximal and Distal Sections ( $n \in \{2, 3\}$ ) geometric constraints.

Table 4.1: Summary of geometric constraints on HBA components, described in Sections 4.1.1 and 4.1.2, expressed in parameter variables. Derivations can be found in Appendix E.

## 4.2 Parameter Bounds

The geometric constraints in Section 4.1 are applicable to any implementation of this model on the HBA, as they are applied to ensure the HBA is wearable and usable. The parameter bounds discussed in this section are not. These bounds were derived to limit the HBA tradespace, discussed in Chapter 5.

To arrive at a tradespace that could be deeply investigated, simplifying assumptions were made. Some parameters were set to constants. All radii of the component edges ( $r_{1t}$ ,  $r_{1b}$ ,  $r_{2t}$ ,  $r_{2b}$ ,  $r_{3t}$ , and  $r_{3b}$ ) were kept the same as in the nominal HBA. The radii are germane to a number of questions regarding space suit design, such as fleet sizing, but they do not affect the motion of the HBA model, which depends only on the DH parameters. The radii do affect the ROM of the occupant, discussed in Chapter 3, as the occupant's limbs have greater range to move within components that have larger radii. However, the magnitude of this effect would be highly coupled to the size of the occupant's leg, which was also kept constant in this research and not considered here. Additionally, an HBA with different radii would require different bearings, making the cost/benefit analysis of different radii more complex. For this research, the radii were kept constant, assuming the same bearing hardware was used in the new geometries, and exploring the best HBA geometry that did not require new bearings.

The  $\theta$  parameters for the Proximal and Distal Sections were also kept constant, set to  $\pi$  and 0, respectively. These are the same as the values in the nominal HBA. All other parameters had upper and lower bounds determined. Some bounds were selected to enforce desired structure, such as requiring all values of  $d$  and  $x$  parameters to be less than 0. Other bounds were generally selected to give a reasonably large exploration region. To ensure the possibility space was fully explored, bounds

outside the space of valid geometries were preferred (when possible), so that geometric constraints would limit the explored geometries, not the bounds themselves.<sup>6</sup> The bounds, the reasoning behind them, and the value of each parameter in the nominal HBA can be seen below. If not otherwise specified, the values of the bounds were selected to produce a reasonably large exploration region. The specific values are also listed in Table 4.2.

- $h_{0/1}$  was kept constant as this parameter specifies the distance between the HBA and HUT, which does not affect the estimated hip ROM, which is the metric analyzed in the tradespace exploration.
- $a_1$  has a nominal value of 0.0316 m and represents the radial distance that the Proximal Section origin lies from the Briefs origin. A value that is nearly 400% of the nominal was permitted, as well as a negative value of the same magnitude, limiting  $a_1$  between -0.125 and 0.125. This range is a superset of  $a_1$  values that appear in valid geometries. The values of  $a_1$  in viable geometries are limited by the Leg Holes inside Briefs constraint in Section 4.1.1, which enforces  $|a_1| \leq r_{1t} - r_{1b}$ . With the values of  $r_{1t}$  and  $r_{1b}$ , this means  $|a_1| \leq 0.0978$ .
- $d_1$  is the vertical separation between the Briefs origin and the Proximal Section origin. In the nominal HBA, it has a value of -0.1057 m. The Briefs should not be too tall, so a limit of -0.2 m was selected as the lower bound. For an upper bound, the model detailed in Chapter 2 assumes the origin of the Proximal Section frame (frame 2) must be beneath the origin of the Briefs frame (frame 1). Thus, the upper bound of  $d_1$  was set to be 0.

---

<sup>6</sup>Due to this, for many of the bounds, there are zero viable geometries with parameters with that value. One clear example is the bounds on  $\alpha_1$ , which are  $\pm \frac{5\pi}{8}$ . The Leg Direction constraint in Section 4.1.1 requires  $\cos \alpha_1 \geq 0$ , so the space of explored values of  $\alpha_1$  is a superset of the values of  $\alpha_1$  that appear in valid geometries.

- $\theta_1$  is related to  $a_1$ . It represents the radial direction of the Proximal Section origin from the Briefs origin ( $a_1$  is the radial distance). The nominal HBA has a value of 2.7925 radians. We could allow the angle to vary from 0 to  $2\pi$ , but this was found to be unnecessary. As  $a_1$  was permitted the same range with both signs, the same result can be achieved with half of the angle. Thus,  $\theta_1$  was limited between  $\frac{\pi}{2}$  and  $\frac{3\pi}{2}$ .  $\theta_1$  also controls the direction of  $\alpha_1$  rotation and the  $x$ -axis of the Proximal Section Frame. However, as shown in the following item,  $\alpha_1$  was allowed to hold the same values with both positive and negative signs, so the same set of possible rotations could be achieved with these limits on  $\theta_1$ . This same argument applies for all subsequent transformations. All parameters used in transformations that would be affected by the direction of  $\theta_1$  could assume the same positive or negative values of the same magnitude, preserving generality. These include  $a_1$ ,  $\alpha_1$ ,  $a_2$ ,  $\alpha_2$ ,  $a_3$ , and  $\alpha_3$ .
- $\alpha_1$  represents the  $x_1$ -axis rotation between the Briefs frame and the Proximal Section frame. It has a value in the nominal HBA of -0.9076 radians. For the geometry to be viable, the leg holes of the Briefs must not point upwards. Thus,  $\alpha_1$  was allowed to represent up to a right angle in either direction. The boundaries were set at  $\pm\frac{5\pi}{8}$  to provide some margin, though the geometric constraints from Section 4.1 mean that the values in that margin were not valid geometries.<sup>7</sup>
- $h_{1/2}$  nominally has a value of -0.1275 m. It was allowed to nearly double, with an upper bound of -0.25 m. This bound is reasonable; for values of a larger magnitude, the Briefs would become impracticably large. For the HBA

---

<sup>7</sup>This is acceptable, as it is better for the exploration space to be bounded by geometric constraints based on what geometries are viable than the assigned parameter bounds, so the tradespace is not limited by the parameter bounds selected.

structure to be valid, the Briefs bottom edges were required to fall below the Proximal Section frame (frame 2) origin, so the upper bound was set to zero.

- $a_2$  and  $a_3$  have nominal values of 0.0049 m and 0 m, respectively.  $a_2$  represents the radial distance that the Distal Section frame (frame 3) origin lies from the Proximal Section frame (frame 2) origin, while  $a_3$  does the same for between the Distal Section frame (frame 3) origin and the thigh component's frame (frame 4) origin. Both were limited between -0.1 and 0.1, as a component with too large of a translation would be infeasible.
- $d_2$  is the vertical displacement between the Proximal Section frame (frame 2) origin and the Distal Section frame (frame 3) origin.  $d_3$  is the same between the Distal Section frame (frame 3) and the next section's frame (frame 4) origin. In the nominal HBA, they have a value of -0.1027 m and -0.0897 m, respectively. To avoid lengthy components a limit was created for both, setting -0.2 m as the lower bound. The model of HBA structure in Section 2.3 assumes each origin is "beneath" the previous origin, so zero was set as the upper bound.
- $\theta_2$  and  $\theta_3$  are the directions of the translation between the Proximal Section frame (frame 2) origin and the Distal Section frame (frame 3) origin and between the Distal Section frame (frame 3) origin and the thigh component's frame (frame 4) origin, respectively. They have values of  $\pi$  and 0, respectively, in the nominal HBA and were kept as such. The components rotate around their  $z$ -axes due to the motion of their bearings, the same motion controlled by  $\theta$ . Any change in  $\theta$  can be duplicated or countered by rotating the bearing. Therefore, the only effect of  $\theta$  is to adjust the neutral or zero position of the



bearing. Without loss of generality, we assigned them to specific values and removed a dimension from the problem. They were assigned  $\pi$  and 0 because these values were convenient, matched the nominal HBA, and placed the axes in an easily-understood manner ( $x$ -axes pointing forward).<sup>8</sup>

- $\alpha_2$  and  $\alpha_3$  have nominal values of -0.3976 rad and -0.4037 rad, respectively.  $\alpha_2$  represents the  $x_2$ -axis rotation between the Proximal Section frame (frame 2) and the Distal Section frame (frame 3), while  $\alpha_3$  does the same for the Distal Section frame (frame 3) and the thigh component's frame (frame 4). They control the angles between the two holes of the Proximal and Distal Section. If either component had too sharp of a bend, the occupant would not have been able to wear it and it would not be a viable geometry. Thus, both were bounded at  $\pm\frac{\pi}{2}$ , allowing a wide range of angles. This limit is beyond the values of  $\alpha_2$  and  $\alpha_3$  allowed in valid HBA geometries. They are restricted to  $\pm\frac{\pi}{3}$  by the Frusta Angle constraint in Section 4.1.2.
- $h_{2/3}$  and  $h_{3/4}$  currently have values of -0.0867 m and -0.1003 m, respectively. We set the upper bounds for both to be -0.25 m. These bounds are reasonable as, for larger values, the Proximal/Distal Sections would become impractically large. For a valid geometry, the bottom edge should be distal to the origin of the next frame. This required the upper bound to be zero.

---

<sup>8</sup>While we set  $\theta_2$  and  $\theta_3$  to specific values as described here, we did also add a neutral rotation to make the  $x$ -axes level in the zero position. For a specific position, this could be considered equivalent to having a different  $\theta$  value, but in other positions this  $\theta$  would not bring the relevant  $x$ -axes into alignment. Instead we simply follow the DH procedure as described, then redefine the neutral position as the zero position and assign rotation values from there. The formula we use to find this neutral position is only used for the middle bearing, and is  $\eta_3 = -\text{atan2}(-\sin(\theta_1), -\cos(\theta_1)\cos(\alpha_3 + \alpha_2 - \alpha_1))$ . In other words, we adjust a provided  $\phi$ , representing the kinematic position of the bearing, by  $\eta_3$ . It would also be applied to the upper bearing, but the solution is always 0, rendering it unnecessary for that bearing.

Parameter	Unit	Mark III Value	Lower Bound	Upper Bound
$h_{0/1}$	m	0	0	0
$r_{1t}$	m	0.2318	0.2318	0.2318
$a_1$	m	0.0316	-0.125*	0.125*
$d_1$	m	-0.1057	-0.2	0 <sup>†</sup>
$\theta_1$	rad	2.7925	$\frac{\pi}{2}$ <sup>‡</sup>	$\frac{3\pi}{2}$ <sup>‡</sup>
$\alpha_1$	rad	-0.9076	$-\frac{5\pi}{8}$ *	$\frac{5\pi}{8}$ *
$h_{1/2}$	m	-0.1275	-0.25	0 <sup>†</sup>
$r_{1b}$	m	0.1340	0.1340	0.1340
$r_{2t}$	m	0.1575	0.1575	0.1575
$a_2$	m	0.0049	-0.1	0.1
$d_2$	m	-0.1027	-0.2	0 <sup>†</sup>
$\theta_2$	rad	$\pi$	$\pi$	$\pi$
$\alpha_2$	rad	-0.3976	$-\frac{\pi}{2}$ *	$\frac{\pi}{2}$ *
$h_{2/3}$	m	-0.0867	-0.25	0 <sup>†</sup>
$r_{2b}$	m	0.1275	0.1275	0.1275
$r_{3t}$	m	0.1400	0.1400	0.1400
$a_3$	m	0	-0.1	0.1
$d_3$	m	-0.0897	-0.2	0 <sup>†</sup>
$\theta_3$	rad	0	0	0
$\alpha_3$	rad	-0.4037	$-\frac{\pi}{2}$ *	$\frac{\pi}{2}$ *
$h_{3/4}$	m	-0.1003	-0.25	0 <sup>†</sup>
$r_{3b}$	m	0.1135	0.1135	0.1135

\* This bound is outside the limits on the parameter established by geometric constraints in Section 4.1, and thus does not prevent consideration of any viable geometries.

<sup>†</sup> This bound ensures proper structure.

<sup>‡</sup> This bound limits the exploration space to improve computation time, but all possible geometries are preserved.

Table 4.2: Table summarizing bounds on HBA parameters, including name, units of measurement, and value in the nominal HBA, the Mark III. Tinted rows indicate parameters that were kept constant in this research. Parameters are described in Section 2.2 and shown in Figure 2-3, while their bounds can be found in Section 4.2.

# Chapter 5

## Hip Bearing Assembly Tradespace Analysis

The possibility of adjusting the Mark III Hip Bearing Assembly (HBA) geometry to improve occupant's mobility during gait was considered. The model in Chapter 2 was applied to the HBA. By changing the parameters, new HBA geometries could be generated.

Potential new HBA geometries were evaluated in a tradespace analysis. The tradespace was bounded by the limits described in Chapter 4. The geometries within these bounds were evaluated using the ROM-scoring method detailed in Chapter 3 (scored against the hip gait Unsuiting ROM example, Section 3.1). The details of the method used for the tradespace analysis are described in Section 5.1. A preliminary tradespace exploration was conducted, analyzed in Section 5.2. Based on those results, a second, more refined, exploration was performed, detailed in Section 5.3. These explorations generated new ideas for HBA geometries, which are discussed in Section 5.4, and provided insight into a number of questions related to suit geometry,

detailed in Section 5.5.

## 5.1 Tradespace Exploration Method

Even with the focus limited to the human hip range of motion (ROM) and the HBA geometry parameterized into a thirteen-dimensional space, the space of possible HBA geometries is complex to explore. The impact of the parameters on the ROM score in Section 3.3 is highly nonlinear, with many local minima and maxima. These issues preclude an optimization approach. Instead, to explore the tradespace and understand how ROM score variations, the HBA geometry was sampled at a number of points throughout and the ROM was analyzed for each.

To explore the tradespace, ten values were selected for each parameter, evenly spaced between the boundaries in Section 4.2, in addition to the parameter's value in the nominal HBA. For both explorations, a subset of these eleven values was considered for each parameter. Every combination of parameter values was tested. If a geometry was invalid, by breaching any of the geometric constraints described in Section 4.1, that geometry was discarded. Geometries that were deemed viable had structures and surfaces generated using the methodology described in Sections 2.3 and 2.4, and their Suited ROMs calculated and scored as detailed in Sections 3.2 and 3.3. This approach was implemented in MATLAB.

The tradespace was explored using fewer faces per surface and fewer poses to estimate the ROM score of every geometry. After the tradespace was tested at this level of accuracy, select geometries (such as those discussed in Section 5.4, as well as the nominal HBA) were re-evaluated with a higher fidelity. The differences between the calculations are:

- There were  $N_1 = 20$  points<sup>1</sup> around the edge of each component for tradespace tests, but  $N_1 = 50$  for visualization and higher-fidelity calculations.
- There were  $N_2 = 5$  points<sup>2</sup> along each subsurface used to generate the Briefs surface during tradespace tests, but  $N_2 = 20$  for visualization and higher-fidelity calculations.
- Bearing thicknesses were set to  $l_{n/n+1} = 0.01$  m for all bearings.
- For the tradespace tests, the increment in bearing position angle used to generate Suited ROM was  $\Delta\phi = 5^\circ$ . For the higher-fidelity tests,  $\Delta\phi = 2^\circ$ .
- For both the tradespace tests and higher fidelity calculations, the bounds on the bearing positions for both the upper and middle bearings were  $\phi_{n,\min} = -90^\circ$  and  $\phi_{n,\max} = 90^\circ$ .

Several simplifications were also made:

- The HBA was treated as symmetric across the sagittal plane up to rotation of the bearings. For both the Proximal and Distal Sections, the right-leg component had the same parameterization as the left-leg, with the signs of the  $\alpha$  and  $\theta$  inverted. The Briefs were symmetric across the sagittal plane, so any point in the Briefs frame on the right half  ${}^1\vec{v}_R$  can be converted from an equivalent left-half vector,  ${}^1\vec{v}_L$  by changing the sign on the  $y_1$ -coordinate, as seen in Equation 2.10. This simplifies the physical structure of the Briefs and HBA. Only one bottom edge radius,  $r_{1b}$  is required for the Briefs, and the bottom edge on the left side is simply reflected across the sagittal plane to find the right side.

---

<sup>1</sup>As mentioned in Section 2.4, there were actually  $N_1 + 1$  points between 0 and  $2\pi$ , but when considering a circle, 0 and  $2\pi$  are equivalent, so there are only  $N_1$  distinct points.

<sup>2</sup>As mentioned in Section 2.4, there were actually  $N_2 + 1$  points along each sub-surface.

The  $\tau_n(p)$  and  $\beta_n(p)$  index adjustments for the component edges, described in Equations 2.7 and 2.8, are used as well.

- Only the Briefs and Proximal and Distal Sections were tested for intersection with the simulated thigh in Suited ROM estimation. The waist bearing was not considered due to its distance well above the hip. The lower bearing and the material corresponding to the soft goods distal to the HBA could be tested, but it is unnecessary. The simulated thigh starts within the HBA. Given the location of the hip and knee points and the lower sections, the thigh cannot be exiting the suit volume from those sections. Therefore, if there was any intersection with those component surfaces, it would come from the thigh re-entering the suit volume. For that to occur, there must be another intersection in the higher components. Thus, no intersection would occur in the lower bearing or thigh component without an intersection in the components already being tested. The lower bearing and thigh component can be neglected for efficiency.
- The hip and knee positions of the simulated thigh are defined as specific points relative to the HBA geometry (see Section 3.2.1), so the length of the simulated thigh changes with different HBA geometries and different parameters. In addition to the geometry, this length changes with the pose of the HBA, as noted in Section 3.2.1. Therefore, selecting a specific thigh length and constraining the HBA geometry to meet that length requires choosing a reference position in which to measure. Given the variability of the distance between two points on the suit geometry (an issue in the nominal HBA and any design with a construction such as this), the specific-length approach was rejected. Instead, the simulated thigh was represented by a pair of two specific locations in the

HBA, defined relative to the geometry. As detailed in Section 3.2.1, the hip point was the centroid of the upper bearing and the knee point was located a constant distance from the origin of frame 4.

## 5.2 Preliminary Tradespace Exploration

The initial attempt at sampling the tradespace used five values for each of the thirteen parameters, including the value held by the parameter in the nominal HBA. The values considered for each parameter are presented in Table 5.1.

Parameter (Units)	Values Explored				
$h_{1/2}$ (m)	-0.219	-0.188	-0.128*	-0.125	-0.0625
$a_1$ (m)	-0.0625	0.00	0.0313	0.0316*	0.0625
$d_1$ (m)	-0.175	-0.150	-0.106*	-0.100	-0.0500
$\theta_1$ (deg)	113	135	160*	180	225
$\alpha_1$ (deg)	-56.3	-52.0*	-28.1	0.00	56.3
$h_{2/3}$ (m)	-0.188	-0.125	-0.0938	-0.0867*	-0.0625
$a_2$ (m)	-0.0750	-0.0500	0.00	0.00492*	0.0500
$d_2$ (m)	-0.175	-0.150	-0.103*	-0.100	-0.0500
$\alpha_2$ (deg)	-45.0	-22.8*	-22.5	0.00	45.0
$h_{3/4}$ (m)	-0.219	-0.188	-0.125	-0.100*	-0.0625
$a_3$ (m)	-0.0750	-0.0500	0.00*	0.00	0.05
$d_3$ (m)	-0.175	-0.150	-0.100	-0.0897*	-0.05
$\alpha_3$ (deg)	-45.0	-23.1*	-22.5	0.00	45.0

Table 5.1: Values for each parameter that were explored in the preliminary tradespace exploration. The values equal to those of the parameter in the nominal HBA are indicated with an asterisk. (In some cases, such as  $a_3$ , the same value may have been used twice, due to the nominal value overlapping with one of the sample space values.)

Of the  $5^{13} = 1.22$  billion combinations of parameter values explored, 168,709 produced a viable geometry. Of these, 6,038 geometries had an ROM score greater than

Parameter (Units)	Mark III HBA	Preliminary Best	Refined Best
$h_{1/2}$ (m)	-0.128*	-0.128*	-0.128*
$a_1$ (m)	0.0316*	0.0313	0.0316*
$d_1$ (m)	-0.106*	-0.106*	-0.106*
$\theta_1$ (deg)	160*	160*	160*
$\alpha_1$ (deg)	-52.0*	-52.0*	-52.0*
$h_{2/3}$ (m)	-0.0867*	-0.188	-0.0867*
$a_2$ (m)	0.00492*	0.0500	0.0500
$d_2$ (m)	-0.103*	-0.0500	-0.175
$\alpha_2$ (deg)	-22.8*	-22.8*	-45.0
$h_{3/4}$ (m)	-0.100*	-0.219	-0.188
$a_3$ (m)	0.00*	0.0500	0.0750
$d_3$ (m)	-0.0897*	-0.0500	0.00
$\alpha_3$ (deg)	-23.1*	-23.1*	22.5

Table 5.2: Parameter values for Mark III HBA and top-scoring HBA geometries from tradespace exploration.

or equal to the nominal HBA. The HBA geometry with the highest ROM Score of those explored used the parameters listed in Table 5.2. This geometry is further discussed in Section 5.4.

The distribution of viable geometries across the values for different parameters can be seen in Figure 5-1. The specific score distribution across the parameters can be seen in Figure 5-2. For every parameter (excluding the Briefs parameters:  $h_{1/2}$ ,  $a_1$ ,  $d_1$ ,  $\theta_1$ , and  $\alpha_1$ ), it was observed that the the top-scoring value for the parameter does not have the most valid geometries. For example, there are more geometries where  $\alpha_1$  takes value 1 than value 2, but they have lower scores. This may indicate a difference between the Briefs and other components, a suggestion further supported by the observation that Briefs variables appear to have little effect on the design's ROM score.

There is only one valid value for  $a_1$ , and only two for  $d_1$ ,  $\alpha_1$ , and  $h_{1/2}$ . This is



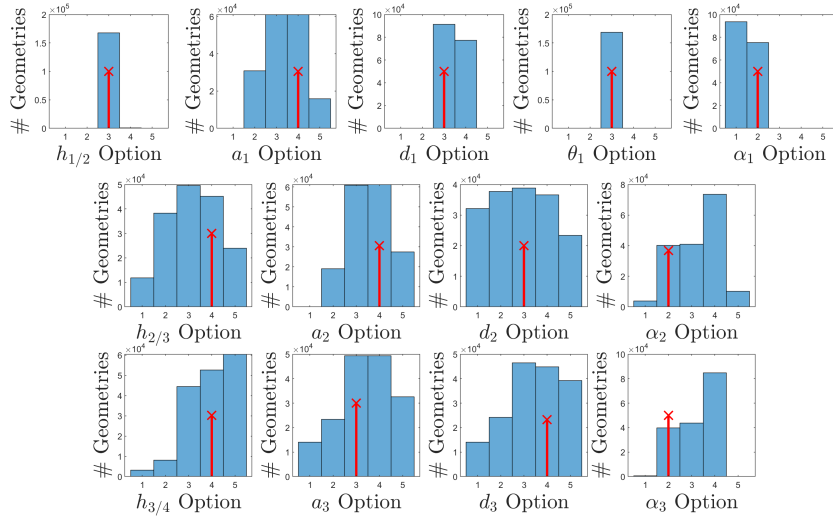


Figure 5-1: Histograms of parameter values occurrences in viable geometries from preliminary tradespace exploration. The red crosses indicate the parameter values of the nominal HBA.

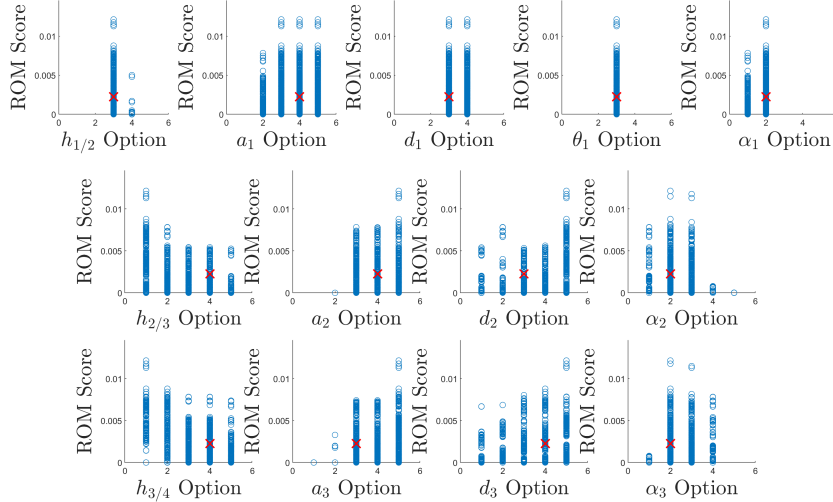


Figure 5-2: Distribution of ROM scores over parameter values from preliminary tradespace exploration. The red crosses indicate the score and parameter values of the nominal HBA.

generally a good sign, as it indicates the parameter bounds established in Section 4.2 did not artificially limit the possibility space. But the scores also show an interesting trend. In every case where there are two or more values, changing from the nominal value of the parameter to a different value has either no effect on the score distribution and top ROM score, or decreases the scores. There is generally little room for the Briefs to move from their current design, so many changes to the Briefs may simply result in nonviable geometries. It is also worth noting that the hip point used when calculating ROM falls in the centroid of the upper bearing, whose location is defined by the Briefs. Due to this connection, changing the Briefs moves the hip point (and simulated leg). Most of the Briefs geometry is therefore above the simulated leg and would not cause intersection or a lower ROM score. This could mitigate some of the losses in ROM that might otherwise occur.

### 5.3 Refined Tradespace Exploration

The results discussed in Section 5.2 indicated that altering the geometry of the Briefs generally did not impact the results. The altered Briefs were either an invalid geometry or had little impact on the Suited ROM. Thus, the tradespace was re-explored, with the Briefs held constant and the other components explored more deeply.

For the refined tradespace sampling, the Briefs parameters ( $h_{1/2}$ ,  $a_1$ ,  $d_1$ ,  $\theta_1$ , and  $\alpha_1$ ) were set to their values from the nominal HBA, and the remaining eight were explored with ten possibilities each, including their nominal value. The values explored can be seen in Table 5.3.

Of the  $10^8 = 100$  million combinations of parameter values explored, 124,390 had a viable geometry. Of these, 5,142 geometries had an ROM score greater than or

		Values Explored											
$h_{1/2}$ (m)		-0.128*											
$a_1$ (m)		0.0316*											
$d_1$ (m)		-0.106*											
$\theta_1$ (deg)		160*											
$\alpha_1$ (deg)		-52.0*											
$h_{2/3}$ (m)	-0.250	-0.219	-0.188	-0.156	-0.125	-0.0938	-0.0867*	-0.0625	-0.0313	0.00	0.00	0.00	0.00
$a_2$ (m)	-0.100	-0.0750	-0.0500	-0.0250	0.00	0.00492*	0.0250	0.0500	0.0750	0.100	0.100	0.100	0.100
$d_2$ (m)	-0.200	-0.175	-0.150	-0.125	-0.103*	-0.100	-0.0750	-0.0500	-0.0250	0.00	0.00	0.00	0.00
$\alpha_2$ (deg)	-90.0	-67.5	-45.0	-22.8*	-22.5	0.00	22.5	45.0	67.5	90.0	90.0	90.0	90.0
$h_{3/4}$ (m)	-0.250	-0.219	-0.188	-0.156	-0.125	-0.100*	-0.0938	-0.0625	-0.0313	0.00	0.00	0.00	0.00
$a_3$ (m)	-0.100	-0.0750	-0.0500	-0.0250	0.00*	0.00	0.0250	0.0500	0.0750	0.100	0.100	0.100	0.100
$d_3$ (m)	-0.200	-0.175	-0.150	-0.125	-0.100	-0.0897*	-0.0750	-0.05	-0.0250	0.00	0.00	0.00	0.00
$\alpha_3$ (deg)	-90.0	-67.5	-45.0	-23.1*	-22.5	0.00	22.5	45.0	67.5	90.0	90.0	90.0	90.0

Table 5.3: Values for each parameter explored in the refined tradespace exploration. The value in the nominal HBA is indicated with an asterisk.

equal to the nominal HBA. The geometry with the highest ROM Score of those explored used the parameters listed in Table 5.2. This geometry is further discussed in Section 5.4. We can see in Figures 5-3 and Figure 5-4 that there are a number of valid and well-scoring geometries spread across the values for each parameter.

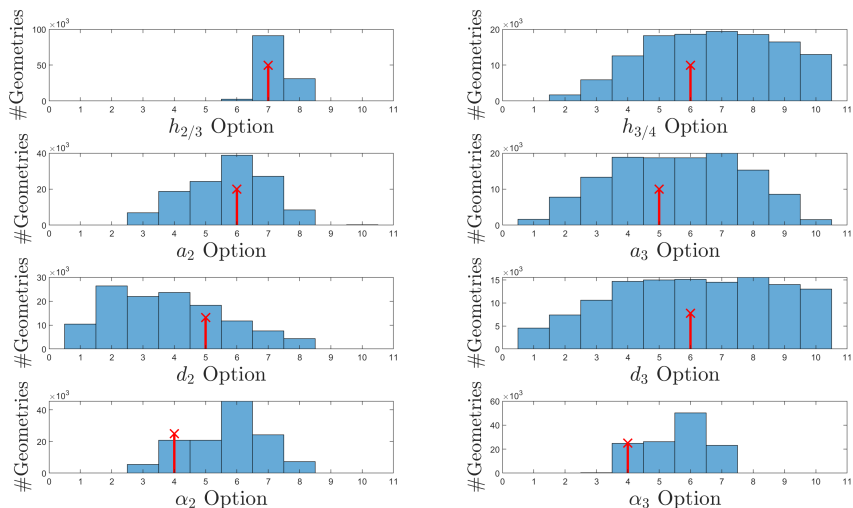


Figure 5-3: Histograms of parameter value occurrences in viable geometries from refined tradespace exploration. The red crosses indicate the parameter values of the nominal HBA.

From the score distribution and histogram, we can see that  $h_{2/3}$  is the most limiting parameter of the remaining eight. Only three values yield any viable geometries at all. This likely stems from some combination of the geometric constraints described in Section 4.1. The other parameters appear to have more complex relationships with the ROM scores. For example, it appears the the maximum score increases with  $\alpha_2$  decreases and  $\alpha_3$  increases, suggesting that the angles of the of the Proximal and Distal Sections may play a key role in the ROM score. Some of these trends are further explored in Section 5.5.2.

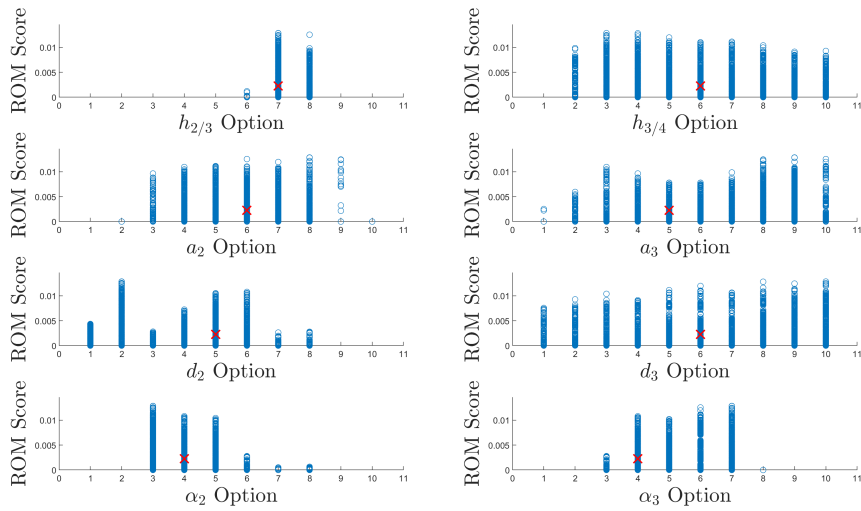


Figure 5-4: Distribution of ROM scores over parameter values from refined tradespace exploration. The red crosses indicate the score and parameter values of the nominal HBA.

## 5.4 Suggested Geometries

The parameters of the top-scoring HBA geometries are presented in Table 5.2. The scores of these geometries are detailed in Table 5.4. Additionally, a programming implementation error resulted in the bearings used in the ROM calculations for tradespace exploration taking  $g_{n/n+1}$  values that were off by 0.0014 and 0.003 m. The effect of this offset should be similar to using slightly thinner or shorter bearings. The two top-performing ROM and the nominal design had their ROM scores re-calculated with the error resolved. These results are also shown in Table 5.4. In that table, we can see that the ROM score of the nominal HBA is stable over changes in fidelity and the bearing error. Changing from low- to high-fidelity for the other geometries affected the ROM scores to a greater extent, but did not dramatically change their standing. Correcting for the bearing error had little effect on the scores, as well.

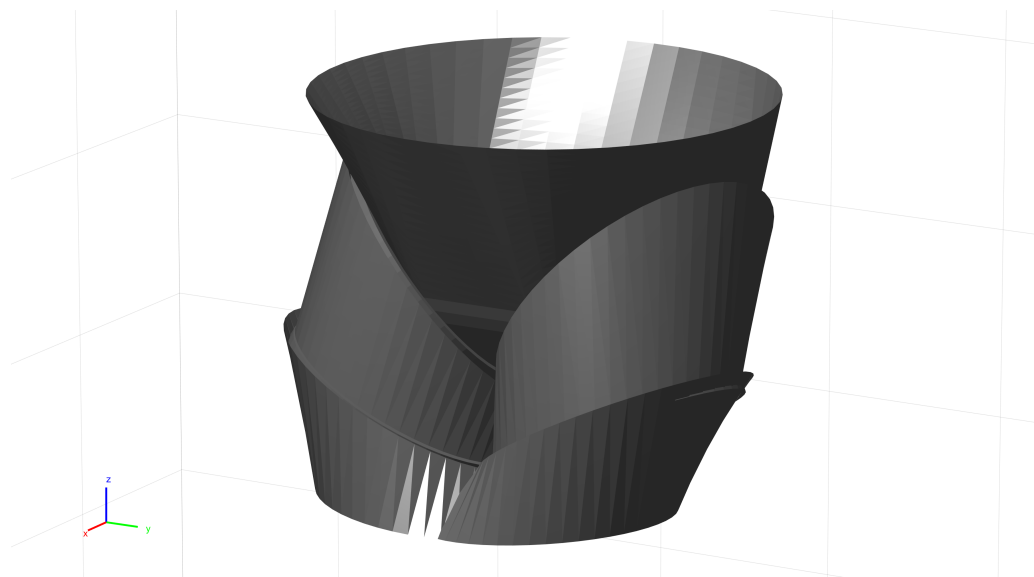
All further discussion using these geometries will be based on the high-fidelity scores with corrected bearings.

	Nominal	Preliminary	Refined
low-fidelity ROM score	0.0023	0.0121	0.0128
high-fidelity ROM score	0.0023	0.0115	0.0148
Fidelity % change	0.9%	-5.6%	15.3%
ROM score with corrected bearings	0.0023	0.0121	0.0141
Bearing error % change	0%	5.3%	-5.1%
% improvement on nominal HBA	-	429.5%	515.8%

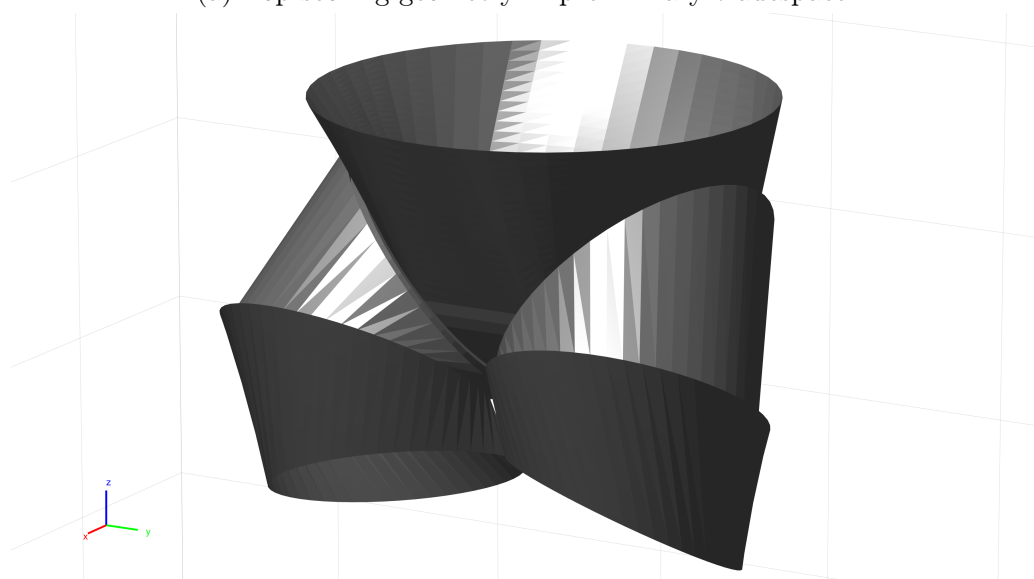
Table 5.4: Summary of ROM scores for the nominal HBA and the top performing geometries in the preliminary and refined tradespace explorations. The ROM score with corrected bearings uses the high-fidelity calculation. The bearing error change compares the high-fidelity scores with and without the bearing correction. The overall improvement percentage compares the high-fidelity, corrected-bearings scores between the new geometries and the nominal.

One other clear takeaway from Table 5.4 is the marked improvement that both tradespace-derived HBA geometries have over the nominal case. The Suited ROMs of these designs and the nominal case are shown in Figure 5-6 and the geometries themselves can be seen in Figure 5-5. It is immediately apparent from Figure 5-6 that the Suited ROMs of the geometries found during tradespace exploration have a much greater overlap with the Unsited ROM, compared to the nominal HBA. Both the preliminary and the refined geometries permit markedly more adduction, allowing the occupant’s feet to be placed closer to the sagittal plane (running through the body midline) or even in line with one another. This increased adduction, along with the greater overlap with the Unsited ROM, should allow occupants to have a more natural gait.

The recommended geometries also make the Unsited ROM extension range more accessible, due to the increased overlap. The ROMs of both highlighted HBA ge-



(a) Top-scoring geometry in preliminary tradespace.



(b) Top-scoring geometry in refined tradespace.

Figure 5-5: Visualization of top-scoring HBA geometries from preliminary and refined tradespace explorations. Visualizations were created using the model in Chapter 2.

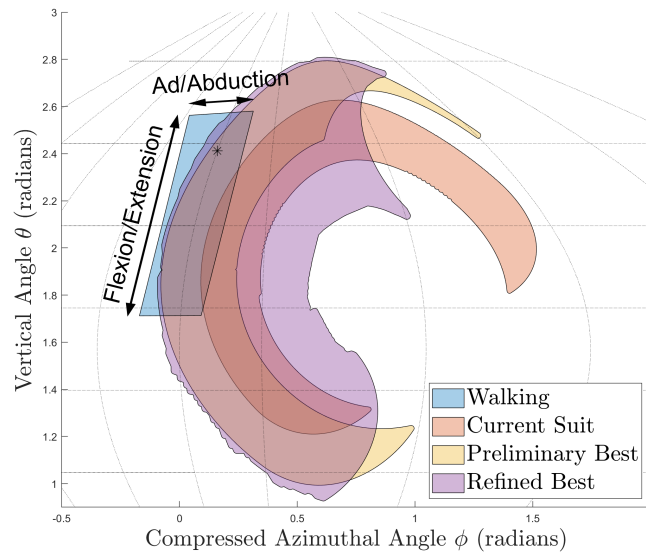


Figure 5-6: Visualization of Suited ROM for top-scoring geometries from preliminary and refined tradespace explorations, compared against the Unsited ROM for gait and the Suited ROM for the nominal case. ROMs are plotted according to the methodology described in Section 3.3. The black star indicates the downward direction, corresponding to the leg's neutral position.



ometries include the leg’s neutral position (straight down, indicated by the black star in Figure 5-6), allowing for a more natural neutral stance. While both are advantageous, the result from the refined tradespace has a higher score and its overlap with the Unsuit ROM is a superset of the overlap from the preliminary tradespace result. Thus, the geometry from the refined tradespace geometry is recommended.

## 5.5 Discussion

The results in Sections 5.2 and 5.3, as well as the highest-scoring geometry presented in Section 5.4, raise a number of interesting points regarding suit geometry. Several are explored in this section. The impact of joint number (simulated with aligned bearings) is discussed in Section 5.5.1. A basic analysis of the overall impact of HBA geometry is detailed in Section 5.5.2. The effect of the top-scoring HBA geometry on the ability of an occupant to kneel is considered in Section 5.5.3.

### 5.5.1 Number of Joints

The HBA geometries tested were all modified from the Mark III HBA, which has three bearings.<sup>3</sup> Two-bearing geometries were not specifically considered. However, HBA geometries with adjacent aligned bearings were considered. Adjacent aligned bearings are two bearings separated by a single component, where the axis of the bearings are collinear, making the component between them form a simple cylinder. In the parameterization detailed in Section 2.2, geometries where  $a_2 = \alpha_2 = 0$  or  $a_3 = \alpha_3 = 0$  have adjacent aligned bearings. An example can be seen in Figure 5-7.

---

<sup>3</sup>To measure the ROM, as described in Section 3.2, the upper and middle bearing are rotated. There is also the lower bearing, which is assumed to be aligned with the leg. Rotating that joint would correspond to internal/external rotation of the leg (turning the foot), and not affect the hip-knee line.

For designs described according to the model in Chapter 2, HBA geometries with

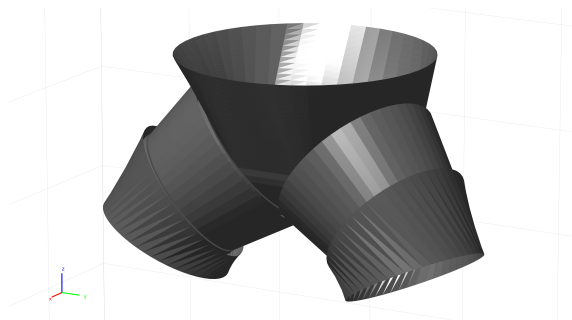


Figure 5-7: HBA geometry featuring adjacent aligned bearings.

adjacent aligned bearings are analogous to suit designs with only two bearings. A summary of the statistics affiliated with the ROM scores for geometries with adjacent aligned bearings is shown in Table 5.5. It is clear these geometries score much lower than the HBA geometries overall. In both the preliminary and refined results (from Sections 5.2 and 5.3, respectively), the maximum and mean scores of geometries with adjacent aligned bearings are less than 10% of the maximum and mean scores of the geometries as a whole.

ROM Score Stat	Results from Preliminary			Results from Refined		
	Set 1 <sup>*</sup>	Set 2 <sup>†</sup>	All	Set 1 <sup>*</sup>	Set 2 <sup>†</sup>	All
Quantity	26628	45765	168709	8516	14266	124390
Min	0	0	0	0	0	0
Max	<0.001	0.0018	0.012	0	<0.001	0.013
Mean	<0.001	<0.001	<0.001	0	<0.001	<0.001

<sup>\*</sup> Set of geometries with  $\alpha_2 = a_2 = 0$ .

<sup>†</sup> Set of geometries with  $\alpha_3 = a_3 = 0$ .

Table 5.5: ROM score statistics from HBA geometries with adjacent aligned bearings. For comparison, the nominal HBA has a score of 0.0023 and the best-performing geometry has a score of 0.0141.

The HBAs with adjacent aligned bearings have lower ROM scores because their

motion is less similar to the actual hip, as they have only one degree of freedom (DoF). Restricting the multi-degree-of-freedom (MDoF) human hip joint to a single degree of freedom severely limits the Suited ROM of the occupant. Figure 5-8 shows the Suited ROM points for the geometries with adjacent aligned bearings that have the maximum ROM scores, for both the preliminary and refined results. The Suited ROM points (rather than the Suited ROM shape itself) were used to highlight how all the points fall on a single curve, due to the single degree of freedom in these designs. The points trace out single curves, indicating the significantly restricted ROM. The designs with adjacent aligned bearings would likely have significant impact on occupant mobility. This supports previous results that locking a bearing in the HBA would drastically reduce ROM [5].

### 5.5.2 Geometric Trends

With the hundreds of thousands of ROM scores for various HBA geometries, there is a question of what factors dominate the score or are shared between the top-scoring geometries, like those in Section 5.4. We can see in Figures 5-5a and 5-5b that the top-scoring suits from both the preliminary and refined tradespace explorations have a Proximal Section which is canted outward from the sagittal plane, and a Distal Section which is canted back towards the sagittal plane. This “out-in” geometry could be a key factor in the higher scores. The larger angles of the components allow for more of the unit sphere to be accessed, and the magnitude of the angles appears to allow greater adduction, a key factor in high ROM scores, given the location of the Unsited ROM. To determine possible causes for the higher scores, a Partial Least Squares Regression (PLS) was applied to the data from the refined tradespace study. The predictors used were the eight parameter variables that were not kept

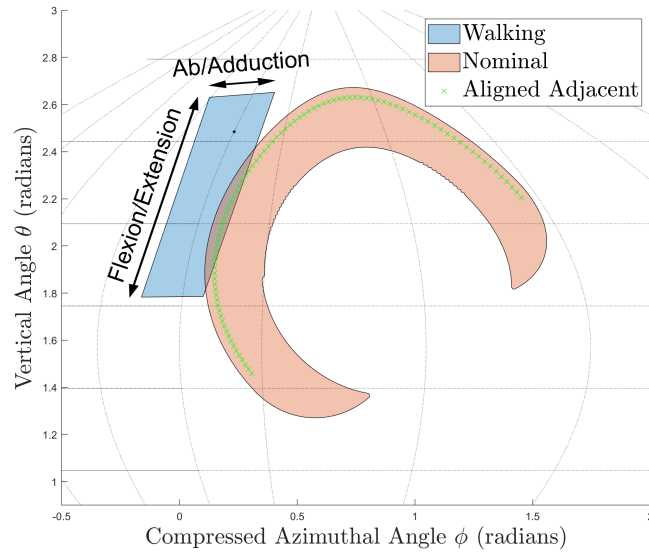


Figure 5-8: Comparison of Suited ROM for nominal HBA and an HBA with adjacent aligned bearings. The Unsited ROM for human gait is in blue, while the Suited ROM for the nominal HBA is in red. The green crosses show the points used in Suited ROM calculation for the top-scoring HBA geometry with adjacent aligned bearings.

constant in the refined tradespace study, and the responses were the ROM scores. The number of components was set at eight, equal to the number of variables. The Variable Importance in Projection (VIP) score was then determined from the loading matrices, to measure the impact of each parameter. The resulting VIP scores can be seen in Table 5.6. The VIP scores of parameters  $\alpha_2$  and  $\alpha_3$  were both greater than 1, indicating they were the most influential. These parameters seem to have the most influence on the ROM score of a given suit geometry.

Parameter	VIP Score
$h_{2/3}$	0.1731
$a_2$	0.1367
$d_2$	0.3403
$\alpha_2$	2.2906
$h_{3/4}$	0.6474
$a_3$	0.6074
$d_3$	0.6083
$\alpha_3$	1.19661

Table 5.6: VIP scores from PLS ( $N = 8$ ) on HBA geometry parameters and ROM scores from refined tradespace. The parameters  $\alpha_2$  and  $\alpha_3$  have VIP scores over 1, indicating influence.

### 5.5.3 Effect on Kneeling

The effect of the HBA geometry on gait is introduced in Chapter 1, and the particular impact of high-scoring suits from the tradespace exploration is discussed in Sections 5.4. While walking is a critical motion for astronauts in surface missions, kneeling or squatting motion should also be considered in space suit design. This motion is important for tasks as varied as scientific research, equipment setup and maintenance, and recovery after a fall. These tasks can be made easier or more difficult by the suit. Hard-joint suits have an advantage here. The soft hip joints of the EMU and Apollo suits make kneeling extremely difficult [1]. Hard-component hip joints, however, with their constant volume, are well-suited to solve this problem.

The impact of the recommended and nominal HBA geometries on kneeling is shown in Figure 5-9. The ROM plots from Section 5.4 were transformed to show the possible kneeling positions for each geometry. The shapes show the possible combinations of ab/adduction and flexion/extension (using the convention described in Section 3.1) for each design’s occupant. Any squatting or kneeling motion that requires flexion of more than 40 degrees will require at least 10 degrees of abduction

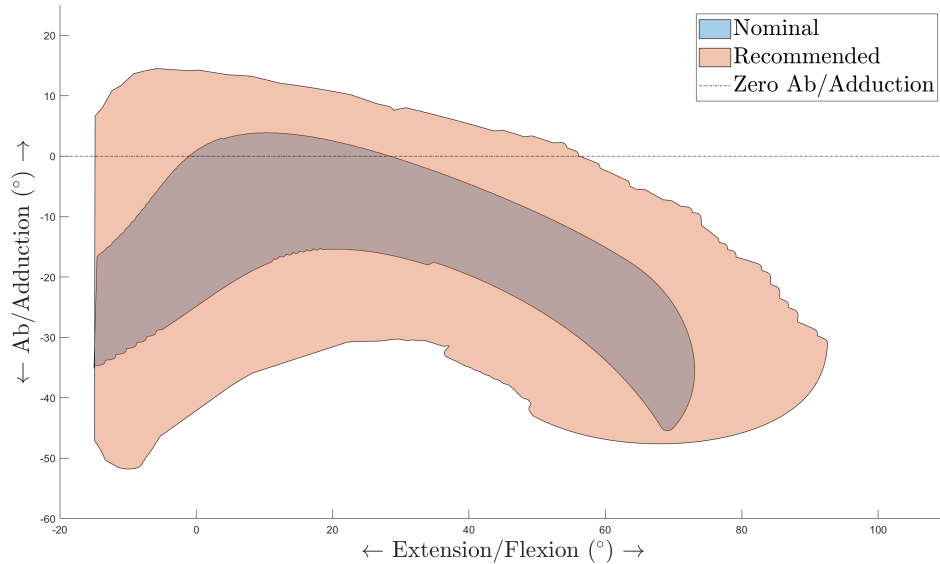


Figure 5-9: Comparison of ab/adduction required for kneeling/squatting between HBA geometries. The range of hip ab/adduction required for a given angle of hip flexion/extension is shown for each suit geometry. The nominal HBA is in blue, the best-performing suit geometry from the preliminary exploration is in red, and the best-performing geometry from the refined exploration is in yellow. The dashed black line shows the line of zero ab/adduction.

in the nominal HBA design. The recommended suit, described in Section 5.4, can reach over 50 degrees of flexion without requiring abduction. This design will allow a much greater range of kneeling or squatting motions<sup>4</sup> by allowing a greater degree of pure flexion/extension.

---

<sup>4</sup>This research is focused on ROM and the effect of hard joint suits. While the ROM may allow kneeling or squatting, other issues such as collisions between the legs (as referenced in Section 6.3) could inhibit these motions.

# Chapter 6

## Conclusion

### 6.1 Thesis Summary

The original Apollo space suit (the only space suit to be used on-mission in a planetary environment) used soft, flexible components for the limbs, which are susceptible to the springback forces caused by changes in volume. An alternative is using hard-component joints assemblies (HCJAs), like those used in the Hip Bearing Assembly (HBA) of the Mark III suit. However, the rigid components on these act as bounds on motion, which can restrict the mobility of the suit's occupant. This research developed a way to describe and study HCJAs and their effect on the occupant's range of motion.

A method of modeling the geometry of HCJAs was developed in Chapter 2 based on Denavit-Hartenberg parameters, with additional parameters to account for the size and placement of component edges and bearings. A method of generating edges from these parameters was explained, as well as an algorithm to generate surfaces representing the overall shape of each component. These surfaces are in the same

format as .STL files, allowing the output of this model to be easily converted and imported to various computer modeling programs.

In Chapter 3, a system to find and describe the range of motion (ROM) of an HCJA occupant's joint was described, as well as a method of comparing it to the overall ROM for that joint or the task-specific ROM. The approach considered human-suit interaction as well as the different kinematic arrangements of the suit.

The model was applied to the HBA, and the parameters were used to develop design constraints for the HBA based on utility and feasibility, described in Chapter 4. Bounds for various parameters were also created, to limit the design space.

A wide range of alternate HBA geometries were evaluated in two tradespace analyses, where a variety of values for thirteen model parameters were explored. The possible designs were scored using the ROM comparison method, focusing on potential geometries that could improve the Suited hip gait ROM. From the results of these tradespace analyses, a new suit geometry was suggested, detailed in Chapter 5. The range of motion of this geometry was visualized and compared to the range of motion necessary for gait and the range of motion for the nominal Mark III HBA. The effect of this design on kneeling was also discussed. The overall data set resulting from these analyses was used to consider the effect of the number of bearings and component angle on the occupant mobility.

## 6.2 Contributions

The key contributions found in this thesis are:

1. Developed a method of parameterizing the geometry of HCJAs in hard-joint suits using DH parameters, component edge radii, and bearing placement.



2. Presented a method of unambiguously converting HCJA models parameters into a three-dimensional representation of motion axes, edges, and surfaces, including in the .STL file format.
3. Analyzed possible constraints on HBA geometry necessary to ensure usability and feasibility, and simplified these constraints to the basic parameters used to describe the geometry.
4. Designed a method of estimating the ROM of a human's joint when wearing a hard-joint suit.
5. Created a metric to compare the ROM of a hard-joint suit occupant to the ROM necessary for gait or other unsuited tasks.
6. Explored two tradespaces defined by the geometric parameters and generated a recommended suit geometry that has significantly greater overlap with the Unsuited gait ROM than the nominal suit.
7. Investigated the HBA tradespace data set for notable conclusions, which suggested suits with fewer joints will have poor ROM and that the angles of the Proximal and Distal Sections had the largest influence on ROM score.

### 6.3 Limitations

The approach and results in this thesis were limited by, among other things, computational complexity. Simplifications (such as those listed in Sections 2.1 and 5.1) had to be made and some effects were not considered. These include:

- **Collision between legs:** The possible intersection of the legs is not inherently a problem; human legs have the range of motion to be in the same place at the

same time, but the Pauli exclusion principle prevents this, as it does with the suit. However, by comparing the Suited ROM to the Unsued ROM of gait, we are assuming that the occupant could use the Unsued ROM as effectively as an unsued person. Copying unsued gait motions while suited could result in collision between the legs of the suit, which was not considered. Further study and a more in-depth exploration of this question is needed, as mentioned in Section 6.4.

- **Varying thigh length:** As stated in Section 3.2.1, the simulated thigh used in this thesis varied in length based on the suit geometry and position of the knee. A different approach that adjusted the suit parameters but had a specified thigh dimension could result in improved estimations of ROM.
- **Human motion within the suit:** In this thesis, both the occupant’s hip and knee had a specific position relative to the suit geometry. This likely resulted in a reduced ROM measurement. When the occupant’s hips and knees can move around within the suit, a given kinematic arrangement can allow a range of occupant leg positions.
- **Leg compression:** To simulate the compression of the leg soft tissue against the components, a leg with reduced thigh and knee diameters was used. A more nuanced approach, considering how the leg would compress and to what extent, could produce more accurate results. To model human-suit interaction, this could also be incorporated with a finite element model, such as the one developed by King [14].
- **Motion of the rolling convolute:** The HBA of the Mark III suit is described as having three bearings, but actually has four degrees of freedom. In addition

to the upper, middle, and lower bearings, there is a convolute connected to the lower bearing that allows for small amounts of ab/adduction of the hip. This motion was not included when determining the Suited ROM in Section 3.2.2. Considering this motion in both the nominal suit and the geometries considered during tradespace exploration would yield ROMs with more ab/adduction.

- **Continuity of motion paths:** The Suited ROM regions is generated according to Section 3.2.2, where the relevant bearings are set to a given number of positions, and the thigh vector between the hip and knee is found. All of these vectors are considered as within the Suited ROM, and it does not consider whether two nearby vectors had bearing positions that were similar. Considering the bearing positions necessary for each point, and how to adjust the bearings to move between two thigh positions, could produce valuable insight into gait and other motions which require motion continuity.
- **Shape of human thigh:** The simulated thigh used in this thesis was treated as a truncated cone, while actual human thighs have a more complicated shape.
- **Internal and external rotation of the hip:** Due to the lower bearing being discounted (and allowed to assume any position), only the flexion/extension and ab/adduction of the hip were considered. However, the hip also allows for internal and external rotation, which is important during gait. As the human thigh is not actually a rotationally-symmetric truncated cone (see previous point), the internal and external rotation could affect the interactions between the suit and occupant.

## 6.4 Future Work

Many of the limitations discussed in Section 6.3 and simplifications mentioned in Section 2.2 could be addressed in future work on this material by:

- allowing varying component radii in the model,
- parameterizing the overlap of the different components,
- modeling components with non-zero thicknesses,
- allowing motion of the rolling convolute,
- testing and considering occupant motion within the suit, or
- better simulating the human thigh and the positions of the knee.

Any or all of these extensions should be considered, to find their effect on results shown here and to improve the accuracy of the model and methods discussed in this thesis.

The model and approach considered here could be applied to other problems. Particularly, extending this model to consider variations in anthropometry could be a very useful tool when considering fleet sizing for space suit components. By considering how various suit geometries affect ROM and fit for human bodies of various dimensions, a set of components could be found that maximize range of motion across people of different sexes, heights, weights, and proportions.

The techniques detailed in Chapters 2 and 3 can be applied to joints other than the hip. Space suits with HCJAs at locations other than the hips (including suits with rigid components over the entire body) have been considered in the past [10].

The techniques discussed in this thesis could be applied to HCJAs at the shoulder, ankle, or other joints, to understand the impact of the geometry on human mobility.

The boundaries and constraints described in Chapter 4 come from a variety of sources. However, some of the limiting values used in the constraints, such as the maximum height of the Briefs, could be varied to understand the impact on suit geometries in tradespace exploration.

This work is focused on the geometry of the components and the impact on human mobility. However, there are other important factors that should also be considered. One possible extension would be using or modifying this model to consider the effect of the structure of the suit necessary to support the bearings and fulfill the suit requirements. Other work that could be valuable would be to explore the tradespace using a more complex objective function. Instead of just mobility or ROM score, using a metric that also includes cost and mass could produce different conclusions and better reflect real-world concerns. Mass, in particular, is a significant downside to hard-joint suits [15].

Finally, the model described in Chapter 2, the bounds and constraints in Chapter 4, and the ROM calculations in Chapter 3 come from a foundation in mathematics and base principles. One clear extension to build on this work would be to construct physical models of various suit geometries (such as the top-scoring geometry in Section 5.4) and test them to determine their impact on ROM. This could be used to validate or improve the methods and model described in this thesis, and to better calibrate the constraints.



# Appendix A

## Definition of Anatomical Terms

This appendix is a brief description of several anatomical terms used in this thesis.

**Sagittal Plane:** The sagittal plane is one of three planes used to describe the body,<sup>1</sup> and runs through the midline of the body, dividing it into left and right sides. The sagittal plane of the Mark III Hip Bearing Assembly can be seen in Figure A-1.

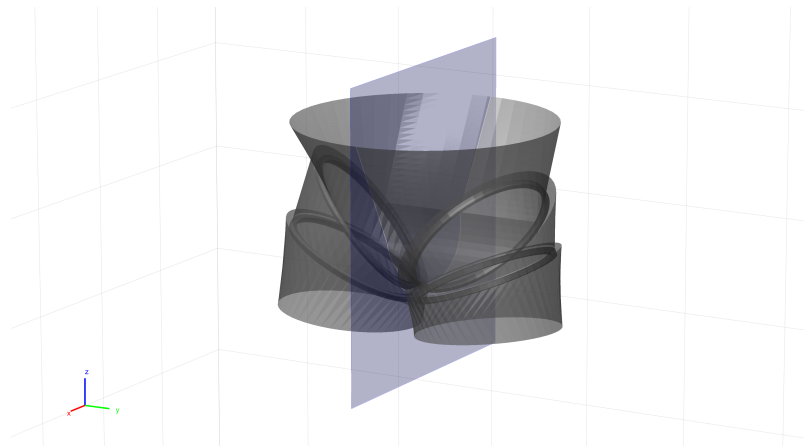


Figure A-1: Sagittal plane. The sagittal plane is divides the body into the left and right sides. The sagittal plane shown is for the Mark III Hip Bearing Assembly.

---

<sup>1</sup>The others are the frontal plane, which divides the body into front and back, and the transverse plane, which divides the body into top and bottom.

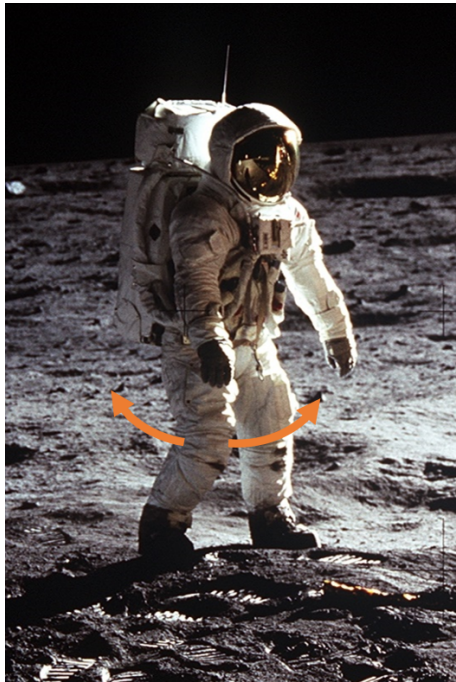


Figure A-2: Flexion and extension of the hip. Moving the hip forward is flexion, backward is extension. Source: NASA [20]. Image cropped and arrows added.

**Flexion/Extension:** Flexion describes bringing body parts closer together, reducing the angle between them. Extension describes moving body parts further apart, increasing the angle. In this thesis, flexion and extension of the hip is discussed. Flexion of the hip means bringing the thigh forward, as if kicking. Extension of the hip is the motion in the opposite direction. These can be seen in Figure A-2.

**Abduction/Adduction:** Abduction describes spreading the body further from the center, relative to the sagittal plane. Adduction describes bringing body parts closer to the center, in terms of the sagittal plane. In this thesis, abduction and adduction of the hip is discussed. Abduction of the hip would bring the knees further apart, such as widening one's stance. Adduction the hip is the motion in the opposite direction. These can be seen in Figure A-3.



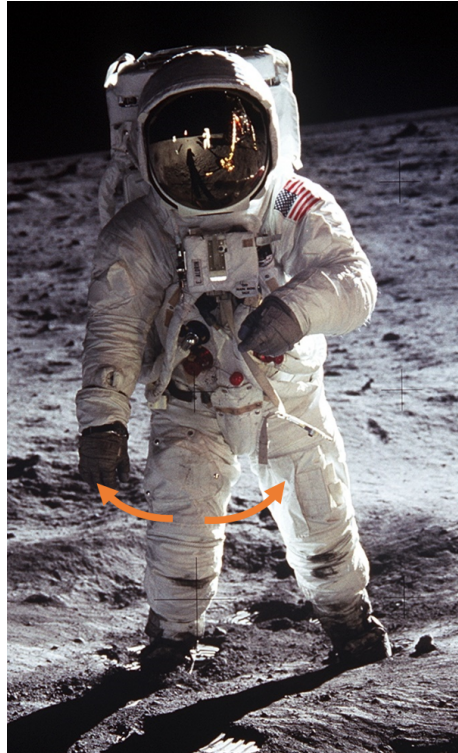


Figure A-3: Abduction and adduction of the hip. Moving the thigh inward, closer to the sagittal plane is adduction, moving outward or it further away is abduction. Source: NASA [21]. Image cropped and arrows added.



# Appendix B

## Sinusoidal Projection Proof

This appendix contains a proof that the sinusoidal projection and area calculation used in Section 3.3 provide an accurate measure of area on the surface of a sphere.

Consider the surface of the unit sphere,  $S_0$ . We aim to determine the area of a region on this surface,  $S$ . This can be done with a surface integral. The general form of surface integral is

$$\iint_D f(x, y, z) dS,$$

where  $D$  is the region on the surface to be measured in Cartesian space,  $dS$  is the infinitesimal portion of the surface (again, in Cartesian space), and  $f(x, y, z)$  is the value of the function being integrated over, described in Cartesian coordinates. If the surface is parameterized, as in our case, with

$$\vec{r}(u, v) = a(u, v)\hat{x} + b(u, v)\hat{y} + c(u, v)\hat{z},$$

then this formula can be rewritten as

$$\iint_{D'} f(\vec{r}(u, v)) \left\| \frac{\partial \vec{r}}{\partial u} \times \frac{\partial \vec{r}}{\partial v} \right\| dA,$$

where  $D'$  is the bounds of the region to be integrated over expressed in terms of  $u$  and  $v$ , and  $dA$  is the infinitesimal area in terms of  $u$  and  $v$ . The key difference in this expression is that, instead of integrating over  $x$ ,  $y$ , and  $z$ , we are now integrating over  $u$  and  $v$ .

For the region of the sphere we previously mentioned, this is exactly what we need. In our case, as we only care about area,  $f(x, y, z) = f(\vec{r}(u, v)) = 1$ , a constant. The region  $D$  is our region on the surface of the sphere  $S$ , and our parametric variables are  $\lambda$  and  $\xi$ , which (as stated in Section 3.3) are the variables used to represent spherical coordinates. Finally, because we are working on the surface of the unit sphere, we have

$$\vec{r}(\lambda, \xi) = (\cos \xi \sin \lambda) \hat{x} + (\sin \xi \sin \lambda) \hat{y} + (\cos \lambda) \hat{z} = \begin{bmatrix} \cos \xi \sin \lambda \\ \sin \xi \sin \lambda \\ \cos \lambda \end{bmatrix}.$$

With these substitutions, the formula for surface area in our case becomes

$$\iint_{S'} 1 \cdot \left\| \frac{\partial \vec{r}}{\partial \lambda} \times \frac{\partial \vec{r}}{\partial \xi} \right\| dA,$$

where  $S'$  is the bounds of  $S$  expressed in terms of  $\lambda$  and  $\xi$  and  $dA$  is the differential of area in terms of  $\lambda$  and  $\xi$ , generally something like  $d\lambda d\xi$ . We can reduce this

expression. We know the value of  $\vec{r}(\lambda, \xi)$ , so we find

$$\frac{\partial \vec{r}}{\partial \lambda} = \frac{\partial}{\partial \lambda} \begin{bmatrix} \cos \xi \sin \lambda \\ \sin \xi \sin \lambda \\ \cos \lambda \end{bmatrix} = \begin{bmatrix} \cos \xi \cos \lambda \\ \sin \xi \cos \lambda \\ -\sin \lambda \end{bmatrix}$$

and

$$\frac{\partial \vec{r}}{\partial \xi} = \frac{\partial}{\partial \xi} \begin{bmatrix} \cos \xi \sin \lambda \\ \sin \xi \sin \lambda \\ \cos \lambda \end{bmatrix} = \begin{bmatrix} -\sin \xi \sin \lambda \\ \cos \xi \sin \lambda \\ 0 \end{bmatrix}.$$

We can therefore simplify the expression  $\left\| \frac{\partial \vec{r}}{\partial \lambda} \times \frac{\partial \vec{r}}{\partial \xi} \right\|$  to be

$$\left\| \frac{\partial \vec{r}}{\partial \lambda} \times \frac{\partial \vec{r}}{\partial \xi} \right\| = \left\| \begin{bmatrix} \cos \xi \cos \lambda \\ \sin \xi \cos \lambda \\ -\sin \lambda \end{bmatrix} \times \begin{bmatrix} -\sin \xi \sin \lambda \\ \cos \xi \sin \lambda \\ 0 \end{bmatrix} \right\| = \left\| \begin{bmatrix} \cos \xi \sin^2 \lambda \\ \sin \xi \sin^2 \lambda \\ \cos \lambda \sin \lambda \end{bmatrix} \right\|.$$

Evaluating this norm, we arrive at

$$\left\| \frac{\partial \vec{r}}{\partial \lambda} \times \frac{\partial \vec{r}}{\partial \xi} \right\| = \left\| \begin{bmatrix} \cos \xi \sin^2 \lambda \\ \sin \xi \sin^2 \lambda \\ \cos \lambda \sin \lambda \end{bmatrix} \right\| = \sqrt{\cos^2 \xi \sin^4 \lambda + \sin^2 \xi \sin^4 \lambda + \cos^2 \lambda \sin^2 \lambda}.$$

With the identity  $\cos^2 \xi + \sin^2 \xi = 1$ , this quickly simplifies and rearranges to

$$\left\| \frac{\partial \vec{r}}{\partial \lambda} \times \frac{\partial \vec{r}}{\partial \xi} \right\| = \sqrt{\sin^2 \lambda (\sin^2 \lambda + \cos^2 \lambda)} = \sqrt{\sin^2 \lambda} = \sin \lambda.$$

We can substitute this into our surface integral to find

$$\iint_{S'} \sin \lambda \, dA.$$

While we have determined the formula for the area of the region  $S$  on the surface of the unit sphere (using spherical coordinates), we still have a problem. As mentioned in Section 3.3, this area is tedious to find directly, due to the  $\sin \lambda$  term in the integral. This is exactly the issue that causes maps that plot latitude and longitude as  $x$  and  $y$  to be distorted, or the areas used in Section 3.3. A change of variables is used to simplify the area calculations in that section. We substitute

$$\lambda' = \lambda \quad \text{and} \quad \xi' = (\xi - \mu) \sin \lambda + \mu.$$

Or, conversely,

$$\lambda = \lambda' \quad \text{and} \quad \xi = \frac{\xi' - \mu}{\sin \lambda} + \mu.$$

The variable  $\mu$  can be any real value. Here, we will limit it to values within the range of values of  $\xi$  found in  $S$ . For example, in Section 3.3, the mean of the values of  $\xi$  in the relevant points is used. However, the exact nature of the value of  $\mu$  does not impact this proof.

For the general double integral of function  $f(x, y)$ , over variables  $x$  and  $y$ , within the bounds of region  $D$ , the change of variables formula is

$$\iint_D f(x, y) \, dA = \iint_R f(a(u, v), b(u, v)) \left| \frac{\partial(x, y)}{\partial(u, v)} \right| \, dA',$$

where  $u$  and  $v$  are the new variables such that  $x = a(u, v)$  and  $y = b(u, v)$ ,  $R$  is the

region of integration in terms of  $u$  and  $v$ , and  $dA'$  is the differential, now also in terms of  $u$  and  $v$ . Finally,  $\left| \frac{\partial(x,y)}{\partial(u,v)} \right|$  is the Jacobian, which we can find as

$$\left| \frac{\partial(x,y)}{\partial(u,v)} \right| = \begin{vmatrix} \frac{\partial x}{\partial u} & \frac{\partial x}{\partial v} \\ \frac{\partial y}{\partial u} & \frac{\partial y}{\partial v} \end{vmatrix}.$$

In our case, with  $x = \xi$ ,  $y = \lambda$ ,  $u = \xi'$ , and  $v = \lambda'$ . the Jacobian is

$$\left| \frac{\partial(\xi, \lambda)}{\partial(\xi', \lambda')} \right| = \begin{vmatrix} \frac{\partial \xi}{\partial \xi'} & \frac{\partial \xi}{\partial \lambda'} \\ \frac{\partial \lambda}{\partial \xi'} & \frac{\partial \lambda}{\partial \lambda'} \end{vmatrix}.$$

With the definitions above, we find

$$\left| \frac{\partial(\xi, \lambda)}{\partial(\xi', \lambda')} \right| = \begin{vmatrix} \frac{1}{\sin \lambda'} & \frac{-(\xi' - \mu) \cos \lambda'}{\sin^2 \lambda'} \\ 0 & 1 \end{vmatrix} = \frac{1}{\sin \lambda'}.$$

With these new definitions and the formula for change of variables, our formula for the area in  $\xi$  and  $\lambda$ ,

$$\iint_{S'} \sin \lambda \, dA,$$

becomes, in terms of  $\xi'$  and  $\lambda'$

$$\iint_{S''} \sin \lambda' \left| \frac{\partial(\xi, \lambda)}{\partial(\xi', \lambda')} \right| dA' = \iint_{S''} \frac{\sin \lambda'}{\sin \lambda'} dA' = \iint_{S''} dA'.$$

This simple formula is exactly the formula used for area on a plane with Cartesian coordinates. Therefore, to find the area of the region  $S$  on the surface of the unit sphere, we simply need to describe the bounds of  $S$  in terms of spherical coordinates

$\xi$  and  $\lambda$ , perform the substitution

$$\lambda' = \lambda \quad \text{and} \quad \xi' = (\xi - \mu) \sin \lambda + \mu,$$

and plot the bounds of  $S$  in  $\lambda'$  and  $\xi'$  as if they were  $x$  and  $y$  on a plane. The simple Cartesian area of this transformed shape is the area of  $S$  on the surface of the unit sphere.



# Appendix C

## Homogeneous Transformations

Most of the concepts contained in this appendix can also be found in *Introduction to Robotics: Analysis, Control, Applications* [24].

Homogeneous transformations are based on a  $4 \times 4$  matrix to represent translation and multi-axis rotation between frame  $n$  and frame  $n + 1$ . Specifically, the matrix  ${}^nT_{n+1}$  is applied to the position of point  $\vec{r} = [r_{x_{n+1}} \ r_{y_{n+1}} \ r_{z_{n+1}} \ s]^T$ , expressed relative to the  $n + 1$  reference frame,<sup>1</sup> to convert it to the  $n$  reference frame by  ${}^nT_{n+1}\vec{r}$ . This matrix is of the form

$${}^nT_{n+1} = \begin{bmatrix} {}^n\vec{x}_{n+1} & {}^n\vec{y}_{n+1} & {}^n\vec{z}_{n+1} & {}^n\vec{p}_{n+1} \\ 0 & 0 & 0 & 1 \end{bmatrix} = \begin{bmatrix} {}^nR_{n+1} & {}^n\vec{p}_{n+1} \\ \vec{0}^T & 1 \end{bmatrix} \quad (\text{C.1})$$

where  ${}^n\vec{x}_{n+1}$  represents the  $x$ -axis of the  $n + 1$  frame, expressed in the coordinates of frame  $n$ . The same is true for the values of  $y_i$  and  $z_i$ . The standard  $3 \times 3$  rotation

---

<sup>1</sup>The  $s$  value in this vector is either 1 or 0, and it indicates whether the vector being transformed describes a point in space or a direction. If the value is  $s = 1$ , it describes a point, and thus it is affected by translation during the ensuing multiplication. If  $s = 0$ , it describes a direction, and is not affected by translation.

matrix  ${}^nR_{n+1}$  also represents the rotation in three-space described by these three vectors. The vector  ${}^n\vec{p}_{n+1} = [p_1 \ p_2 \ p_3]^T$  is the location of the origin of frame  $n + 1$  in frame  $n$ . As an example, consider the transformation of the previously-described  $\vec{r}$ , with its coordinates given in frame  $n + 1$ :

$$\begin{aligned} {}^nT_{n+1}\vec{r} &= \begin{bmatrix} {}^n\vec{x}_{n+1} & {}^n\vec{y}_{n+1} & {}^n\vec{z}_{n+1} & {}^n\vec{p}_{n+1} \\ 0 & 0 & 0 & 1 \end{bmatrix} \begin{bmatrix} r_{x_{n+1}} \\ r_{y_{n+1}} \\ r_{z_{n+1}} \\ s \end{bmatrix} \\ &= r_{x_{n+1}} \begin{bmatrix} {}^n\vec{x}_{n+1} \\ 0 \end{bmatrix} + r_{y_{n+1}} \begin{bmatrix} {}^n\vec{y}_{n+1} \\ 0 \end{bmatrix} + r_{z_{n+1}} \begin{bmatrix} {}^n\vec{z}_{n+1} \\ 0 \end{bmatrix} + s \begin{bmatrix} {}^n\vec{p}_{n+1} \\ 1 \end{bmatrix}. \end{aligned}$$

As we can see, this vector is now described in the  $n$  frame as  $r_{x_{n+1}}$  distance along the  $n + 1$   $x$ -axis,  $r_{y_{n+1}}$  distance along the  $n + 1$   $y$ -axis, and  $r_{z_{n+1}}$  distance along the  $n + 1$   $z$ -axis, from the origin of frame  $n + 1$ .<sup>2</sup> If these placeholder variables were replaced with relevant values, we would have a simple 4-vector representing the point in the  $n$  frame. The transformation from any frame to itself,  ${}^nT_n$ , is necessarily the identity matrix. Transformations can be inverted and used to transform in the other direction, such that

$$({}^nT_{n+1})^{-1} = {}^{n+1}T_n = \begin{bmatrix} {}^nR_{n+1}^T & -({}^nR_{n+1}^T) {}^n\vec{p}_{n+1} \\ \vec{0}^T & 1 \end{bmatrix} = \begin{bmatrix} {}^n\vec{x}_{n+1}^T & -{}^n\vec{x}_{n+1} \cdot {}^n\vec{p}_{n+1} \\ {}^n\vec{y}_{n+1}^T & -{}^n\vec{y}_{n+1} \cdot {}^n\vec{p}_{n+1} \\ {}^n\vec{z}_{n+1}^T & -{}^n\vec{z}_{n+1} \cdot {}^n\vec{p}_{n+1} \\ \vec{0}^T & 1 \end{bmatrix},$$

---

<sup>2</sup>Assuming  $s = 1$ . As mentioned previously, if  $s = 0$ , this vector represents a direction, not a point. If so, this transformation would be the same except without adding the origin, thus keeping the direction the same as reference frames change.

where  $\cdot$  is the dot product operator.

While the derivation is not shown here, there is a reasonable formula to go from DH parameters to a transformation matrix:

$${}^nT_{n+1} = T(\theta_n, d_n, a_n, \alpha_n) = \begin{bmatrix} \cos \theta_n & -\sin \theta_n \cos \alpha_n & \sin \theta_n \sin \alpha_n & a_n \cos \theta_n \\ \sin \theta_n & \cos \theta_n \cos \alpha_n & -\cos \theta_n \sin \alpha_n & a_n \sin \theta_n \\ 0 & \sin \alpha_n & \cos \alpha_n & d_n \\ 0 & 0 & 0 & 1 \end{bmatrix}.$$

Rotation of a joint in the robot, using our  $\phi$  formulation where changes in robot kinematics are independent from changes in geometry, can be expressed by a simplified version of this matrix. A rotation of  $\phi_n$  in the joint  $n$  between components  $n - 1$  and  $n$  (and corresponding the  $z$ -axis of frame  $n$ ) can be represented by

$$J(\phi_n) = T(\phi_n, 0, 0, 0) = \begin{bmatrix} \cos \phi_n & -\sin \phi_n & 0 & 0 \\ \sin \phi_n & \cos \phi_n & 0 & 0 \\ 0 & 0 & 1 & 0 \\ 0 & 0 & 0 & 1 \end{bmatrix}.$$

Note that this transformation is identical to a rotation about the  $z$ -axis, which is what we would expect. The position of point  $\vec{r}$ , with its coordinates given in frame  $n$ , while  $\phi_n \neq 0$ , could then be converted to frame  $n - 1$  using

$${}^{n-1}T_n J(\phi_n) \vec{r}$$

Chaining the transformation matrices  ${}^{n-1}T_n$  and  $J(\phi_n)$  can also be thought of as an

extension of the transformation matrix  ${}^{n-1}T_n$  itself, so that

$${}^{n-1}T_n J(\phi_n)$$

represents both the geometric structure and kinematic position associated with that coordinate transform.

The use of these transforms means many points and directions will be represented as 4-vectors. While 3-vectors are more standard, the usage of 4-vectors generally does not cause difficulty, with a few small exceptions, such as the application of the cross product. In cases where the three-vector form of a 4-vector is desired, the conversion will be indicated by  $(\vec{v})_{1:3}$ , such that

$$\left( \begin{array}{c} x \\ y \\ z \\ s \end{array} \right)_{1:3} = \begin{array}{c} x \\ y \\ z \end{array} .$$

The opposite conversion is simply achieved by writing  $\begin{array}{c} \vec{v} \\ 1 \end{array}$ .

# Appendix D

## Briefs Bottom Edge Orientation

### Proof

This appendix is based on the Mark III HBA model generated by the methods in Sections 2.2 and 2.3. It focuses on the two points (denoted as  $\vec{f}_L$  and  $\vec{r}_L$ , for the fore- and rearmost of the pair, respectively) of the left bottom edge which have  $z_1$ -coordinates equal to those of the centers of the bottom edges. This appendix proves  ${}^1\vec{f}_L = \vec{b}_1(\beta_1(0))$  and  ${}^1\vec{r}_L = \vec{b}_1(\beta_1(\pi))$ ,

Based on Equations 2.6 and 2.8, we know

$${}^1\vec{b}_1(\beta_1(p)) = {}^1T_2 \begin{bmatrix} r_{1b} \cos(\beta_1(p)) \\ r_{1b} \sin(\beta_1(p)) \\ h_{1/2} \\ 1 \end{bmatrix}.$$

With

$${}^1T_2 = \begin{bmatrix} \cos \theta_1 & -\sin \theta_1 \cos \alpha_1 & \sin \theta_1 \sin \alpha_1 & a_1 \cos \theta_1 \\ \sin \theta_1 & -\cos \theta_1 \cos \alpha_1 & -\cos \theta_1 \sin \alpha_1 & a_1 \sin \theta_1 \\ 0 & \sin \alpha_1 & \cos \alpha_1 & d_1 \\ 0 & 0 & 0 & 1 \end{bmatrix}$$

determined by applying Equation 2.1, we can rewrite  $\vec{b}_1(\beta_1(p))$  as

$$\begin{bmatrix} (a_1 + r_{1b} \cos(\beta_1(p))) \cos \theta_1 + (h_{1/2} \sin \alpha_1 - r_{1b} \sin(\beta_1(p)) \cos \alpha_1) \sin \theta_1 \\ (a_1 + r_{1b} \cos(\beta_1(p))) \sin \theta_1 - (h_{1/2} \sin \alpha_1 + r_{1b} \sin(\beta_1(p)) \cos \alpha_1) \cos \theta_1 \\ r_{1b} \sin(\beta_1(p)) \sin \alpha_1 + h_{1/2} \cos \alpha_1 + d_1 \\ 1 \end{bmatrix}.$$

We can see that the only values where the  $z_1$ -coordinate of  $\vec{b}_1(\beta_1(p))$  is equal to the bottom edge center  $z_1$ -coordinate ( $h_{1/2} \cos \alpha_1 + d_1$ ) are when  $\sin(\beta_1(p)) = 0$ . The two conditions that fulfill this are  $\beta_1(p) = 0$  and  $\beta_1(p) = \pi$ .

If  $\cos \theta_1 < 0$ , so  $\beta_1(0) = \pi$  and  $\beta_1(\pi) = 0$ , we have the  $x_1$ -coordinate of  $\vec{b}_1(\beta_1(0))$  as

$$-r_{1b} \cos \theta_1 + h_{1/2} \sin \theta_1 \sin \alpha_1 + a_1 \cos \theta_1$$

and of  $\vec{b}_1(\beta_1(\pi))$  as

$$r_{1b} \cos \theta_1 + h_{1/2} \sin \theta_1 \sin \alpha_1 + a_1 \cos \theta_1.$$

Knowing  $\cos \theta_1 < 0$ , we see that the foremost of the two points is  $\vec{f}_L = \vec{b}_1(\beta_1(0))$  and the rearmost is  $\vec{r}_L = \vec{b}_1(\beta_1(\pi))$ .

On the other hand, if  $\cos \theta_1 \geq 0$ , so  $\beta_1(0) = 0$  and  $\beta_1(\pi) = \pi$ , we have the  $x_1$ -

coordinate of  $\vec{b}_1(\beta_1(0))$  as

$$r_{1b} \cos \theta_1 + h_{1/2} \sin \theta_1 \sin \alpha_1 + a_1 \cos \theta_1$$

and of  $\vec{b}_1(\beta_1(\pi))$  as

$$-r_{1b} \cos \theta_1 + h_{1/2} \sin \theta_1 \sin \alpha_1 + a_1 \cos \theta_1.$$

Keeping in mind  $\cos \theta_1 \geq 0$ , we see once again that the foremost of the two points is

$\vec{f}_L = \vec{b}_1(\beta_1(0))$  and the rearmost is  $\vec{r}_L = \vec{b}_1(\beta_1(\pi))$ .





# Appendix E

## Constraint Simplification

We know the formulae for the constraints from Section 4.1. Using other formulae we have defined and various identities, we can rewrite and simplify the constraints. We also know that  $\theta_2 = \pi$  and  $\theta_3 = 0$ . Using these, we can rewrite our constraints.

### E.1 Briefs Constraints

- **Leg Direction:** We start with the constraint in Section 4.1.1:

$$\left( {}^1T_2 \begin{bmatrix} 0 \\ 0 \\ -1 \\ 0 \end{bmatrix} \right) \cdot \begin{bmatrix} 1 \\ 0 \\ 0 \\ 0 \end{bmatrix} \geq 0, \quad \left( {}^1T_2 \begin{bmatrix} 0 \\ 0 \\ -1 \\ 0 \end{bmatrix} \right) \cdot \begin{bmatrix} 0 \\ 1 \\ 0 \\ 0 \end{bmatrix} \geq 0, \quad \left( {}^1T_2 \begin{bmatrix} 0 \\ 0 \\ -1 \\ 0 \end{bmatrix} \right) \cdot \begin{bmatrix} 0 \\ 0 \\ 1 \\ 0 \end{bmatrix} \leq 0,$$

where  $\cdot$  is the dot product. We can see that

$$\left( {}^1T_2 \begin{bmatrix} 0 \\ 0 \\ -1 \\ 0 \end{bmatrix} \right) = \begin{bmatrix} -\sin \theta_1 \sin \alpha_1 \\ \cos \theta_1 \sin \alpha_1 \\ -\cos \alpha_1 \\ 0 \end{bmatrix}$$

Thus, we have  $\cos \alpha_1 \geq 0$ ,  $\cos \theta_1 \sin \alpha_1 \geq 0$ , and  $\sin \theta_1 \sin \alpha_1 \leq 0$ . Knowing cosine and sine and treating  $\theta_1 = \theta_1 \pmod{2\pi}$  and  $\alpha_1 = \alpha_1 \pmod{2\pi}$ , we see that these can be rewritten as:

$$\frac{\pi}{2} \geq \alpha_1 \vee \alpha_1 \geq \frac{3\pi}{2},$$

$$\left( \left( \frac{3\pi}{2} \leq \theta_1 \vee \frac{\pi}{2} \geq \theta_1 \right) \wedge 0 \leq \alpha_1 \leq \pi \right) \vee \left( \left( \frac{\pi}{2} \leq \theta_1 \leq \frac{3\pi}{2} \right) \wedge (\pi \leq \alpha_1 \leq 2\pi) \right),$$

and

$$(0 \leq \theta_1 \leq \pi \wedge \pi \leq \alpha_1 \leq 2\pi) \vee (\pi \leq \theta_1 \leq 2\pi \wedge 0 \leq \alpha_1 \leq \pi).$$

Asserting that all conditions are simultaneously true reduces the conditions to

$$\left( \left( \frac{3\pi}{2} \leq \theta_1 \leq 2\pi \right) \wedge \left( 0 \leq \alpha_1 \leq \frac{\pi}{2} \right) \right) \vee \left( \left( \frac{\pi}{2} \leq \theta_1 \leq \pi \right) \wedge \left( \frac{3\pi}{2} \leq \alpha_1 \leq 2\pi \right) \right)$$

- **Briefs Height:** We start with the constraint in Section 4.1.1:

$$\forall p \in [0, 2\pi), -z_{1,\max} \leq \left( {}^1\vec{b}_1(p) \cdot \begin{bmatrix} 0 \\ 0 \\ 1 \\ 0 \end{bmatrix} \right) \leq -z_{1,\min}.$$

We can show this by showing the points on  ${}^1\vec{b}_1(p)$  with the minimum and maximum  $z$  values satisfy the bounds. Using Equation 2.6, we find

$${}^1\vec{b}_1(p) \cdot \begin{bmatrix} 0 \\ 0 \\ 1 \\ 0 \end{bmatrix} = \left( {}^1T_2 \begin{bmatrix} r_{1b} \cos p \\ r_{1b} \sin p \\ h_{1/2} \\ 1 \end{bmatrix} \right) \cdot \begin{bmatrix} 0 \\ 0 \\ 1 \\ 0 \end{bmatrix}$$

With Equation 2.1, this can be rewritten as

$$\left( \begin{bmatrix} \cos \theta_1 & -\sin \theta_1 \cos \alpha_1 & \sin \theta_1 \sin \alpha_1 & a_1 \cos \theta_1 \\ \sin \theta_1 & \cos \theta_1 \cos \alpha_1 & -\cos \theta_1 \sin \alpha_1 & a_1 \sin \theta_1 \\ 0 & \sin \alpha_1 & \cos \alpha_1 & d_1 \\ 0 & 0 & 0 & 1 \end{bmatrix} \begin{bmatrix} r_{1b} \cos p \\ r_{1b} \sin p \\ h_{1/2} \\ 1 \end{bmatrix} \right) \cdot \begin{bmatrix} 0 \\ 0 \\ 1 \\ 0 \end{bmatrix}$$

and simplified to

$$r_{1b} \sin p \sin \alpha_1 + h_{1/2} \cos \alpha_1 + d_1.$$

These are the  $z_1$  values of the points on  $\vec{b}_1(p)$ . We need to identify the minimum and maximum (with respect to  $p$ ). By inspection, we can see that the minimum and maximum occur when the first term equals  $-r_{1b} \sin \alpha_1$  and  $r_{1b} \sin \alpha_1$ , respectively. Thus, we have the two constraints of

$$r_{1b} \sin \alpha_1 + h_{1/2} \cos \alpha_1 + d_1 \leq -z_{1,\min}$$

and

$$-r_{1b} \sin \alpha_1 + h_{1/2} \cos \alpha_1 + d_1 \geq -z_{1,\max}.$$

- **Leg Gap:** We start with the constraint in Section 4.1.1:

$$\forall p \in [0, 2\pi), \left( {}^1\vec{b}_1(p) \cdot \begin{bmatrix} 0 \\ 1 \\ 0 \\ 0 \end{bmatrix} \right) \geq \frac{y_{1,\min}}{2}.$$

This inequality is satisfied for all points if it is satisfied by the point on  $\vec{b}_1(p)$  with the minimum  $y$  value. From Equation 2.6, we find

$$\vec{b}_1(p) \cdot \begin{bmatrix} 0 \\ 1 \\ 0 \\ 0 \end{bmatrix} = \left( {}^1T_2 \begin{bmatrix} r_{1b} \cos p \\ r_{1b} \sin p \\ h_{1/2} \\ 1 \end{bmatrix} \right) \cdot \begin{bmatrix} 0 \\ 1 \\ 0 \\ 0 \end{bmatrix}$$

With Equation 2.1, this can be rewritten as

$$\left( \begin{bmatrix} \cos \theta_1 & -\sin \theta_1 \cos \alpha_1 & \sin \theta_1 \sin \alpha_1 & a_1 \cos \theta_1 \\ \sin \theta_1 & \cos \theta_1 \cos \alpha_1 & -\cos \theta_1 \sin \alpha_1 & a_1 \sin \theta_1 \\ 0 & \sin \alpha_1 & \cos \alpha_1 & d_1 \\ 0 & 0 & 0 & 1 \end{bmatrix} \begin{bmatrix} r_{1b} \cos p \\ r_{1b} \sin p \\ h_{1/2} \\ 1 \end{bmatrix} \right) \cdot \begin{bmatrix} 0 \\ 1 \\ 0 \\ 0 \end{bmatrix}$$

and simplifies to

$$r_{1b} (\sin \theta_1 \cos p + \cos \theta_1 \cos \alpha_1 \sin p) - h_{1/2} \cos \theta_1 \sin \alpha_1 + a_1 \sin \theta_1. \quad (\text{E.1})$$

These are the  $y_1$  values of the points on  $\vec{b}_1(p)$ . We need to identify the minimum (with respect to  $p$ ). We use the critical point test. We set the derivative of the

function, with respect to  $p$ , to 0:

$$r_{1b} (\cos \theta_1 \cos \alpha_1 \cos p - \sin \theta_1 \sin p) = 0.$$

Thus, we find, at the critical points,

$$\tan p = \cot \theta_1 \cos \alpha_1. \quad (\text{E.2})$$

Plugging Equation E.2 into Equation E.1, we find the  $y_1$  values at the critical points to be

$$\frac{r_{1b}}{\sqrt{1 + \tan^2 p}} (\pm_1 \sin \theta_1 \pm_2 \cos \theta_1 \cos \alpha_1 \tan p) - h_{1/2} \cos \theta_1 \sin \alpha_1 + a_1 \sin \theta_1$$

which simplifies to

$$\frac{r_{1b} \sin \theta_1}{\sqrt{1 + (\cot \theta_1 \cos \alpha_1)^2}} (\pm_1 1 \pm_2 (\cot \theta_1 \cos \alpha_1)^2) - h_{1/2} \cos \theta_1 \sin \alpha_1 + a_1 \sin \theta_1.$$

Knowing that  $r_{1b}$  and both terms inside the parentheses are positive, we can see that the the minimum value occurs when both of the  $\pm$ 's are negative. Thus, we have our minimum value as

$$-\frac{r_{1b} \sin \theta_1}{\sqrt{1 + (\cot \theta_1 \cos \alpha_1)^2}} (1 + (\cot \theta_1 \cos \alpha_1)^2) - h_{1/2} \cos \theta_1 \sin \alpha_1 + a_1 \sin \theta_1,$$

which simplifies to

$$a_1 \sin \theta_1 - r_{1b} \sin \theta_1 \sqrt{1 + (\cot \theta_1 \cos \alpha_1)^2} - h_{1/2} \cos \theta_1 \sin \alpha_1.$$

Our constraint is thus

$$a_1 \sin \theta_1 - r_{1b} \sin \theta_1 \sqrt{1 + (\cot \theta_1 \cos \alpha_1)^2} - h_{1/2} \cos \theta_1 \sin \alpha_1 \geq \frac{y_{1,\min}}{2}.$$

- **Leg Holes inside Briefs:** We start with the constraint in Section 4.1.1:

$$\forall p \in [0, 2\pi), \left\| \left( \vec{b}_1(p) \right)_{1:3} \times \begin{bmatrix} 0 \\ 0 \\ 1 \end{bmatrix} \right\| \leq r_{1t},$$

where  $\|*\|$  is the Euclidean Norm.

We know  $r_{1t}$  and the result of  $\|*\|$  are always positive, so we can rewrite this as

$$\forall p \in [0, 2\pi), \left\| \left( \vec{b}_1(p) \right)_{1:3} \times \begin{bmatrix} 0 \\ 0 \\ 1 \end{bmatrix} \right\|^2 \leq r_{1t}^2. \quad (\text{E.3})$$

Using Equations 2.1 and 2.6, we find  $\left( \vec{b}_1(p) \right)_{1:3}$  is equal to

$$\left( \begin{bmatrix} \cos \theta_1 & -\sin \theta_1 \cos \alpha_1 & \sin \theta_1 \sin \alpha_1 & a_1 \cos \theta_1 \\ \sin \theta_1 & \cos \theta_1 \cos \alpha_1 & -\cos \theta_1 \sin \alpha_1 & a_1 \sin \theta_1 \\ 0 & \sin \alpha_1 & \cos \alpha_1 & d_1 \\ 0 & 0 & 0 & 1 \end{bmatrix} \begin{bmatrix} r_{1b} \cos p \\ r_{1b} \sin p \\ h_{1/2} \\ 1 \end{bmatrix} \right)_{1:3}$$

and simplifies to

$$\begin{bmatrix} r_{1b}(\cos \theta_1 \cos p - \sin \theta_1 \cos \alpha_1 \sin p) + h_{1/2} \sin \theta_1 \sin \alpha_1 + a_1 \cos \theta_1 \\ r_{1b}(\cos p \sin \theta_1 + \sin p \cos \theta_1 \cos \alpha_1) - h_{1/2} \cos \theta_1 \sin \alpha_1 + a_1 \sin \theta_1 \\ r_{1b} \sin p \sin \alpha_1 + h_{1/2} \cos \alpha_1 + d_1 \end{bmatrix}.$$

The main expression of Equation E.3 can thus be rewritten as

$$\left\| \begin{bmatrix} r_{1b}(\cos \theta_1 \cos p - \sin \theta_1 \cos \alpha_1 \sin p) + h_{1/2} \sin \theta_1 \sin \alpha_1 + a_1 \cos \theta_1 \\ r_{1b}(\cos p \sin \theta_1 + \sin p \cos \theta_1 \cos \alpha_1) - h_{1/2} \cos \theta_1 \sin \alpha_1 + a_1 \sin \theta_1 \\ r_{1b} \sin p \sin \alpha_1 + h_{1/2} \cos \alpha_1 + d_1 \end{bmatrix} \times \begin{bmatrix} 0 \\ 0 \\ 1 \end{bmatrix} \right\|^2$$

and simplified to

$$\left\| \begin{bmatrix} r_{1b}(\cos p \sin \theta_1 + \sin p \cos \theta_1 \cos \alpha_1) - h_{1/2} \cos \theta_1 \sin \alpha_1 + a_1 \sin \theta_1 \\ -r_{1b}(\cos \theta_1 \cos p - \sin \theta_1 \cos \alpha_1 \sin p) - h_{1/2} \sin \theta_1 \sin \alpha_1 - a_1 \cos \theta_1 \\ 0 \end{bmatrix} \right\|^2.$$

Finding the norm, this equation becomes

$$(r_{1b}\gamma - h_{1/2} \cos \theta_1 \sin \alpha_1 + a_1 \sin \theta_1)^2 + (r_{1b}\kappa + h_{1/2} \sin \theta_1 \sin \alpha_1 + a_1 \cos \theta_1)^2$$

where

$$\gamma = \cos p \sin \theta_1 + \sin p \cos \theta_1 \cos \alpha_1 \text{ and } \kappa = \cos \theta_1 \cos p - \sin \theta_1 \cos \alpha_1 \sin p.$$

Expanding and simplifying, we arrive at

$$\begin{aligned}
& r_{1b}^2 (\gamma^2 + \kappa^2) + h_{1/2}^2 \sin^2 \alpha_1 + a_1^2 \\
& + 2r_{1b} ((\kappa \sin \theta_1 - \gamma \cos \theta_1) h_{1/2} \sin \alpha_1 + a_1 (\kappa \cos \theta_1 + \gamma \sin \theta_1))
\end{aligned} \tag{E.4}$$

We note

$$\kappa \sin \theta_1 - \gamma \cos \theta_1 = -\cos \alpha_1 \sin p$$

and

$$\kappa \cos \theta_1 + \gamma \sin \theta_1 = \cos p,$$

so Equation E.4 can be rewritten as

$$\begin{aligned}
& r_{1b}^2 (\gamma^2 + \kappa^2) + h_{1/2}^2 \sin^2 \alpha_1 + a_1^2 + 2r_{1b} (a_1 \cos p - h_{1/2} \cos \alpha_1 \sin p \sin \alpha_1) .
\end{aligned} \tag{E.5}$$

We also note

$$\gamma^2 + \kappa^2 = \cos^2 p + \sin^2 p \cos^2 \alpha_1,$$

so we Equation E.5 can be rearranged further to

$$\begin{aligned}
& r_{1b}^2 (\cos^2 p + \sin^2 p \cos^2 \alpha_1) + h_{1/2}^2 \sin^2 \alpha_1 \\
& + a_1^2 + 2r_{1b} (a_1 \cos p - h_{1/2} \cos \alpha_1 \sin p \sin \alpha_1) .
\end{aligned}$$

Grouping similar terms, this equation becomes

$$(a_1 + r_{1b} \cos p)^2 + (h_{1/2} \sin \alpha_1 - r_{1b} \cos \alpha_1 \sin p)^2$$



and the constraint can be rewritten as

$$\forall p \in [0, 2\pi), (a_1 + r_{1b} \cos p)^2 + (h_{1/2} \sin \alpha_1 - r_{1b} \cos \alpha_1 \sin p)^2 \leq r_{1t}^2. \quad (\text{E.6})$$

We can simplify this by considering the maximum value of the main expression and setting that to meet the constraint. We can find the maximum value using the critical point test. We set the derivative of Equation E.6, with respect to  $p$ , to 0:

$$0 = -2(a_1 + r_{1b} \cos p)r_{1b} \sin p - 2(h_{1/2} \sin \alpha_1 - r_{1b} \cos \alpha_1 \sin p)r_{1b} \cos \alpha_1 \cos p$$

Thus, we find

$$0 = (a_1 + r_{1b} \cos p) \sin p + (h_{1/2} \sin \alpha_1 - r_{1b} \sin p \cos \alpha_1) \cos \alpha_1 \cos p$$

or

$$0 = a_1 \sin p + r_{1b} \cos p \sin p \sin^2 \alpha_1 + h_{1/2} \sin \alpha_1 \cos \alpha_1 \cos p$$

There is no simple solution for this, so we cannot simply find a value and plug it back in. But we know that for a given geometry, we can solve the above, find the zeros, and plug them back into the previous expression. This limits the points that must be considered for Equation E.6.

Thus, our constraint simplifies to

$$(a_1 + r_{1b} \cos p)^2 + (h_{1/2} \sin \alpha_1 - r_{1b} \cos \alpha_1 \sin p)^2 \leq r_{1t}^2$$

for all  $p$  such that

$$0 = a_1 \sin p + r_{1b} \cos p \sin p \sin^2 \alpha_1 + h_{1/2} \sin \alpha_1 \cos \alpha_1 \cos p$$

## E.2 Proximal and Distal Sections Constraints

- **Frusta Length:** We start with the constraint equation from Section 4.1.2:

$$\forall n \in \{2, 3\}, \left\| \left\| \begin{bmatrix} 0 \\ 0 \\ h_{n-1/n} \\ 1 \end{bmatrix} - {}^n T_{n+1} \begin{bmatrix} 0 \\ 0 \\ h_{n/n+1} \\ 1 \end{bmatrix} \right\| \right\| \leq l_{\max}.$$

We can immediately simplify the math necessary, knowing both  $l_{\max}$  and the output of  $\|\cdot\|$  to be positive, by the constraint as

$$\forall n \in \{2, 3\}, \left\| \left\| \begin{bmatrix} 0 \\ 0 \\ h_{n-1/n} \\ 1 \end{bmatrix} - {}^n T_{n+1} \begin{bmatrix} 0 \\ 0 \\ h_{n/n+1} \\ 1 \end{bmatrix} \right\|^2 \right\| \leq l_{\max}^2.$$

Knowing  $\theta_2 = \pi$  and  $\theta_3 = 0$ , as specified in Section 4.2 and applying Equation 2.1, the main expression can be rewritten as

$$\left\| \begin{bmatrix} 0 \\ 0 \\ h_{n-1/n} \\ 1 \end{bmatrix} - \begin{bmatrix} \mp 1 & 0 & 0 & \mp a_n \\ 0 & \mp \cos \alpha_n & \pm \sin \alpha_n & 0 \\ 0 & \sin \alpha_n & \cos \alpha_n & d_n \\ 0 & 0 & 0 & 1 \end{bmatrix} \begin{bmatrix} 0 \\ 0 \\ h_{n/n+1} \\ 1 \end{bmatrix} \right\|^2$$

which simplifies to

$$\left\| \begin{bmatrix} 0 \\ 0 \\ h_{n-1/n} \\ 1 \end{bmatrix} - \begin{bmatrix} \mp a_n \\ \pm h_{n/n+1} \sin \alpha_n \\ d_n + h_{n/n+1} \cos \alpha_n \\ 1 \end{bmatrix} \right\|^2 = \left\| \begin{bmatrix} \pm a_n \\ \mp h_{n/n+1} \sin \alpha_n \\ h_{n-1/n} - d_n - h_{n/n+1} \cos \alpha_n \\ 0 \end{bmatrix} \right\|^2$$

and

$$a_n^2 + h_{n/n+1}^2 \sin^2 \alpha_n + (h_{n-1/n} - d_n - h_{n/n+1} \cos \alpha_n)^2.$$

This expression can be rearranged as

$$a_n^2 + h_{n/n+1}^2 + (d_n - h_{n-1/n})^2 + 2h_{n/n+1}(d_n - h_{n-1/n}) \cos \alpha_n$$

Therefore, we can rewrite our constraint as

$$\forall n \in \{2, 3\}, a_n^2 + h_{n/n+1}^2 + (d_n - h_{n-1/n})^2 + 2h_{n/n+1}(d_n - h_{n-1/n}) \cos \alpha_n \leq l_{\max}^2.$$

- **Frustra Angle:** We start with the constraint equation from Section 4.1.2:

$$\forall n \in \{2, 3\}, \begin{bmatrix} 0 \\ 0 \\ 1 \\ 0 \end{bmatrix} \cdot \left( {}^n T_{n+1} \begin{bmatrix} 0 \\ 0 \\ 1 \\ 0 \end{bmatrix} \right) \geq \cos \gamma_{\max}$$

Knowing  $\theta_2 = \pi$  and  $\theta_3 = 0$ , as specified in Section 4.2 and applying Equation 2.1, the main expression can be rewritten as

$$\begin{bmatrix} 0 \\ 0 \\ 1 \\ 0 \end{bmatrix} \cdot \left( \begin{bmatrix} \mp 1 & 0 & 0 & \mp a_n \\ 0 & \mp \cos \alpha_n & \pm \sin \alpha_n & 0 \\ 0 & \sin \alpha_n & \cos \alpha_n & d_n \\ 0 & 0 & 0 & 1 \end{bmatrix} \begin{bmatrix} 0 \\ 0 \\ 1 \\ 0 \end{bmatrix} \right)$$

or

$$\begin{bmatrix} 0 \\ 0 \\ 1 \\ 0 \end{bmatrix} \cdot \begin{bmatrix} 0 \\ \pm \sin \alpha_n \\ \cos \alpha_n \\ 0 \end{bmatrix} = \cos \alpha_n$$

Therefore, we can rewrite our constraint as

$$\forall n \in \{2, 3\}, \cos \alpha_n \geq \cos \gamma_{\max}.$$

Assuming these  $\alpha_n$  are in the range  $[-\pi, \pi]$ , we can rewrite this even more simply as

$$\forall n \in \{2, 3\}, |\alpha_n| \leq \gamma_{\max},$$

where  $|\cdot|$  is the absolute value symbol. Assuming  $\gamma_{\max}$  is in the first quadrant, this can also be written as

$$\forall n \in \{2, 3\}, -\gamma_{\max} \leq \alpha_n \leq \gamma_{\max}$$

- **Frusta Skew:** We start with the constraint equation from Section 4.1.2:

$$\forall n \in \{2, 3\}, \left\| \begin{bmatrix} 0 \\ 0 \\ 1 \end{bmatrix} \times \left( {}^n T_{n+1} \begin{bmatrix} 0 \\ 0 \\ h_{n/n+1} \\ 1 \end{bmatrix} \right)_{1:3} \right\| \leq r_{nt}$$

and

$$\forall n \in \{2, 3\}, \left\| \begin{bmatrix} 0 \\ 0 \\ 1 \end{bmatrix} \times \left( {}^{n+1} T_n \begin{bmatrix} 0 \\ 0 \\ h_{n-1/n} \\ 1 \end{bmatrix} \right)_{1:3} \right\| \leq r_{nb}.$$

To simplify the mathematics, knowing that all radii and the outputs of  $\|\cdot\|$  are positive, we rewrite this as

$$\forall n \in \{2, 3\}, \left\| \begin{bmatrix} 0 \\ 0 \\ 1 \end{bmatrix} \times \left( {}^n T_{n+1} \begin{bmatrix} 0 \\ 0 \\ h_{n/n+1} \\ 1 \end{bmatrix} \right)_{1:3} \right\|^2 \leq r_{nt}^2$$

and

$$\forall n \in \{2, 3\}, \left\| \begin{bmatrix} 0 \\ 0 \\ 1 \end{bmatrix} \times \left( {}^{n+1}T_n \begin{bmatrix} 0 \\ 0 \\ h_{n-1/n} \\ 1 \end{bmatrix} \right) \right\|_{1:3}^2 \leq r_{nb}^2.$$

Knowing  $\theta_2 = \pi$  and  $\theta_3 = 0$ , as specified in Section 4.2 and applying Equation 2.1, the main expression can be rewritten as

$$\left\| \begin{bmatrix} 0 \\ 0 \\ 1 \end{bmatrix} \times \left( \begin{bmatrix} \mp 1 & 0 & 0 & \mp a_n \\ 0 & \mp \cos \alpha_n & \pm \sin \alpha_n & 0 \\ 0 & \sin \alpha_n & \cos \alpha_n & d_n \\ 0 & 0 & 0 & 1 \end{bmatrix} \begin{bmatrix} 0 \\ 0 \\ h_{n/n+1} \\ 1 \end{bmatrix} \right) \right\|_{1:3}^2$$

and

$$\left\| \begin{bmatrix} 0 \\ 0 \\ 1 \end{bmatrix} \times \left( \begin{bmatrix} \mp 1 & 0 & 0 & -a_n \\ 0 & \mp \cos \alpha_n & \sin \alpha_n & -d_n \sin \alpha_n \\ 0 & \pm \sin \alpha_n & \cos \alpha_n & -d_n \cos \alpha_n \\ 0 & 0 & 0 & 1 \end{bmatrix} \begin{bmatrix} 0 \\ 0 \\ h_{n-1/n} \\ 1 \end{bmatrix} \right) \right\|_{1:3}^2.$$

We can simplify:

$$\left\| \begin{bmatrix} 0 \\ 0 \\ 1 \end{bmatrix} \times \left( \begin{bmatrix} \mp a_n \\ \pm h_{n/n+1} \sin \alpha_n \\ d_n + h_{n/n+1} \cos \alpha_n \\ 1 \end{bmatrix} \right) \right\|_{1:3}^2 = \left\| \begin{bmatrix} 0 \\ 0 \\ 1 \end{bmatrix} \times \begin{bmatrix} \mp a_n \\ \pm h_{n/n+1} \sin \alpha_n \\ d_n + h_{n/n+1} \cos \alpha_n \end{bmatrix} \right\|^2$$

to

$$\left\| \begin{bmatrix} \mp h_{n/n+1} \sin \alpha_n \\ \mp a_n \\ 0 \end{bmatrix} \right\|^2 = h_{n/n+1}^2 \sin^2 \alpha_n + a_n^2$$

and

$$\left\| \begin{bmatrix} 0 \\ 0 \\ 1 \end{bmatrix} \times \begin{pmatrix} -a_n \\ (h_{n-1/n} - d_n) \sin \alpha_n \\ (h_{n-1/n} - d_n) \cos \alpha_n \\ 1 \end{pmatrix} \right\|_{1:3}^2 = \left\| \begin{bmatrix} 0 \\ 0 \\ 1 \end{bmatrix} \times \begin{bmatrix} -a_n \\ (h_{n-1/n} - d_n) \sin \alpha_n \\ (h_{n-1/n} - d_n) \cos \alpha_n \end{bmatrix} \right\|^2$$

to

$$\left\| \begin{bmatrix} -(h_{n-1/n} - d_n) \sin \alpha_n \\ -a_n \\ 0 \end{bmatrix} \right\|^2 = (h_{n-1/n} - d_n)^2 \sin^2 \alpha_n + a_n^2.$$

Thus, our constraints can be rewritten as

$$\forall n \in \{2, 3\}, h_{n/n+1}^2 \sin^2 \alpha_n + a_n^2 \leq r_{nt}^2$$

and

$$\forall n \in \{2, 3\}, (h_{n-1/n} - d_n)^2 \sin^2 \alpha_n + a_n^2 \leq r_{nb}^2.$$

- **Frusta Height:** We start with the constraint equation from Section 4.1.2:

$$\forall n \in \{2, 3\}, \forall p \in [0, 2\pi), \left( \begin{bmatrix} 0 \\ 0 \\ 1 \\ 0 \end{bmatrix} \cdot {}^n \vec{b}_n(p) \right) \leq h_{n-1/n}.$$

Knowing  $\theta_2 = \pi$  and  $\theta_3 = 0$ , as specified in Section 4.2 and applying Equations 2.1 and 2.6, the main expression can be rewritten as

$$\begin{bmatrix} 0 \\ 0 \\ 1 \\ 0 \end{bmatrix} \cdot \left( \begin{bmatrix} \mp 1 & 0 & 0 & \mp a_n \\ 0 & \mp \cos \alpha_n & \pm \sin \alpha_n & 0 \\ 0 & \sin \alpha_n & \cos \alpha_n & d_n \\ 0 & 0 & 0 & 1 \end{bmatrix} \begin{bmatrix} r_{nb} \cos p \\ r_{nb} \sin p \\ h_{n/n+1} \\ 1 \end{bmatrix} \right).$$

This simplifies to

$$\begin{bmatrix} 0 \\ 0 \\ 1 \\ 0 \end{bmatrix} \cdot \left( \begin{bmatrix} \mp(r_{nb} \cos p + a_n) \\ \pm(h_{n/n+1} \sin \alpha_n - r_{nb} \sin p \cos \alpha_n) \\ d_n + h_{n/n+1} \cos \alpha_n + r_{nb} \sin p \sin \alpha_n \\ 1 \end{bmatrix} \right)$$

and

$$d_n + h_{n/n+1} \cos \alpha_n + r_{nb} \sin p \sin \alpha_n.$$

Thus, our constraint can be rewritten as

$$\forall n \in \{2, 3\}, \forall p \in [0, 2\pi), d_n + h_{n/n+1} \cos \alpha_n + r_{nb} \sin p \sin \alpha_n \leq h_{n-1/n}.$$



We can enforce this by finding the maximum of the main expression (with respect to  $p$ ), and forcing it to satisfy the constraint. By inspection (and knowing  $r_{nb} > 0$ ), we can see that the maximum will occur when  $\sin p$  has a magnitude of 1 and the same sign as  $\sin \alpha_n$ . In other words, this expression is maximized when  $\sin p \sin \alpha_n = |\sin \alpha_n|$ . Therefore, we can summarize our constraint as

$$\forall n \in \{2, 3\}, d_n + h_{n/n+1} \cos \alpha_n + r_{nb} |\sin \alpha_n| \leq h_{n-1/n}.$$

- **Frustrated Edge Gaps:** We start with the constraint equation from Section 4.1.2:

$$\forall n \in \{2, 3\}, \forall p_t \in [0, 2\pi), \forall p_b \in [0, 2\pi), \left\| {}^n \vec{t}_n(p_t) - {}^n \vec{b}_n(p_b) \right\| \geq l_{\min}.$$

The variable  $l_{\min}$  is always positive, as is the output of  $\|\cdot\|$ . Therefore, we can simplify this constraint by rewriting it as

$$\forall n \in \{2, 3\}, \forall p_t \in [0, 2\pi), \forall p_b \in [0, 2\pi), \left\| \vec{t}_n(p_t) - \vec{b}_n(p_b) \right\|^2 \geq l_{\min}^2.$$

Applying Equations 2.4 and 2.6, this simplifies as

$$\left\| \begin{bmatrix} r_{nt} \cos p_t \\ r_{nt} \sin p_t \\ h_{n-1/n} \\ 1 \end{bmatrix} - {}^n T_{n+1} \begin{bmatrix} r_{nb} \cos p_b \\ r_{nb} \sin p_b \\ h_{n/n+1} \\ 1 \end{bmatrix} \right\|^2.$$

Given that  $\theta_2 = \pi$  and  $\theta_3 = 0$ , this simplifies as

$$\left\| \begin{bmatrix} r_{nt} \cos p_t \\ r_{nt} \sin p_t \\ h_{n-1/n} \\ 1 \end{bmatrix} - \begin{bmatrix} \mp 1 & 0 & 0 & \mp a_n \\ 0 & \mp \cos \alpha_n & \pm \sin \alpha_n & 0 \\ 0 & \sin \alpha_n & \cos \alpha_n & d_n \\ 0 & 0 & 0 & 1 \end{bmatrix} \begin{bmatrix} r_{nb} \cos p_b \\ r_{nb} \sin p_b \\ h_{n/n+1} \\ 1 \end{bmatrix} \right\|^2.$$

Simplifying we arrive at

$$\left\| \begin{bmatrix} r_{nt} \cos p_t \pm r_{nb} \cos p_b \pm a_n \\ r_{nt} \sin p_t \pm r_{nb} \sin p_b \cos \alpha_n \mp h_{n/n+1} \sin \alpha_n \\ h_{n-1/n} - r_{nb} \sin p_b \sin \alpha_n - h_{n/n+1} \cos \alpha_n - d_n \\ 0 \end{bmatrix} \right\|^2,$$

which can be calculated as

$$\begin{aligned} & (r_{nt} \cos p_t \pm r_{nb} \cos p_b \pm a_n)^2 \\ & + (r_{nt} \sin p_t \pm r_{nb} \sin p_b \cos \alpha_n \mp h_{n/n+1} \sin \alpha_n)^2 \\ & + ((h_{n-1/n} - d_n) - r_{nb} \sin p_b \sin \alpha_n - h_{n/n+1} \cos \alpha_n)^2. \end{aligned}$$

While this constraint can be written in terms of the parameters, as is done here, it could not be simplified. It effectively requires finding the minimum distance between two arbitrary circles in  $\mathbb{R}^3$ , which does not have a simple solution [9].

Thus, this constraint is re-written as

$$\begin{aligned} & \forall n \in \{2, 3\}, \forall p_t \in [0, 2\pi), \forall p_b \in [0, 2\pi), \\ & (r_{nt} \cos p_t \pm r_{nb} \cos p_b \pm a_n)^2 + (r_{nt} \sin p_t \pm r_{nb} \sin p_b \cos \alpha_n \mp h_{n/n+1} \sin \alpha_n)^2 \\ & + ((h_{n-1/n} - d_n) - r_{nb} \sin p_b \sin \alpha_n - h_{n/n+1} \cos \alpha_n)^2 \geq l_{\min}^2, \end{aligned}$$

where the sign of  $\pm$  depends on  $\theta_n$ . If  $\theta_n = 0$ , then it is positive, and if  $\theta_n = \pi$ , it is negative.



# Bibliography

- [1] Isaac Abramov, N. Moiseyev, and A. Stoklitsky. Concept of Space Suit Enclosure for Planetary Exploration. In *31st International Conference On Environmental Systems*, Jul 2001. doi:10.4271/2001-01-2168.
- [2] Daniel M. Barry and John W. Bassick. NASA Space Shuttle Advanced Crew Escape Suit Development. *SAE Transactions*, 104:696–701, 1995.
- [3] Steven P. Chappell, Jason R. Norcross, Andrew F. J. Abercromby, Omar S. Bekdash, Elizabeth A. Benson, Sarah L. Jarvis, Johnny Conkin, Michael L. Gernhardt, Nancy House, Jennifer Jadwick, Jeffrey A. Jones, Lesley R. Lee, Richard A. Scheuring, and Jennifer A. Tuxhorn. *Evidence Report: Risk of Injury and Compromised Performance due to EVA Operations*. National Aeronautics and Space Administration, Jan 2017. Available on NASA Technical Reports Server at <https://ntrs.nasa.gov/archive/nasa/casi.ntrs.nasa.gov/20170002574.pdf>.
- [4] Cinda Chullen, Joe McMann, Ken Thomas, Joe Kosmo, Cathleen Lewis, Rebecca Wright, Rose Bitterly, and Vladenka Oliva. U.S. Spacesuit Legacy: Maintaining it for the Future. In *43rd International Conference on Environmental Systems*. American Institute of Aeronautics and Astronautics, Jul 2013. doi:10.2514/6.2013-3498.
- [5] Matthew S. Cowley, Sarah Margerum, Lauren Hharvill, and Sudhakar Rajulu. Model for Predicting the Performance of Planetary Suit Hip Bearing Designs. In *4th International Conference on Applied Human Factors and Ergonomics*. National Aeronautics and Space Administration, Jul 2012. Available on NASA Technical Reports Server.
- [6] Conor R. Cullinane, Richard A. Rhodes, and Leia A. Stirling. Mobility and Agility During Locomotion in the Mark III Space Suit. *Aerospace Medicine and Human Performance*, 88(6):589–596, Jun 2017. doi:10.3357/AMHP.4650.2017.

- [7] Conor Ryan Cullinane. *Evaluation of the Mark III Spacesuit: An Experimental and Computational Modeling Approach*. PhD thesis, Massachusetts Institute of Technology, 2018.
- [8] Conor Ryan Cullinane. Evaluation of the Mark III Spacesuit: An Experimental and Computational Modeling Approach, June 2018. PhD Thesis Defense Slides.
- [9] David Eberly. Distance to Circles in 3D. Technical report, Geometric Tools, Geometric Tools, Redmond, Washington, Feb 2019. Available at <https://www.geometrictools.com/Documentation/DistanceToCircle3.pdf>.
- [10] Charles W. Flugel, Joseph J. Kosmo, and John R. Rayfield. Development of a Zero-Prebreathe Spacesuit. In *14th Intersociety Conference on Environmental Systems*, pages 840–981, Jul 1984. doi:10.4271/840981.
- [11] Claire C. Gordon, Cynthia L. Blackwell, Bruce Bradtmiller, Joseph L. Parham, Patricia Barrientos, Stephen P. Paquette, Brian D. Corner, Jeremy M. Carson, Joseph C. Venezia, Belva M. Rockwell, et al. 2012 Anthropometric Survey of US Army Personnel: Methods and Summary Statistics. Technical report, ARMY NATICK SOLDIER RESEARCH DEVELOPMENT AND ENGINEERING CENTER MA, 2014.
- [12] David Graziosi and Janet G. Ferl. Performance Evaluations of an Advanced Space Suit Design for International Space Station and Planetary Applications. In *29th International Conference on Environmental Systems*, Jul 1999. doi:10.4271/1999-01-1967.
- [13] Stephen J. Hoffman. Advanced EVA Capabilities: A Study for NASA’s Revolutionary Aerospace Systems Concept Program. Technical Report 20040200983, NASA Johnson Space Center, NASA Johnson Space Center, Houston, Texas, April 2004. Available on NASA Technical Reports Server.
- [14] Christopher David King. A Coupled Contact-Mechanics Computational Model for Studying Deformable Human-Artifact Contact. Master’s thesis, Massachusetts Institute of Technology, Department of Mechanical Engineering, June 2018.
- [15] Joseph J. Kosmo and Amy Ross. Space Suit Mobility Evaluations in Lunar/Mars Gravity Environments. In *28th International Conference on Environmental Systems*, Jul 1998. doi:10.4271/981627.

- [16] Joseph J. Kosmo, William E. Spenny, Rob Gray, and Phil Spampinato. Development of the NASA ZPS Mark III 57.2-kN/m<sup>2</sup> (8.3 psi) Space Suit. In *18th Intersociety Conference on Environmental Systems*, pages 630–650. SAE International, July 1988.
- [17] Andreas Kranzl. Normative Gait Database. Available on Clinical Gait Analysis Website <http://www.clinicalgaitanalysis.com/data/kinematics>.
- [18] Mathworks. evalclusters, Jul 2019. <https://www.mathworks.com/help/stats/evalclusters.html>.
- [19] Bill McDonald. surf2stl, Feb 2004. MATLAB Central File Exchange <https://www.mathworks.com/matlabcentral/fileexchange/4512-surf2stl> The available code was modified in some use cases for speed and efficiency. Some portions of this research required using this function hundreds of thousands of times. To make that process more efficient, unused generalizations and input checking were removed from the code. To further reduce computation time, the code was modified in some uses to output the data as a pair of arrays containing .STL-formatted data, rather than saving every geometry as a file.
- [20] NASA, Jul 1969. NASA Photo AS11-40-5903, available at [https://spaceflight.nasa.gov/gallery/images/apollo/apollo11/html/as11\\_40\\_5902.html](https://spaceflight.nasa.gov/gallery/images/apollo/apollo11/html/as11_40_5902.html).
- [21] NASA, Jul 1969. NASA Photo AS11-40-5902, available at [https://spaceflight.nasa.gov/gallery/images/apollo/apollo11/html/as11\\_40\\_5903.html](https://spaceflight.nasa.gov/gallery/images/apollo/apollo11/html/as11_40_5903.html).
- [22] NASA, Oct 2004. NASA Photo JSC2004-E-43624, available at <https://spaceflight.nasa.gov/gallery/images/exploration/esas/html/jsc2004e43624.html>.
- [23] Dava Newman, P. B. Schmidt, D. B. Rahn, Norman Badler, and Dimitris Metaxas. Modeling the Extravehicular Mobility Unit (EMU) Space Suit: Physiological Implications for Extravehicular Activity (EVA). In *30th International Conference on Environmental Systems*, 07 2000. doi:10.4271/2000-01-2257.
- [24] Saeed B. Niku. *Introduction to Robotics: Analysis, Control, Applications*. Wiley, Hoboken, New Jersey, second edition, 2011.

- [25] Jason R. Norcross, Kurt G. Clow, Leah C. Stroud, Lena Desantis, Jessica R. Vos, and Michael L. Gernhardt. Metabolic Costs and Biomechanics of Inclined Ambulation and Exploration Tasks in a Planetary Suit. Technical report, National Aeronautics and Space Administration, NASA Center for AeroSpace Information, Hanover, Maryland, June 2010. [https://ston.jsc.nasa.gov/collections/TRS/\\_techrep/TP-2010-216125.pdf](https://ston.jsc.nasa.gov/collections/TRS/_techrep/TP-2010-216125.pdf).
- [26] Asbjørn Roaas and Gunnar B. J. Andersson. Normal Range of Motion of the Hip, Knee and Ankle Joints in Male Subjects, 30–40 Years of Age. *Acta Orthopaedica Scandinavica*, 53(2):205–208, 1982. doi:10.3109/17453678208992202.
- [27] Amy Ross. Advanced Space Suits. In *Society for the Advancement of Material and Process Engineering*. National Aeronautics and Space Administration, May 2016. Available on NASA Technical Reports Server.
- [28] Richard A. Scheuring, Jeffrey A. Jones, Joseph D. Novak, James D. Polk, David B. Gillis, Josef Schmid, James M. Duncan, and Jeffrey R. Davis. The Apollo Medical Operations Project: Recommendations to improve crew health and performance for future exploration missions and lunar surface operations. *Acta Astronautica*, 63(7–10):980–987, Oct 2008. doi:10.1016/j.actaastro.2007.12.065.
- [29] Patricia B. Schmidt, Dava J. Newman, and Edward Hodgson. Modeling Space Suit Mobility: Applications to Design and Operations. In *31st International Conference on Environmental Systems*, Jul 2001. doi:10.4271/2001-01-2162.
- [30] Jeong Chang Seong, Karen A. Mulcahy, and E. Lynn Usery. The Sinusoidal Projection: A New Importance in Relation to Global Image Data. *The Professional Geographer*, 54(2):218–225, 2002. doi:10.1111/0033-0124.00327.
- [31] K. Alex Shorter, Amy Wu, and Arthur D. Kuo. The High Cost of Swing Leg Circumduction during Human Walking. *Gait & Posture*, 54:265–270, May 2017.
- [32] John Parr Snyder. *Map Projections—A Working Manual*, volume 1395. US Government Printing Office, 1987.
- [33] Leia Stirling, Pedro Arezes, and Allison Anderson. Implications of Space Suit Injury Risk for Developing Computational Performance Models. *Aerospace Medicine and Human Performance*, 90(6):553–565, Jun 2019. doi:10.3357/AMHP.5221.2019.



- [34] Márta Szilvsi-Nagy and Gyula Mátyási. Analysis of STL files. *Mathematical and Computer Modelling*, 38(7–9):945–960, Oct 2003. doi:10.1016/S0895-7177(03)90079-3.
- [35] Jaroslaw Tuszynski. Triangle/Ray Intersection, Mar 2019. MATLAB Central File Exchange, <https://www.mathworks.com/matlabcentral/fileexchange/33073-triangle-ray-intersection>. The available code was modified for speed and efficiency, removing the generality of the original code to make it faster for the specific usage.
- [36] Jessica R. Vos, Michael L. Gernhardt, and Lesley Lee. The Walkback Test: A Study to Evaluate Suit and Life Support System Performance Requirements for a 10 Kilometer Lunar Traverse in a Planetary Suit. In *37th International Conference on Environmental Systems*, Jul 2007. doi:10.4271/2007-01-3133.
- [37] Richard D. Watson. Use MACES IVA Suit for EVA Mobility Evaluations. In *44th International Conference On Environmental Systems*. National Aeronautics and Space Administration, Jan 2014. Available on NASA Technical Reports Server.
- [38] Leslie A. Wickman and Bernadette Luna. Locomotion while load-carrying in reduced gravities. *Aviation, space, and environmental medicine*, 67:940–6, Nov 1996.
- [39] Ge Wu, Sorin Siegler, Paul Allard, Chris Kirtley, Alberto Leardini, Dieter Rosenbaum, Mike Whittle, Darryl D. D’Lima, Luca Cristofolini, Hartmut Witte, et al. ISB Recommendation on Definitions of Joint Coordinate System of Various Joints for the Reporting of Human Joint Motion—Part I: Ankle, Hip, and Spine. *Journal of Biomechanics*, 35(4):543–548, Apr 2002. doi:10.1016/S0021-9290(01)00222-6.